AN ENGINEERED HYDROGEL PLATFORM FOR UNDERSTANDING BREAST CANCER DORMANCY, REACTIVATION, AND CHEMORESISTANCE FOR DRUG DEVELOPMENT

by

Cindy J. Farino Reyes

A dissertation submitted to the Faculty of the University of Delaware
in partial fulfillment of the requirements for the degree of
Doctor of Philosophy in Biomedical Engineering

Winter 2022

AN ENGINEERED HYDROGEL PLATFORM FOR UNDERSTANDING BREAST CANCER DORMANCY, REACTIVATION, AND CHEMORESISTANCE FOR DRUG DEVELOPMENT

by

Cindy J. Farino Reyes

Approved: _____
Kristi Kiick, Ph.D.
Chair of the Department of Biomedical Engineering

Approved: _____
Levi T. Thompson, Ph.D.
Dean of the College of Engineering

Approved: _____
Louis F. Rossi, Ph.D.
Vice Provost for Graduate and Professional Education and Dean of the Graduate College

I certify that I have read this dissertation and that in my opinion it meets the academic and professional standard required by the University as a dissertation for the degree of Doctor of Philosophy.

Signed: _____

John H. Slater, Ph.D.
Professor in charge of dissertation

I certify that I have read this dissertation and that in my opinion it meets the academic and professional standard required by the University as a dissertation for the degree of Doctor of Philosophy.

Signed: _____

Jennifer Sims-Mourtada, Ph.D.
Member of dissertation committee

I certify that I have read this dissertation and that in my opinion it meets the academic and professional standard required by the University as a dissertation for the degree of Doctor of Philosophy.

Signed: _____

Kelvin H. Lee, Ph.D.
Member of dissertation committee

I certify that I have read this dissertation and that in my opinion it meets the academic and professional standard required by the University as a dissertation for the degree of Doctor of Philosophy.

Signed: _____

Elise Corbin, Ph.D.
Member of dissertation committee

ACKNOWLEDGEMENTS

This work was supported by the National Institutes of Health (R21CA214299) and the W.M. Keck Foundation (15A00396). The Bio-Imaging Center in the Delaware Biotechnology Institute provided confocal microscopy with support from the NIHNIGMS (P20 GM103446), the NSF (IIA 1301765), and the State of Delaware. I extend my thanks to the University of Delaware Biomedical Engineering Department for their support through the 2018 University Graduate Scholar Award, 2019 University Graduate Scholar Award, 2021 University BME Graduate Student Best Paper Award, and the 2021 University Doctoral Fellowship, and to my dissertation committee members for their ongoing support.

I would also like to thank my advisor, Dr. John Slater for his valuable input and advice, and all past and present Slater Lab members including Ryan Taitano, Samuel Freeman, John Sperduto, Keely Keller, Ph.D., Omar Banda, Ph.D., Zeinab Fereshteh, Ph.D., and Shantanu Pradhan, Ph.D.. Special acknowledgements go to Dr. Shantanu Pradhan for laying the groundwork for the studies conducted in this dissertation. Alongside Slater Lab members, I would like to thank Megan Dang for her friendship and fond memories throughout my time at Delaware.

My family has played a significant role in the completion of this work. For your support and welcoming me into your family thank you to Florence Foo, David Kwok, and Alex Kwok. I want to also thank my tía Karen Farino who has inspired my interest in the medical field and has always supported our family, and tíos Carlota and Miguel Davila for their love and affection. My sister, Stefany Farino, has always

inspired me to work hard and live up to her great achievements. Now that we have grown into our own lives, I could not be more proud of you and your well-earned accomplishments. You stepped up as the leader of the family as a child and have always been an essential part of all our successes. I want to thank you for your support. I want to extend this thanks to my brother Anil Maharjan, who has never been hesitant to help the family. Finally, this work would not have been possible without my parents, Rosa Reyes and Alfonso Farino, who have sacrificed everything to build us a better life.

Lastly I must thank my husband, Bryan Kwok, who has been the ultimate support throughout my time at Delaware. Together, we have made it past many obstacles, and I cannot thank you enough for your unconditional love and support.

DEDICATION

To my parents, Rosa Reyes and Alfonso Farino, whose constant determination and perseverance inspire me to overcome any challenge.

TABLE OF CONTENTS

Appendix

LIST OF FIGURES

ABSTRACT

Metastasis remains the leading cause of cancer-associated death worldwide. A latency period ranging from months to decades is often observed prior to relapse as disseminated tumor cells (DTCs) can undergo dormancy upon infiltration of secondary organs. While eliminating these dormant cells can prevent recurrence, current chemotherapeutics fail to effectively target and eliminate dormant populations. Mechanistic understanding of dormancy-associated chemoresistance could lead to development of targeted therapeutic strategies. In the effort towards developing new therapeutic strategies to eliminate dormant cells, we developed an *in vitro*, hydrogel platform to mimic generic premetastatic niches during initial DTC infiltration of secondary tissues.

In particular, we investigated the role of hydrogel properties (matrix adhesivity and degradability) in regulating the phenotypic fate of breast cancer using five breast cancer cell lines: the triple negative MDA-MB-231 (231) parental line, three organotropic sublines derived from the parental 231 line: BoM-1833 (bone-tropic), LM2-4175 (lung-tropic), and BrM2a-831 (brain-tropic), and the estrogen receptor positive (ER^+) MCF7 cell line. Each cell line was individually encapsulated and cultured for 15 days in three distinct, poly(ethylene glycol) (PEG)-based hydrogel formulations composed of proteolytically degradable PEG (PEG-PQ), integrin-ligating RGDS, and the non-degradable crosslinker N-vinyl pyrrolidone (NVP). We varied concentrations of RGDS and NVP to mimic favorable and unfavorable premetastatic niches including a permissive niche with high levels of adhesivity and degradability

(Gel 1: ++ adhesivity, ++ degradability), a non-permissive niche with moderate levels of adhesivity and degradability (Gel 2: + adhesivity, + degradability), and a non-permissive niche with no adhesivity but high degradability (Gel 3: - adhesivity, ++ degradability). Dormancy-associated metrics including temporal changes in viable cell density, proliferation, metabolism, apoptosis, phosphorylated-ERK (p-ERK) and -p38 (p-p38), and morphological characteristics were quantified. A multimetric classification approach was implemented to categorize each hydrogel-induced phenotype as: (1) growth, (2) balanced tumor dormancy, (3) balanced cellular dormancy, or (4) restricted survival, cellular dormancy. Hydrogels with high adhesivity and degradability (permissive gel 1) promoted growth in all five cell lines tested. Hydrogels with no adhesivity, but high degradability (non-permissive gel 3), induced restricted survival, cellular dormancy in the parental 231 and MCF7 lines and balanced cellular dormancy in the organotropic lines demonstrating the role of cell adhesion in inducing dormancy while also highlighting the enhanced survival capabilities of organotropic sublines. Hydrogels with moderate adhesivity and degradability (non-permissive gel 2) induced balanced cellular dormancy in the parental 231 and lung-tropic lines and balanced tumor mass dormancy in bone- and brain-tropic lines and MCF7s, demonstrating that matrix confinement can induce dormancy. The ability to induce escape from dormancy, reactivation, via “on-demand” dynamic incorporation of RGDS into a highly degradable hydrogel was also demonstrated.

With an established dormancy and reactivation platform, we implemented this system to quantify dormancy-associated chemoresistance. The cellular responses to doxorubicin (DOX), paclitaxel (PAC), and 5-fluorouracil (5-FU) in the growth

formulation (permissive gel 1), and dormant formulations (non-permissive gels 2 and 3) in parental 231s were quantified via measurement of half maximal inhibitory concentration (IC_{50}) and half maximal effective concentration (EC_{50}) values. Under PAC and 5-FU treatment, parental 231s residing in either dormant state exhibited increased chemoresistance compared to 231s in the growth state in permissive gel 1. DOX was further tested on growing, dormant, and reactivated parental 231s, organotropic sublines, and MCF7s. Parental 231s undergoing dormancy demonstrated increased chemoresistance with a 1.4 to 1.8-fold increase in EC_{50} and 1.3 to 1.8-fold increase in IC_{50} compared to cells in the growth state. Furthermore, reactivated parental 231s were also chemoresistant and displayed a ~2.5 fold increase in the EC_{50}. Similar results were observed for organotropic sublines and MCF7s. To mechanistically investigate the role of dormancy in conferring DOX resistance, cytoplasmic and nuclear accumulation of DOX was measured. The results indicated statistically significantly higher DOX accumulation rates and nuclear localization, determined by nuclear to cytoplasmic mean intensity ratio (NC ratio), in cells in the growth state (permissive gel 1) compared to the two dormant (non-permissive gels 2 and 3) and reactivated states. These results further validated the utility of implementing engineered hydrogels as an *in vitro* platform to induce breast cancer dormancy for the development of anti-dormancy therapeutic strategies and provided valuable insight into the mechanisms involved in dormant and reactivated cell chemoresistance.

Based on our findings that chemoresistant dormant and reactivated cells exhibit decreased DOX intracellular accumulation rates and subsequent localization to the nucleus, we investigated the role of three ABC-efflux pumps (P-gp, MRP1, and

BCRP) which are known to be overexpressed in chemoresistant cancers. Immunofluorescence analysis revealed that chemoresistant dormant and reactivated cells expressed significantly greater levels of P-gp, MRP1, and BCRP (excluding MCF7s which had similar levels of BCRP expression in all states), compared to more chemosensitive cells residing in the growth state induced by permissive gel 1. To determine if differential efflux pump expression played a role in chemoresistance, efflux pumps were inhibited using a P-gp inhibitor (10 nM tariquidar), MRP1 inhibitor (50 μM MK571), BCRP inhibitor (10 μM Ko 143), or a combination of all three inhibitors on parental 231s, brain-tropic 231s, and MCF7s. Results showed that efflux pump inhibition significantly increased chemosensitivity, indicated by significant decreases in EC_{50} values, in all three cell lines. For instance, P-gp+MRP1+BCRP inhibition decreased EC_{50} values to 4.2 ± 1.1 μM (permissive gel 1, ~11-fold decrease), 0.4 ± 0.1 μM (non-permissive gel 2, ~170-fold decrease), 1.1 ± 0.5 μM (non-permissive gel 3, ~81-fold decrease), and 1.4 ± 0.3 μM (reactivated, ~81-fold decrease) compared to no inhibition, with significantly lower EC_{50} values in dormant and reactivated parental 231s than cells in permissive gel 1. Increased chemoresistance was accompanied by significant increases in the DOX accumulation rate (~3-11-fold increase) and NC ratio (~1.2-3.2-fold increase) for all three cell lines. Furthermore, efflux pump inhibition led to significantly greater accumulation rates and, in most cases, greater NC ratios in dormant and reactivated cells compared to growing cells in permissive gel 1. These results provide novel insights in the role of efflux pumps in dormancy and reactivated cell chemoresistance and proposes a therapeutic strategy to target and eliminate dormant and reactivated cells *in vivo*.

Taken together this work provides a well-characterized hydrogel platform to induce breast cancer dormancy and reactivation as demonstrated in five breast cancer lines, implements the platform to quantify dormant and reactivated cell chemoresistance, provides novel insight regarding DOX accumulation and localization in dormant and reactivated cells, provides insight into the role of efflux pumps in chemoresistance and DOX transport, and demonstrates the ability to increase DOX efficacy in treatment of highly chemoresistant dormant and reactivated cancer via efflux pump inhibition *in vitro*. Future implementation of these results could be used to model dormancy in other cancers and investigate mechanisms involved in dormancy and reactivation. Furthermore, we show that this platform can be used in drug development and plan future studies to test our treatment strategy *in vivo*, with the ultimate goal to eliminate dormant cells and aid in preventing metastatic relapse.

Chapter 1

INTRODUCTION

Sections in this chapter have been adapted from the following articles:

(1) Pradhan S, Sperduto JL, Farino CJ, Slater JH. Engineered In Vitro Models of Tumor Dormancy and Reactivation. Journal of Biological Engineering 2018, 12 (37).

(2) Farino CJ, Pradhan S, Slater JH. The Influence of Matrix-Induced Dormancy on Metastatic Breast Cancer Chemoresistance. ACS Applied Biomaterials 2020, 3(9), 5832-5844.

(3) Farino Reyes CJ, Pradhan S, Slater JH. The Influence of Ligand Density and Degradability on Hydrogel Induced Breast Cancer Dormancy and Reactivation. Advanced Healthcare Materials 2021, 10(11), 2002227.

1.1 Overview and Clinical Relevance

Significant strides in cancer detection and treatment have increased 5-year survival rates.[1] Unfortunately, metastasis remains responsible for >90% of cancer-associated deaths.[1,2] Metastasis occurs when disseminated tumor cells (DTCs) leave the primary tumor and invade secondary organs. However, the pathway between initial diagnosis and treatment and metastasis is not straightforward. Prior to relapse, there is often a latency period that can range from months to decades, during which there is no detectable cancer.[3,4] This latency period is determined by tumor dormancy where residual DTCs reside in a dormant state that delays the growth of clinically detectable

tumors.[3] Dormant cells may undergo cellular quiescence for decades,[4] before returning to an actively proliferative state that results in metastatic relapse. DTCs originating from the primary tumor may also extravasate into secondary organs where <2% of the cells survive.[5,6] Surviving DTCs undergo one of three possible fates: cellular dormancy,[3,7-9] tumor mass dormancy,[3,7,10-12] or growth (Figure 1.1).[13,14] In cellular dormancy, surviving cells employ anti-apoptotic survival mechanisms to remain in G_0-G_1 cell cycle arrest. Cells undergoing tumor mass dormancy maintain a delicate balance between proliferation and apoptosis which prevents tumors (or multi-cellular clusters) from growing to a clinically detectable size. Over time and with matrix remodeling, dormant DTCs can become reactivated and resume growth, leading to the formation of overt lesions and metastatic relapse (Figure 1.2).[3,4]

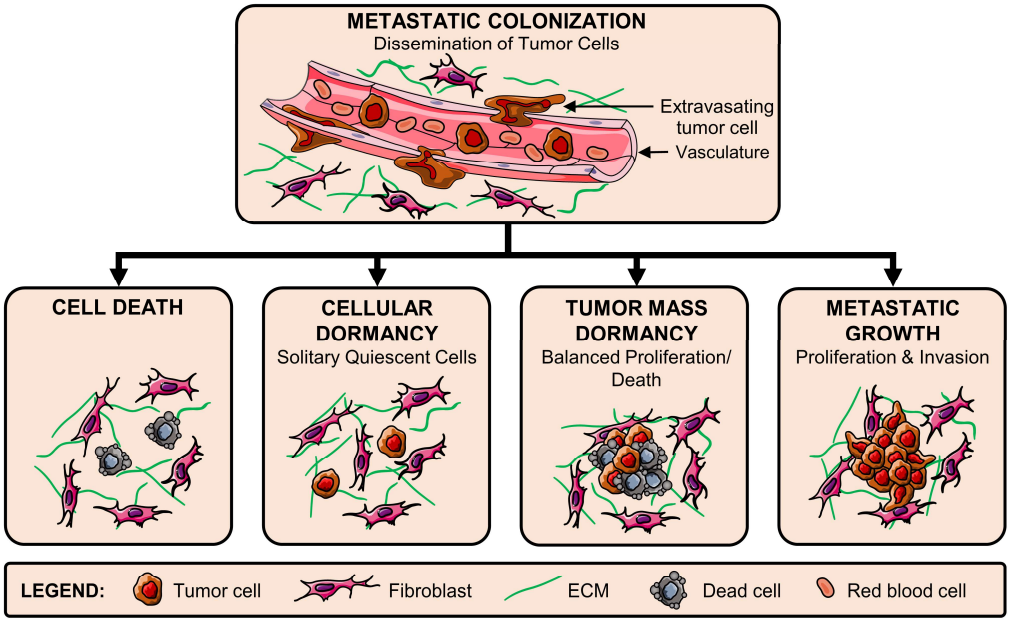

Figure 1.1: Fate of Disseminated Tumor Cells. Circulating tumor cells extravasate from vasculature at secondary sites and undergo one of four fates in the secondary niche: cell death (primarily via apoptosis), cellular dormancy (remain as single quiescent cells), tumor mass dormancy (small clusters with balanced proliferation and apoptosis) and metastatic growth (high proliferation and invasion). *Figure adapted from [7] with permission from Springer Nature.*

While survival rates are low (5-year survival rate of 27% in breast cancer[1]) in metastatic patients, therapeutic intervention before DTCs form aggressive secondary lesions could provide a better patient outlook. Fortunately, cancer dormancy provides a therapeutic "window of opportunity" to eliminate dormant cells or prevent their reactivation, and ultimately prevent metastatic relapse. A major limitation towards this goal is that current chemotherapeutics often fail to effectively treat dormant, quiescent cells.[15-20] This is likely due to a lack of understanding of the mechanisms that regulate the dormancy period between DTC infiltration of secondary organs and active

proliferation.[21-23] Thus, to develop new drugs and therapeutic strategies that target dormant cancer cells, there is an urgent need for simple platforms that can induce dormancy and reactivation *in vitro*. While dormant cells can be isolated from animal models, monitoring their response over time can be cumbersome due to limitations of current *in vivo* imaging modalities. However, *in vitro* platforms provide the resolution and spatiotemporal control to perform mechanistic studies that may aid in drug development. The work described in the following sections highlight our efforts towards preventing metastatic relapse by: (1) developing and characterizing a tunable, hydrogel-based breast cancer dormancy and reactivation platform, (2) implementing this platform to quantify dormant and reactivated cell chemosensitivity, (3) investigating mechanisms involved in dormant and reactivated cell chemoresistance, and (4) implementing a therapeutic strategy to increase drug efficacy in treating dormant and reactivated breast cancer *in vitro*.

Together, this work provides an easy-to-use hydrogel platform that can be applied to perform mechanistic studies that aid in drug development to prevent metastatic relapse. Furthermore, this platform can potentially be used to model other cancers known to undergo dormancy, prostate cancer and melanoma for example. This work also provides novel insight into breast cancer dormancy and reactivated cell chemoresistance that can be used in clinical settings for drug development. Towards this goal, we provide a therapeutic strategy that significantly increases drug efficacy in treating dormant and reactivated breast cancer cells *in vitro*. With further studies and optimization, this strategy has the potential to eliminate dormant cells *in vivo* and ultimately prevent reactivation and metastatic relapse.

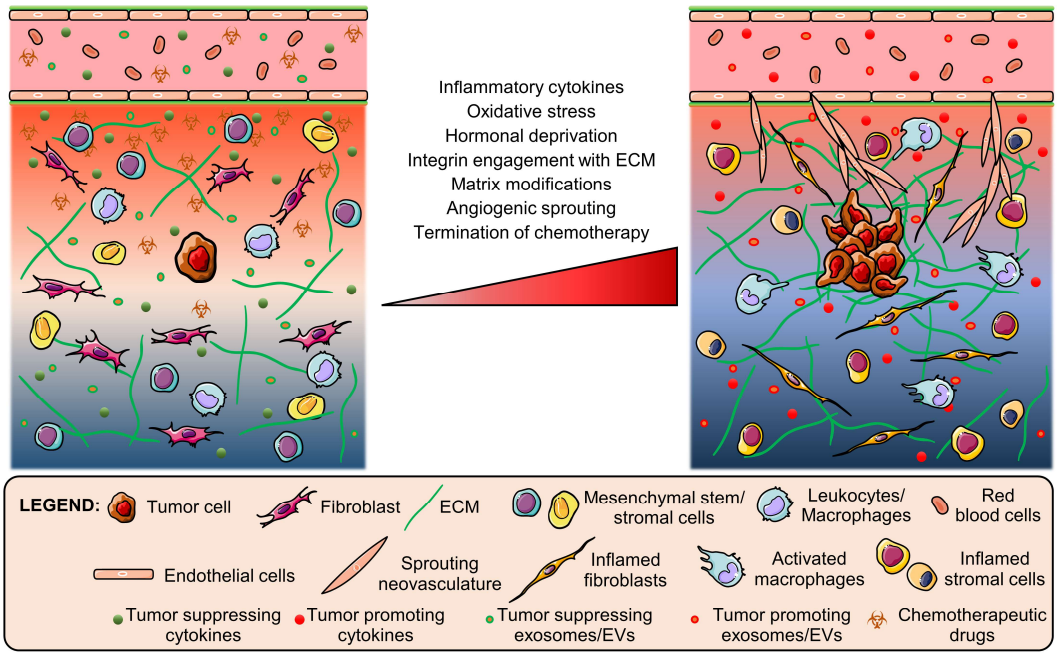

Figure 1.2: Factors Influencing Reactivation of Dormant Cancer Cells. Dormant tumor cells in the secondary niche can be stimulated or triggered toward metastatic growth via multiple sources including pro-inflammatory and angiogenic factors, paracrine signaling by stromal cells and sprouting vasculature, and dysregulated cell-matrix interactions amongst others. *Figure adapted from [7] with permission from Springer Nature.*

1.2 *In Vitro* Methods to Model Tumor Dormancy

To study dormant micrometastases and subsequent chemosensitivity, engineered systems that induce cancer dormancy *in vitro* have been developed by implementing multiple components found in the premetastatic niche that induce dormancy *in vivo* to achieve cell signaling-induced dormancy, biochemical-induced dormancy, drug-induced dormancy, and extracellular matrix (ECM)-induced dormancy (Figure 1.3).[7] In cell-signaling induced dormancy, co-culturing with secondary cell types such as mesenchymal stromal cells and endothelial cells can induce dormancy in multiple cancer types including triple negative MDA-MB-231s

and MCF7s.[14,24] Biochemical-induced dormancy has been achieved via hypoxia, nutrient deprivation, and soluble factors, which can lead to cell-cycle arrest or limited proliferation.[25,26] In drug-induced dormancy, cells are exposed to chemotherapies including doxorubicin, docetaxel, cyclophosphamide, 5-fluorouracil, methotrexate, cisplatin, bevacizumab, and trastuzumab.[7] Surviving, chemoresistant cells will often be in a dormant state. Many studies have used this method to obtain dormant cells *in vivo* and *in vitro*.[27-29] Studies have also demonstrated that the ECM can be tuned to induce cancer cell dormancy *in vitro*.[7,30-33] The studies in this dissertation implement ECM-induced dormancy (chapters 2, 3), but future studies that incorporate these alternative influences are of interest.

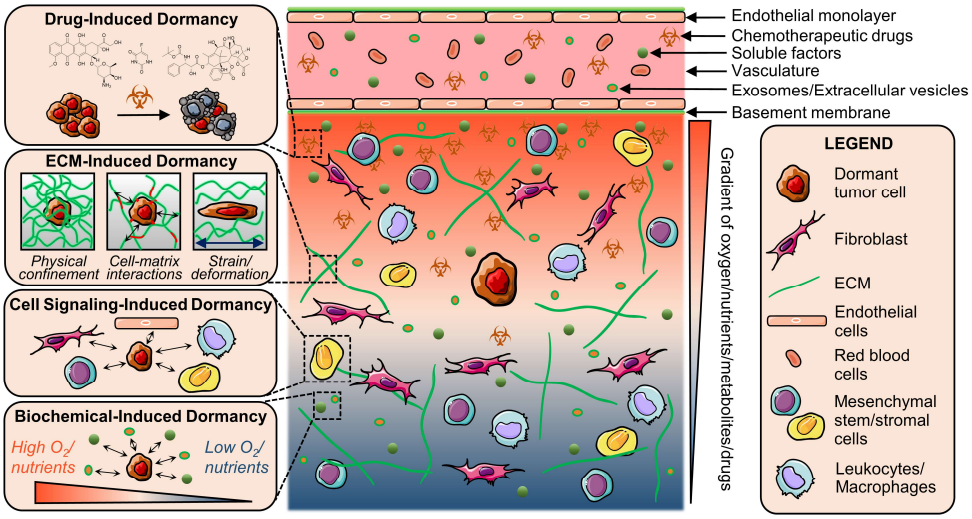

Figure 1.3: Modes of Dormancy Induction. Engineered, *in vitro* models of tumor dormancy can be classified based on the mode of dormancy induction: drug-induced dormancy (selective elimination and survival of sub-populations under chemotherapeutic treatment), ECM-induced dormancy (biophysical constraints imposed on cancer cells by the surrounding matrix), cell-signaling induced dormancy (paracrine signaling from stromal cells and vasculature) and biochemical-induced dormancy (influence of soluble factors, hypoxia and nutrients) amongst others. *Figure adapted from [7] with permission from Springer Nature.*

1.3 Influence of the Extracellular Matrix on Cancer Cell Fate and Dormancy

The role that microenvironmental properties of the premetastatic niche play in regulating dormancy has garnered significant interest.[7] In particular, the ECM has key biochemical and mechanical components which influence how a disseminated tumor cell interacts with its microenvironment. For instance, in a permissive microenvironment, the ECM provides matrix components (proteins, proteoglycans) that support cell adhesion via integrin-mediated adhesions and cell surface receptors. Subsequently, these adhesions trigger downstream intracellular pathways that modulate cancer cell fate including cell cycle progression and migration. Alternatively, when the ECM is not as permissive to integrin ligation or ligates different integrins, cancer cells may enter a state of dormancy. Remodeling of the dormant niche over time may permit engagement of dormant tumor cells with altered ECM and enable their escape from dormancy. However, there is still a poor understanding of the underlying mechanisms that induce and maintain cancer dormancy, as imaging resolution limitations that prevent dormant cells from being easily detected *in vivo* make it difficult to use animal models for development of therapeutics that target dormant micrometastases. Thus, studies have demonstrated that the ECM can be tuned to induce cancer cell dormancy *in vitro* using both natural and synthetic biomaterials (Figure 1.2).[7,30-33] Amongst several factors, physical confinement, cell-matrix interactions, and matrix strain/deformation have been manipulated to induce dormancy.[7]

1.4 Tuning Matrix Properties to Mimic Permissive and Non-Permissive Niches

To mimic permissive and nonpermissive ECMs, our group previously developed a suite of sixteen poly(ethylene glycol) (PEG)-based hydrogels with

varying biochemical (ligand density and degradability) and mechanical (elasticity, swelling, mesh size) properties.[34-36] In chapter 2, we describe three chosen formulations that induced three distinct phenotypes (growth, balanced cellular dormancy, and restricted survival cellular dormancy) in triple negative breast cancer cells, MDA-MB-231s (parental 231s) (Figure 2.1).[34-36]

Ligand density and matrix degradability were tuned via the concentration of PEG-RGDS (RGDS) and NVP, respectively, to mimic different ECMs DTCs may experience during early stages of secondary organ infiltration. Tuning PEG-RGDS concentration altered adhesive ligand density of the hydrogel matrix required for integrin-mediated cell adhesion and survival, and NVP incorporation increased the number of non-degradable crosslinks of the hydrogel matrix, inhibiting cell-mediated matrix degradation leading to increased physical confinement of encapsulated cells in their local niche. Permissive gel 1 (2.1 mM RGDS and 0 mM NVP) had high matrix (++) adhesivity and (++) degradability to mimic a favorable scenario in which cells can adhere to, and proteolytically degrade, their surrounding matrix. Non-permissive gel 2 (0.9 mM RGDS, 9.4 mM NVP) contained additional crosslinks (due to NVP) to generate a matrix with moderate (+) adhesivity but (+) low degradability. This mimics a scenario in which cells can adhere to their surrounding matrix but cannot degrade the ECM efficiently. Non-permissive gel 3 (0 mM RGDS, 0 mM NVP) had no (-) adhesivity but high (++) degradability. This mimics a scenario in which cells can degrade their matrix but cannot form integrin-mediated adhesions. The logic for this design is that enhancing cell-matrix interactions will form focal adhesions, leading to downstream signaling that promotes survival and proliferation. Alternatively, creating

unfavorable conditions by limiting cell-matrix interactions or the ability to degrade the matrix during growth may induce cells into dormancy.

1.5 ECM-Induced Dormancy and Reactivation in Breast Cancer

To develop a clinically relevant breast cancer dormancy and reactivation platform, key cell lines were chosen. Since breast cancers preferentially metastasize to the bone, lung, and brain,[37] genetically unique organotropic cells that also preferentially metastasize to bone (BoM-1833)[38], lung (LM2-4175)[39], or brain (BrM2a-831)[40] were implemented, along with the parental 231 line that these organotropic lines were derived from. We hypothesized that genetic signatures that promote organ-specific survival may also support sustained survival of dormant cells. The ER^+ breast cancer line, MCF7, was also utilized, as dormancy in ER^+ cancer can persist for over 20 years compared to ~2 years for ER^- breast cancers, providing an extended "window of opportunity" to eliminate dormant cells before being reactivated to form burdensome metastatic tumors. Therefore, in chapter 3, parental 231s, the three organotropic sublines, and MCF7s were all individually encapsulated in permissive gel 1, non-permissive gel 2, and non-permissive gel 3 for 15 days (Figure 2.1F).[34,35,41]

To characterize hydrogel-induced phenotype, we quantified the temporal change in number of viable cells, proliferating cells, and metabolic activity throughout the 15 day culture period as described in chapter 3.[41] We also determined the balance between newly formed live and dead cells, and proliferating (EdU^+) and apoptotic (Annexin V^+) cells at day 15. Other studies have also used viability, metabolic activity, proliferation, and other phenotypic assays to identify dormant cell populations.[7,42-44] Morphology and a p-ERK/p-38 ratio (dormancy predictor) was also

quantified. Permissive gel 1 (++ adhesivity, ++ degradability) promoted growth in all five cell lines. Favorable conditions led to large protruding clusters in parental 231s and organotropic sublines, and large rounded clusters in MCF7s with high levels of viability (>82.9%) and proliferation (>33.8%) (Figure 3.10). Removing all matrix adhesivity in non-permissive gel 3 restricted parental 231 and MCF7 survival (~40% viability), leading to restricted survival, cellular dormancy (Figure 3.10). Interestingly, organotropic 231 viability remained high (>88.5%) in non-permissive gel 3 and the cells were thus characterized as residing in balanced cellular dormancy (Figure 3.10). Reduced degradability in non-permissive gel 2 confined MCF7s, and bone- and brain-tropic cells into small clusters residing in balanced tumor mass dormancy, while parental 231s and lung-tropic lines remained as solitary, single cells in balanced cellular dormancy (Figure 3.10). Dynamic "on-demand" photocoupling of PEG-RGDS into non-permissive gel 3 at day 15 increased proliferation and viability in all five cell lines to levels comparable to cells in the growth state in permissive gel 1, indicating the ability to reactivate dormant cells via an external trigger (Figure 3.11). Together, these results demonstrated the ability to achieve growth, distinct dormancy states, and reactivation in parental 231s, organotropic sublines, and MCF7s.[41]

1.6 Chemoresistance in Dormant and Reactivated Breast Cancer

After thorough characterization, the *in vitro* dormancy and reactivation platform was implemented to quantify and compare the response of growing, dormant, and reactivated cells to common chemotherapeutics in chapter 4.[41,45] To measure drug response, parental 231s were encapsulated and cultured for 15 days to achieve growth (permissive gel 1) or dormancy (non-permissive gels 2 and 3), or 22 days (15 days in non-permissive gel 3 + 7 days post RGDS incorporation) to achieve reactivation, and

exposed to varying concentrations of common chemotherapeutics, doxorubicin (DOX), paclitaxel (PAC), and 5-fluorouracil (5-FU). Results showed significantly higher viability in dormant parental 231s in non-permissive gels 2 and 3 compared to growing cells in permissive gel 1 for all drugs tested (Figure 4.2, 4.4, 4.5). Due to low efficacy (Figure 4.1), we could not plot dose response curves for PAC and 5-FU. However, since DOX studies showed overall greater efficacy (Figure 4.1), we were able to obtain dose response curves and calculate half maximal effective concentration (EC_{50}) and half maximal inhibitory concentration (IC_{50}) values. Higher EC_{50} and IC_{50} values correspond with enhanced chemoresistance, as they indicate that higher concentrations were required to induce cytotoxicity. Since we were able to obtain pertinent EC_{50} and IC_{50} values, DOX studies were expanded to investigate the drug response of parental 231s, organotropic sublines, and ER^+ MCF7s in a growth, dormant, or reactivated state. Results indicated that all dormant populations (non-permissive gels 2 and 3) displayed increased chemoresistance to DOX, compared to growing cells in permissive gel 1 in all five cell lines (Figure 4.5, 4.6). For example, growing parental 231s in permissive gel 1 had an EC_{50} of 44.9 ± 6.2 μM, while dormant parental 231s in non-permissive gels 2 and 3 had significantly higher EC_{50} values of 65.5 ± 7.7 μM (non-permissive gel 2) and 82.9 ± 14.5 μM (non-permissive gel 3) (Figure 4.5, 4.6). Similar trends were observed in organotropic sublines and MCF7s. Interestingly, while reactivated cells had similar viability and proliferation values as cells in permissive gel 1, reactivated populations displayed significantly greater EC_{50} values than both growing and dormant cells in all cell lines tested. For instance, reactivated parental 231s had an EC_{50} of 113.0 ± 15.7 μM, compared to values ranging from ~44-83 μM in growing and dormant 231s (Figure 4.5, 4.6).

To investigate if DOX uptake correlated with increased chemoresistance, intracellular DOX accumulation was measured over 48 hr and plotted to determine the accumulation rate. Results indicated that chemoresistant dormant (non-permissive gels 2 and 3) and reactivated cells had significantly lower accumulation rates compared to chemosensitive cells in permissive gel 1 (Figure 4.7). For instance, DOX accumulated at a rate of 112.8 ± 10.1 h^{-1} in permissive gel 1, compared to 100.5 ± 7.7 in non-permissive gel 2 (dormant), 97.2 ± 9.4 in non-permissive gel 3 (dormant), and 76.6 ± 1.7 h^{-1} in reactivated cells (Figure 4.7). Similar trends were observed for organotropic and MCF7 cell lines. We also quantified the NC ratio to determine DOX nuclear localization after 48 h exposure and observed significantly greater nuclear localization in chemosensitive cells in permissive gel 1, compared to dormant and reactivated cells for all cell lines (Figure 4.8).

Overall, this data demonstrated that both dormant and reactivated populations acquire chemoresistance to DOX. Results highlight that while reactivated cells have similar phenotypic behavior as growing cells in permissive gel 1, they have unique chemoresistance that may have been acquired during entry into dormancy or exit out of dormancy and into reactivated growth. These results also suggest that acquired dormancy and reactivated chemoresistance may be due to decreased DOX intracellular accumulation and subsequent localization to the nucleus. These findings provide valuable insight that can be used to develop novel drugs and therapeutic strategies that target dormant and reactivated cells.

1.7 Influence of Efflux Pump Expression on Chemoresistance

Based on findings that indicate DOX transport may play a role in dormant and reactivated cell chemoresistance, we next aimed to understand what mechanisms

regulate DOX transport in chemoresistant cells in chapter 5. Since ATP-binding cassette (ABC) efflux pumps have been established as key factors in cancer chemoresistance, we investigated expression of three clinically relevant efflux pumps: ABCB1 (P-gp)[46,47], ABCC1 (MRP1),[48,49] and ABCG2 (BCRP).[50,51] Our goals were: (1) to determine whether parental 231s, organotropic sublines, and MCF7s expressed these efflux proteins, and (2) if expressed, to determine whether chemoresistant dormant or reactivated populations expressed significantly higher levels of these efflux pump proteins. Our results showed that all five cell lines expressed levels of P-gp, MRP1, and BCRP, however chemoresistant dormant (non-permissive gels 2 and 3) and reactivated cells tended to express significantly higher levels compared to chemosensitive growing cells in permissive gel 1 (Figure 5.1-5.6). For instance, parental 231s expressed significantly greater levels of MRP1 in dormant cells (non-permissive gel 2: 0.71 ± 0.15, non-permissive gel 3: 0.93 ± 0.23) than growing cells in permissive gel 1 (0.15 ± 0.04) (Figure 5.6). Furthermore, reactivated parental 231s had the highest MRP1 expression of 1.88 ± 0.21 (Figure 5.6). While similar trends were observed in organotropic sublines, BCRP expression was not significantly different between growing, dormant, or reactivated MCF7s.

In most cases, efflux pumps P-gp, MRP1, and BCRP were overexpressed in chemoresistant dormant and reactivated cells. To investigate whether these efflux pumps played a role in chemoresponse, DOX drug studies were performed with efflux pump inhibition using a P-gp inhibitor (10 nM tariquidar), MRP1 inhibitor (50 μM MK571), BCRP inhibitor (10 μM Ko 143), or a combination of all three inhibitors on parental 231s, brain-tropic 231s, and MCF7s. Note, BCRP was not tested for MCF7s since BCRP was not overexpressed in dormant or reactivated MCF7s. Results showed

that inhibiting these efflux pumps significantly increased chemosensitivity, quantified by significant decreases in EC_{50} values. In many cases efflux pump inhibition decreased dormant and reactivated cell EC_{50} values below those of growing cells in permissive gel 1 (Figure 5.9). For instance, P-gp+MRP1+BCRP inhibition decreased EC_{50} values to 4.2 ± 1.1 μM (permissive gel 1, ~11-fold decrease), 0.4 ± 0.1 μM (non-permissive gel 2, ~170-fold decrease), 1.1 ± 0.5 μM (non-permissive gel 3, ~81-fold decrease), and 1.4 ± 0.3 μM (reactivated, ~81-fold decrease) compared to no inhibition, with significantly lower EC_{50} values in previously chemoresistant dormant and reactivated cells (Figure 5.9). DOX accumulation and nuclear localization studies confirmed that efflux pump inhibition significantly increased the accumulation rate (~3-11-fold increase) and NC ratio (~1.2-3.2-fold increase) in all cell lines tested (Figure 5.11-5.15). In particular, efflux pump inhibition resulted in significantly greater accumulation rates and, in many cases, significantly greater NC ratios in dormant and reactivated cells compared to growing cells in permissive gel 1.

Overall, this data provides novel insights into dormant and reactivated cell chemoresistance. Results indicate that chemoresistant dormant and reactivated cells overexpress P-gp, MRP1, and BCRP, and that their inhibition significantly increases DOX efficacy by increasing intracellular accumulation rate and nuclear localization. These findings suggest a mechanism involved in dormant and reactivated cell chemoresistance and provides a potential therapeutic strategy to target and eliminate dormant cells during breast cancer latency to help prevent metastatic relapse.

Chapter 2

3D HYDROGELS WITH TUNABLE ADHESIVITY AND DEGRADABILITY TO MIMIC PERMISSIVE AND NON-PERMISSIVE NICHES

Sections in this chapter have been adapted from the following articles:

(1) Farino CJ, Pradhan S, Slater JH. The Influence of Matrix-Induced Dormancy on Metastatic Breast Cancer Chemoresistance. ACS Applied Biomaterials 2020, 3(9), 5832-5844.

(2) Farino Reyes CJ, Pradhan S, Slater JH. The Influence of Ligand Density and Degradability on Hydrogel Induced Breast Cancer Dormancy and Reactivation. Advanced Healthcare Materials 2021, 10(11), 2002227.

2.1 Introduction

Despite improvements in cancer prevention, detection, and treatment, metastasis remains a serious threat.[1,52] During metastasis, disseminated tumor cells (DTCs) originating from a primary tumor extravasate into secondary organs. In many cases, there is a latency period ranging anywhere from a few months to several decades prior to metastatic relapse that is explained by tumor dormancy.[3,4,7,52] During dormancy, DTCs may enter cellular dormancy, characterized by solitary cells that survive in cell-cycle arrest via anti-apoptotic mechanisms, or tumor mass dormancy, characterized by clustered cells residing in a balanced state of proliferation and apoptosis.[3,9,10] Metastatic relapse can occur when dormant cells undergo a phenotypic switch to resume proliferation and invasive growth.[53] The advantage of this latency period is that it provides a potential therapeutic "window of opportunity" lasting up to

decades in which eliminating dormant DTCs or preventing their reactivation can be used to prevent metastatic recurrence. However, current chemotherapeutics that target proliferating cancer cells, fail to efficiently eliminate quiescent, dormant DTCs.[15,45] Towards this effort, *in vitro* platforms that induce dormancy and reactivation are necessary to investigate cancer dormancy at a resolution that provides mechanistic understanding at the cellular level to increase chemotherapeutic efficacy.

A general understanding of the factors involved in tumor dormancy has led to the development of *in vitro* models that induce dormancy via multiple factors found in the premetastatic niche which can induce dormancy *in vivo*.[7] For instance, incorporation of immune responses, stromal cell signaling, and nutrient deprivation have all been applied to induce dormancy.[7] Another key factor in regulating DTC fate are the microenvironmental cues provided by the extracellular matrix (ECM). When cancer cells fail to establish integrin-mediated adhesions to ECM proteins in unfavorable conditions, downstream signaling may lead to dormancy.[54] Using this logic, we previously implemented a suite of sixteen unique hydrogel formulations containing well-controlled, systematic variations in ligand and crosslinking density using three components:[35] (1) a proteolytically degradable, poly(ethylene glycol) (PEG)-based, diacrylate macromer containing the peptide sequence, GGGPQGIWGQGK (PQ), cleavable by cell-secreted matrix metalloproteinases-2 and -9, flanked on either side by a PEG with a terminal acrylate (PEG-PQ), (2) a mono-acrylated integrin-ligating peptide (RGDS) that contained a PEG with a terminal acrylate attached to the N-terminus (PEG-RGDS), and (3) a non-enzymatically degradable co-monomer N-vinyl pyrrolidone (NVP) that facilitates crosslinking. The suite of hydrogels was implemented to systematically investigate the influences of

ligand density and hydrogel degradability, elasticity, and pore size on regulating the fate of the triple negative, MDA-MB-231 parental line with respect to growth and dormancy phenotypes.[35] The results demonstrated that ligand density and hydrogel degradability had a greater influence on the resultant phenotype compared to hydrogel elasticity and pore size.[35]

We implemented three of the sixteen hydrogel formulations that induced growth and distinct forms of dormancy in parental 231s[34-36] to further characterize how altering ligand (RGDS) density and hydrogel degradability influence the phenotype of the parental 231 line and to quantify the response of three organotropic sublines that preferentially metastasize to the bone, lung, or brain, as well as the ER^+ breast cancer cell line, MCF7 in chapters 2 and 3 (Figure 2.1).[41] In this chapter, we characterize the hydrogels used in these studies by measuring key properties known to influence cell phenotype. Matrix adhesivity and degradability were tuned via RGDS and NVP concentration in three hydrogel formulations that represented different premetastatic niches. RGDS provides adhesive ligands, while NVP increases hydrogel crosslinking density via addition of non-enzymatically degradable crosslinks through its acrylate side groups.[35,55,56] Permissive gel 1 was composed of 2.1 mM RGDS, 0 mM NVP (++ adhesivity and ++ degradability) and mimicked a favorable niche to promote tumor growth in which cells are able to adhere and degrade their surrounding matrix. Non-permissive gel 2 was composed of 0.9 mM RGDS, 9.4 mM NVP (+ adhesivity, + degradability) and mimicked a unfavorable niche in which cells can adhere to their matrix but do not express the proteases required to enzymatically degrade the matrix. Non-permissive gel 3 was composed of 0 mM RGDS, 0 mM NVP (- adhesivity, ++ degradability) and mimicked a case in which cells can degrade their

matrix but fail to form focal adhesions. The matrices were chosen on the logic that a favorable ECM will likely promote growth and proliferation, while an unfavorable ECM (via confinement or lack of adhesion) will promote dormancy (chapter 3).

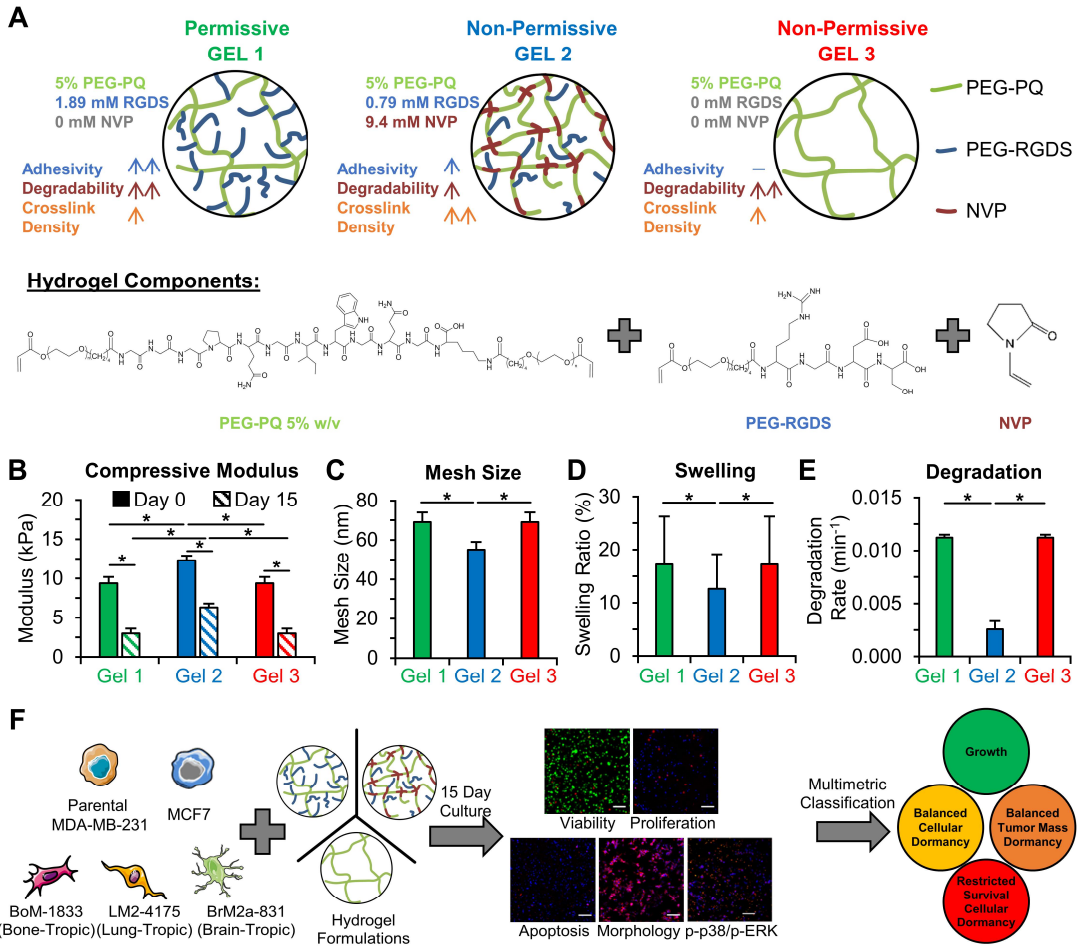

Figure 2.1: Hydrogel Characterization and Experimental Workflow. (A) Schematic of three hydrogel formulations with tunable adhesivity, degradability, and crosslink density (permissive gel 1, non-permissive gel 2, non-permissive gel 3). Chemical structures of hydrogel components: PEG-PQ, PEG-RGDS, and n-vinyl pyrrolidinone (NVP). Quantification of the (B) compressive modulus of cell-laden hydrogels at day 0 (solid) and 15 (striped), (C) mesh size, (D) swelling ratio, and (E) degradation rate. * indicates $p<0.05$. n=4 hydrogels per condition. Values represent mean + standard deviation. (F) Schematic of the experimental workflow involving culture of five breast cancer cell lines within three different hydrogel formulations, quantification of cellular behavior, and implementation of multimetric classification of hydrogel-induced cellular phenotypes. *Figure reproduced from [41] with permission from John Wiley and Sons.*

In this chapter, we characterized hydrogel properties by measuring metrics known to influence cell phenotype including RGDS incorporation efficiency and final concentration, elastic modulus, mesh size, swelling ratio, and degradation rate.[41] In summary, we found that permissive gel 1 and non-permissive gel 3 had a compressive modulus of 4.2 ± 0.6 kPa, a mesh size of 69 ± 5 nm, degradation rate of (0.0125 ± 0.0006 min^{-1}), and a swelling ratio of 17 ± 9 (Figure 2.1). NVP incorporation in non-permissive gel 2 led to a modulus of 7.6 ± 0.8 kPa, mesh size of 55 ± 4 nm, degradation rate of 0.0081 ± 0.0016 min^{-1}, and swelling ratio (13 ± 6). Additionally, NVP incorporation increased RGDS incorporation in non-permissive gel 2. Overall, these findings quantify how altering hydrogel composition alter hydrogel mechanical and chemical properties, which can have significant influence on cancer cell phenotype, which is explored in the next chapter.

2.2 Methods

2.2.1 Cell Culture

The metastatic, triple negative breast cancer line, MDA-MB-231 (parental 231), was purchased from American Type Culture Collection (ATCC). Cells were cultured (passage (p) 35-40) in fibronectin coated (10 μg/mL) T75 flasks with Dulbecco's Modified Eagle Medium (DMEM: Lonza C#12-741F) supplemented with 10% (v/v) fetal bovine serum (FBS: Thermo Fisher C#16000044) and 1% (v/v) penicillin-streptomycin (Lonza C#DE17-602E) to 80% confluence at 37 °C and 5% CO_2. Prior to encapsulation in hydrogels, cells were serum starved in serum-free DMEM for 48 h to synchronize the cell cycle.[35,36,41]

2.2.2 PEG Macromer Synthesis and Characterization

The proteolytically-degradable PEG-diacrylate macromer, PEG-PQ-PEG (PEG-PQ), and the integrin-ligating mono-acrylated macromer, PEG-RGDS, were synthesized as previously described.[34-36] Briefly, acrylate-PEG-SVA (MW: 3400 Da, Laysan Bio C#3400-1g) was reacted with a proteolytically degradable peptide sequence GGGPQG↓IWGQGK (PQ, MW: 1141.24 Da, Biopeptek, ↓ denotes cleavage site by matrix metalloproteinase-2 and -9) at a 2.1:1 molar (M) ratio (PEG-SVA:peptide) in dimethyl sulfoxide (DMSO) with N,N-diisopropylethylamine (DIPEA) at a 4:1 M ratio (DIPEA:PQ) at room temperature for 48 h to form the PEG-PQ macromer. Acrylate-PEG-SVA was reacted to the integrin-ligating peptide sequence RGDS (MW: 433.42 Da, Biopeptek) at a 1.1:1 M ratio (PEG-SVA: peptide) in DMSO with DIPEA at a molar ratio of 2:1 (DIPEA:RGDS) to form the PEG-RGDS macromer. All reacted products were purified via dialysis (DI water, 24 h) (MWCO 3500, Regenerated Cellulose, Spectrum Laboratories C#25223-210), frozen, lyophilized, and stored at −80 °C under argon. PEG-peptide conjugation was verified via gel permeation chromatography (GPC, Waters, aqueous phase).

2.2.3 Cell Encapsulation

Formulations that induced growth, balanced cellular dormancy, or restricted survival cellular dormancy in the parental 231 line were prepared as previously described.[34-36] PEG-PQ (MW: 7900 Da) was reconstituted in phosphate-buffered saline (PBS) to a final concentration of 5% weight/volume (w/v) (6.3 mM) for all hydrogel formulations. PEG-RGDS was reconstituted in PBS to final concentrations of 10 mM (permissive gel 1) or 1 mM (non-permissive gel 2). Non-permissive gel 3 contained 0 mM PEG-RGDS. For non-permissive gel 2, NVP was added to PEG-PQ

and PEG-RGDS precursor solutions to a final concentration of 1.0 μL/mL (9.4 mM) prior to photopolymerization. Lithium phenyl-2,4,6-trimethylbenzoylphosphinate (LAP), a UV-sensitive photocrosslinker, was added to all formulations at a final concentration of 3.0 mg/mL (10 mM). Cells were trypsinized, counted, and re-suspended in the desired pre-polymer solution at a concentration of 10 million cells/mL. Cell-laden precursor solutions were pipetted (3 μL) onto a perfluoro alkoxy alkane (McMaster-Carr) coated Petri dish. To control hydrogel height, a glass slide was gently placed over the droplets with 500 μm thick poly(dimethylsiloxane) (PDMS) spacers between the slide and Petri dish. Hydrogels were photopolymerized via exposure to broad spectrum UV (Blak-Ray flood UV lamp, wavelength: 365 nm, intensity: 10 mW/cm^2) for 1 min. Cell-laden hydrogels were cultured in well plates for 15 days in DMEM supplemented with 10% (v/v) FBS and 1% (v/v) penicillin-streptomycin. Media was replaced every 4 days.

2.2.4 PEG-RGDS Incorporation

To determine the concentration of PEG-RGDS that was photocoupled into PEG-PQ hydrogels with either 0 mM NVP and 10 mM PEG-RGDS, or 9.4 mM NVP and 1 mM PEG-RGDS, fluorescence analysis was implemented (n=4 hydrogels per condition) as previously described (Figure 2.2).[34-36] Briefly, pre-polymer solutions containing a fluorescent PEG variant, PEG-RGDS functionalized with Alexa Fluor 488 (PEG-RGDS-488) at a concentration of 0.5 mM PEG-RGDS-488 with adjusted PEG-RGDS concentrations of 9.5 and 0.5 mM were prepared. To account for photobleaching, pre-polymer solutions were imaged before photopolymerization and immediately after, using a Zeiss AxioObserver Z1 inverted fluorescent microscope. Hydrogels were soaked in PBS overnight to allow swelling and to rinse away

unconjugated PEG-RGDS and PEG-RGDS-488. Rinsed hydrogels were imaged and measurements comparing the intensity of PEG-RGDS-488 before and after rinsing were made to determine the conjugation efficiency and concentration of PEG-RGDS incorporated into the hydrogels as previously described.[34-36]

2.2.5 Mesh Size

Hydrogel mesh size was calculated via diffusion of 150 kDa fluorescein isothiocyanate (FITC)-labeled dextran (Thermo Fisher) as previously described (Figure 2.3).[34-36] After reaching swelling equilibrium in DI water, PEG-PQ hydrogels containing 0 or 9.4 mM NVP (n=4 hydrogels per condition) were transferred to solutions containing 1 mg/mL, 150 kDa FITC-labeled dextran for 48 h at 4 °C. Hydrogels were transferred into new well plates with DI water. Samples of DI water containing dextran that diffused out of the hydrogels were collected every 15 min for 4 h and measured with a plate reader (Biotek Synergy, Excitation: 490 nm, Emission: 525 nm). Equal volumes of water were added to the wells at each timepoint. Fluorescence intensities were used to determine the cumulative mass of dextran that was released over time. Using the hindered solute diffusion in solvent-filled-pores-model, these values were used to calculate the hydrogel diffusion coefficient and theoretical mesh size as previously described.[34-36]

2.2.6 Compressive Modulus

A Universal Testing System 3340 Series (Instron) was used to measure the compressive modulus of cylindrical (3 mm diameter, 1 mm tall) cell-laden, 5% (w/v) PEG-PQ hydrogels with 0 or 9.4 mM NVP as previously described (Figure 2.4).[34-36] Compression tests were performed at day 0 (6 h) and day 15-post cell encapsulation

(n=3 hydrogels per condition) using a 10 N load cell with an initial load of 0.02 N at 2 μm/sec for 100 sec. The slope of the linear portion (within 20% strain) of the resulting stress-strain curve was used to determine the compressive modulus.

2.2.7 Swelling Ratio

To determine the hydrogel swelling ratio, PEG-PQ hydrogels containing 0 or 9.4 mM NVP (n=4 hydrogels per condition) were photopolymerized, allowed to swell to equilibrium, stored overnight in PBS, and weighed. The hydrogels were dried for 6 h in ambient air and reweighed. Differences in measured weights were used to calculate the swelling ratio as previously described (Figure 2.5).[34-36]

2.2.8 Degradation Rate

The hydrogel degradation rate was measured using collagenase IV (Worthington, 250 U/mg). PEG-PQ hydrogels with 0 or 9.4 mM NVP were photopolymerized in the presence of 1 mM methacryloxyethyl thiocarbamoyl rhodamine B (Polysciences) (n=3 hydrogels per condition) as previously described.[34-36] The hydrogels were incubated at 37 °C in 100 μg/mL collagenase IV and imaged every 15 min for 3 h. FIJI software (NIH, 1.51r) was used to measure the hydrogel fluorescence intensity over time (Figure 2.6). The slope of the linear relationship between hydrogel intensity and time was measured to determine the degradation rate. Hydrogels not exposed to collagenase were used as controls to account for any photobleaching that may have occurred.

2.2.9 Statistical Analysis

Statistical analysis was performed using Minitab 17 Statistical Software (Minitab Inc.) Data represent the mean + plus one standard deviation. An Anderson-

Darling test and a Levene's test was used to test assumptions of normality and equality of variance among groups respectively ($p>0.05$). One-way analysis of variance (ANOVA) was used for statistical comparison between values, with Tukey family error = 5% implemented to determine statistical significance between multiple groups, assuming equal sample size. ANOVA analysis was followed with a Howell post-hoc test in cases of unequal variance. A 2-sample t-test was used for statistical comparison between two variables. Unless otherwise indicated, $p < 0.05$ was considered statistically significant.

2.3 Results

2.3.1 PEG-RGDS Incorporation

We implemented three unique, PEG-based hydrogel formulations composed of a proteolytically-degradable PEG-PQ macromer which can be enzymatically degraded by matrix metalloproteinase-2 and -9 and forms the backbone of the polymers used in this study. We also incorporated varying concentrations of the integrin ligating peptide (RGDS) and the non-degradable co-monomer (NVP) (Figure 2.1) to induce phenotypic changes in breast cancer cell lines.[38-40] Ligand (RGDS) density influences a cell's ability to interact with the hydrogel via integrin-mediated adhesions. Incorporation of NVP increases the density of non-enzymatically degradable crosslinks in the hydrogel network thereby increasing cell confinement by lowering matrix degradability. In our previous work,[35] we implemented a suite of 16 hydrogel formulations with varying concentrations of PEG-RGDS (0-10 mM) and NVP (0-18.7 mM). Of these formulations, we chose three which induced distinct growth and dormant states in parental MDA-MB-231s through controlled variations in ligand

density and degradability to mimic favorable (permissive gel 1) and unfavorable (non-permissive gel 2 and non-permissive gel 3) premetastatic niches. Permissive gel 1, composed of 2.1 mM PEG-RGDS and 0 mM NVP, mimics a favorable pre-metastatic niche that induces growth via a high level of integrin ligation and matrix degradability (Figure 2.1). Non-permissive gel 2, composed of 0.9 mM PEG-RGDS and 9.7 mM NVP, mimics a less favorable pre-metastatic niche via decreased ligand density and degradability compared to permissive gel 1, mimicking conditions where DTCs are confined and unable to locally degrade or remodel the surrounding matrix (Figure 2.1). Non-permissive gel 3, composed of 0 mM PEG-RGDS and 0 mM NVP, restricted cell-matrix interactions due to the non-existence of RGDS (Figure 2.1) but maintained high degradability again mimicking a less favorable pre-metastatic niche due to the decreased RGDS density. A low or zero PEG-RGDS concentration mimics a microenvironment in which disseminated tumor cells (DTCs) cannot form integrin-mediated adhesions, while NVP incorporation resulting in reduced hydrogel degradation mimics an environment in which DTCs cannot easily degrade the surrounding matrix.

To quantify the effect of tuning RGDS and NVP concentrations on resulting hydrogel properties, we measured metrics known to influence cell phenotype including the RGDS concentration, elastic modulus, mesh size, swelling ratio, and degradation rate.[41] To measure RGDS incorporation, hydrogels were prepared with fluorescent PEG-RGDS-488 and imaged. Intensity measurements before and after crosslinking were used to determine RGDS incorporation in each formulation. Results showed that incorporation efficiency increased from 20.7 ± 6.6% without NVP to 90.4 ± 9.3% with NVP (Figure 2.2). Furthermore, while 10 mM PEG-RGDS was added to

the permissive gel 1 precursor, the actual RGDS concentration in the matrix was 2.1 ± 0.7 mM. Due to high incorporation with NVP, of the 1 mM RGDS that was added to the non-permissive gel 2 precursor, 0.9 ± 0.1 mM RGDS was incorporated into the matrix (Figure 2.2). Non-permissive gel 3 contained 0 mM PEG-RGDS. Increased PEG-RGDS incorporation in the presence of NVP is likely due to the increased number of available acrylate groups during photopolymerization as previously described.[34-36,41]

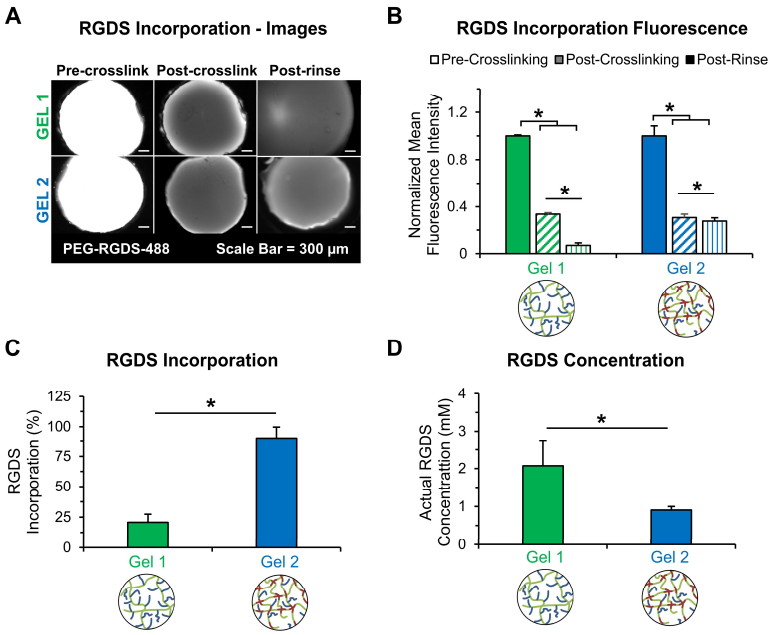

Figure 2.2: Quantification of PEG-RGDS Incorporation. (A) Representative fluorescent images of the hydrogel precursor before crosslinking (left column), the photopolymerized hydrogel immediately after crosslinking (middle column), and post-rinse in phosphate buffered saline (right column) for gels with NVP (gel 2) and without NVP (gel 1). Scale bar = 300 µm. Quantification of (B) the normalized mean fluorescence intensity pre-crosslinking, post-crosslinking, and post-rinse, (C) RGDS incorporation, and (D) actual RGDS concentration in gels with NVP (gel 2) and without NVP (gel 1). * indicates statistically significant difference ($p<0.05$). n=6 from 6 individual hydrogels. Values represent mean + standard deviation.

2.3.2 Mesh Size

To determine how varying NVP and RGDS concentration influenced hydrogel mesh size, 150 kDa FITC-dextran was added to hydrogels with and without NVP. Fluorescence intensity measurements quantifying dextran diffusion was used to calculate diffusion coefficient and mesh size.[41] Formulations without NVP (permissive gel 1, non-permissive gel 3) had a diffusion coefficient of $1.01 \times 10^{-7} \pm 6.55 \times 10^{-9}$ cm^2/s and mesh size of 69 ± 5 nm. In non-permissive gel 2, diffusion coefficient and mesh size decreased significantly to $8.02 \times 10^{-8} \pm 5.21 \times 10^{-9}$ cm^2/s and 55 ± 4 nm, respectively (Figure 2.3). These findings are likely explained by additional number of crosslinks resulting from NVP which can create a more constricting matrix.

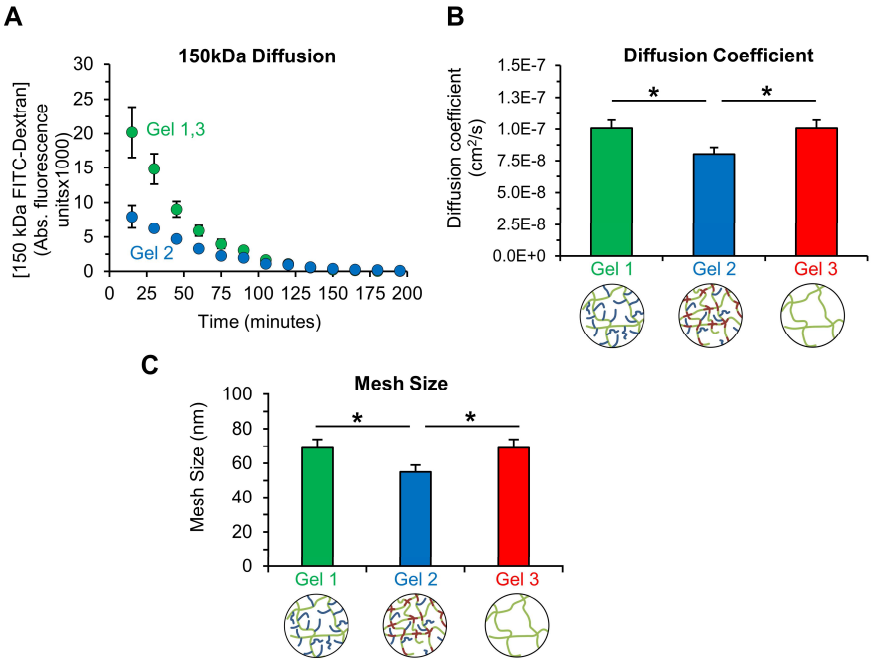

Figure 2.3: Quantification of Hydrogel Diffusion and Mesh Size. (A) Absorbance fluorescence of hydrogels with (gel 2) or without NVP (gel 1,3) over time. Quantification of (B) diffusion coefficient, and (C) theoretical mesh size. * indicates statistically significant difference ($p<0.05$). n=4 from 4 individual hydrogels. Values represent mean + standard deviation. *Figure adapted from [41] with permission from John Wiley and Sons.*

2.3.3 Hydrogel Elasticity

Hydrogel elasticity was measured to determine how bulk modulus changed with NVP incorporation, as well as with and without cells using compression testing.[41] In acellular hydrogels, hydrogels without NVP (permissive gel 1 and non-permissive gel 3) had an elastic modulus of 6.5 ± 0.3 kPa, while hydrogels containing 9.4 mM NVP (non-permissive gel 2) had an elastic modulus of 11.6 ± 0.5 kPa (Figure 2.4). As expected, increasing the number of crosslinks via NVP incorporation increased hydrogel elasticity. In the presence of cells, the elastic modulus decreased to 4.6 ± 0.4 and 10.1 ± 0.5 kPa in hydrogels with 0 mM NVP (permissive gel 1 and non-permissive gel 3) and 9.4 mM NVP (non-permissive gel 2) at day 0 (6 h post encapsulation), respectively (Figure 2.4).

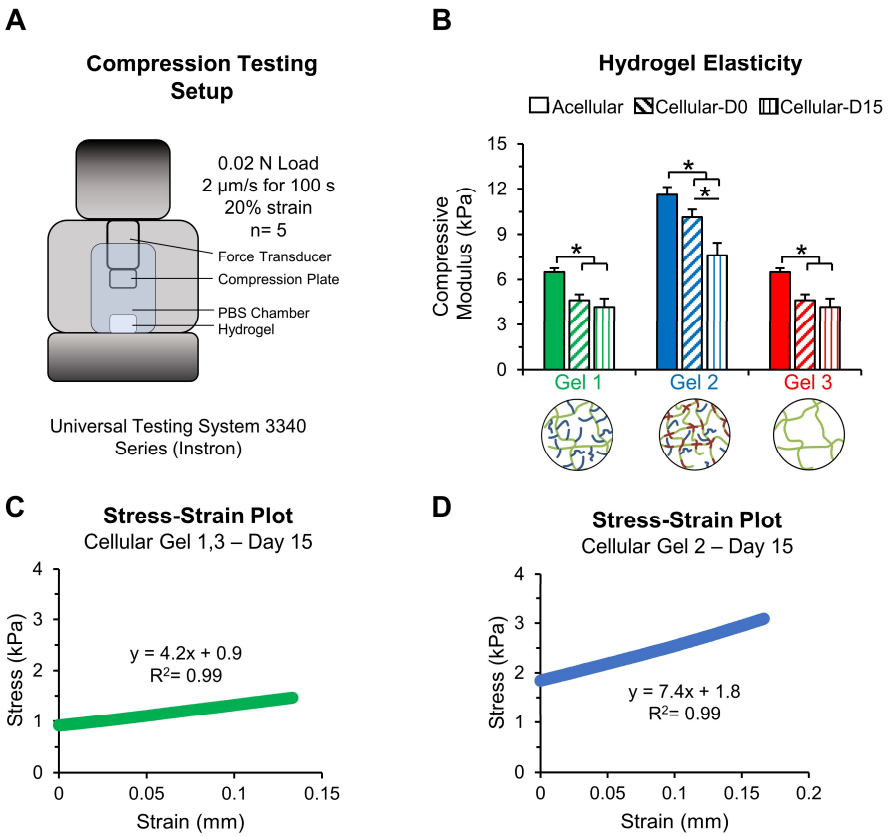

Figure 2.4: Quantification of Hydrogel Elasticity. (A)Schematic of mechanical testing setup. (B) Quantification of compressive modulus of acellular hydrogels and cell-laden hydrogels at day 0 (striped) and day 15 (striped). Representative stress-strain plots of (C) gels without NVP at day 15, and (D) gels with NVP at day 15. * indicates statistically significant difference ($p<0.05$). n=5 from 5 individual hydrogels. Values represent mean + standard deviation. *Figure adapted from [41] with permission from John Wiley and Sons.*

After culturing cell-laden hydrogels for 15 days, the elastic modulus further decreased to 4.2 ± 0.6 kPa (0 NVP) and 7.6 ± 0.8 kPa (9.4 mM NVP). Cell-mediated hydrogel degradation likely accounts for the observed decreases in elastic modulus over the 15-day culture period. The elastic modulus values are similar to those previously reported in PEG-PQ hydrogels.[35,41,57-59]

2.3.4 Swelling Ratio

Hydrogel swelling ratio can indicate how much water enters the hydrogel before reaching equilibrium. To quantify swelling ratio in the three hydrogels, sample mass was measured in its swollen and dry state.[41] Without NVP (permissive gel 1, non-permissive gel 3), sample mass decreased from (swollen) 3.7 to (dry) 0.2 mg, resulting in a swelling ratio of 17.3 ± 0.9 (Figure 2.5). Addition of NVP in non-permissive gel 2 dropped mass from (swollen) 2.7 mg to (dry) 0.2 mg, resulting in a significantly lower swelling ratio of 12.6 ± 0.6 (Figure 2.5). These results are consistent with mesh size and compressive modulus findings.

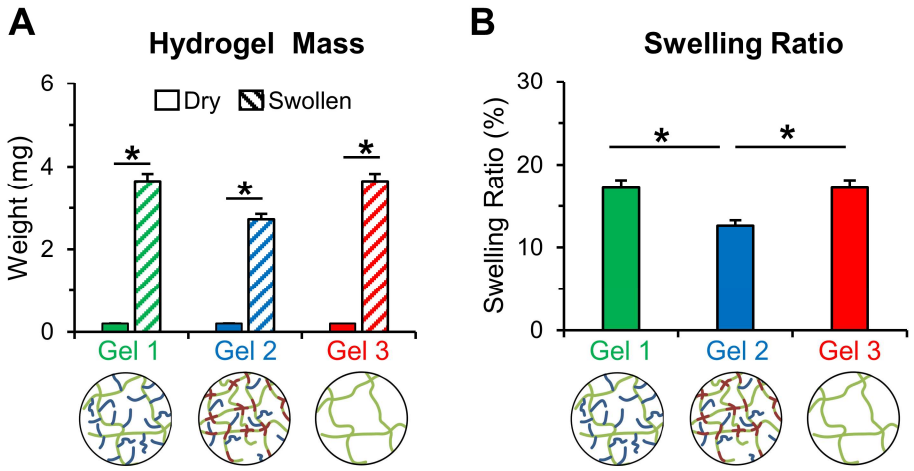

Figure 2.5: Quantification of Swelling Ratio. (A) Mass of dry hydrogel (solid) and swollen hydrogel (striped) for gel 1, 2, and 3. (B) Quantification of swelling ratio of gel 1, 2, and 3. * indicates statistically significant difference ($p<0.05$). n=4 from 4 individual hydrogels. Values represent mean + standard deviation. *Figure adapted from [41] with permission from John Wiley and Sons.*

2.3.5 Degradation Rate

To determine how NVP incorporation altered overall hydrogel degradability, hydrogel enzymatic degradation via 100 μg/mL collagenase IV was quantified over time. Hydrogels without NVP degraded at a rate of 0.0125 ± 0.0006 min^{-1} and achieved 100% degradation in 80 min (Figure 2.6). Hydrogels with NVP had a significantly lower degradation rate of 0.0081 ± 0.0016 min^{-1} and achieved ~80% degradation in 120 min (Figure 2.6).

Together, tuning hydrogel degradability via NVP incorporation and matrix adhesion via RGDS density can alter cell-mediated hydrogel degradation and adhesion to influence cell phenotype as demonstrated in the following chapter 3.

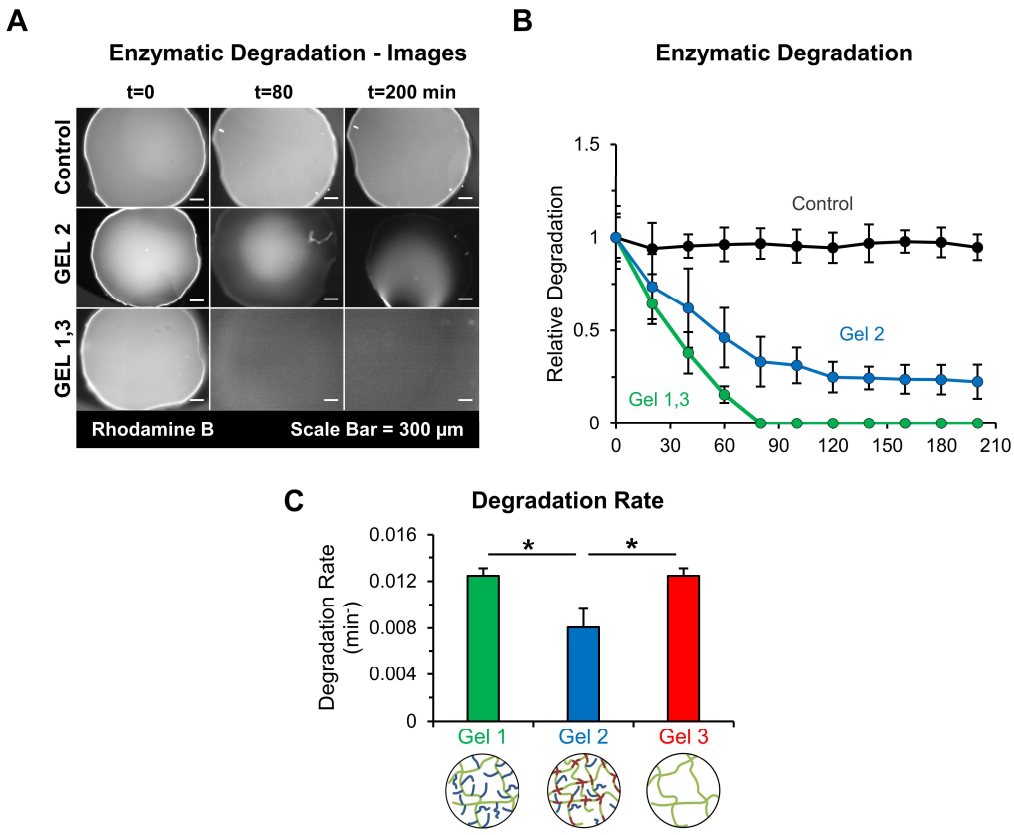

Figure 2.6: Quantification of Hydrogel Degradability. (A) Representative fluorescent images of the hydrogels with (gel 2) or without NVP (gel 1,3) after 0 (left column), 80 (middle column), or 200 min (right column) in 250 U/mg collagenase IV. Scale bar = 300 µm. Quantification of (B) relative degradation quantified by normalized fluorescence over time, and (C) degradation rate determined by the slope of the linear portion of plot B. * indicates statistically significant difference ($p<0.05$). n=6 from 6 individual hydrogels. Values represent mean + standard deviation. *Figure adapted from [41] with permission from John Wiley and Sons.*

Chapter 3

HYDROGEL-INDUCED DORMANCY AND REACTIVATION IN BREAST CANCER

Sections in this chapter have been adapted from the following articles:

(1) Farino CJ, Pradhan S, Slater JH. The Influence of Matrix-Induced Dormancy on Metastatic Breast Cancer Chemoresistance. ACS Applied Biomaterials 2020, 3(9), 5832-5844.

(2) Farino Reyes CJ, Pradhan S, Slater JH. The Influence of Ligand Density and Degradability on Hydrogel Induced Breast Cancer Dormancy and Reactivation. Advanced Healthcare Materials 2021, 10(11), 2002227.

3.1 Introduction

Metastasis remains the leading cause of cancer-associated death.[1,2] During metastasis, disseminated tumor cells (DTCs) often adopt a dormant phenotype that provides a potential therapeutic "window of opportunity" lasting up to decades in which eliminating dormant DTCs or preventing their reactivation can be used to prevent metastatic recurrence. To form a better understanding of the mechanisms driving dormancy and reactivation and develop new therapeutics, *in vitro* platforms that provide the resolution required to perform mechanistic studies are urgently needed.

In the efforts to develop an *in vitro* platform that induces dormancy and reactivation, it is important to consider the relevant cell types that contain unique genetic signatures which may influence its phenotypic state. For instance, the concept

of organotropism initially described by Paget's seed and soil hypothesis proposes that cancer metastasis is dictated by a suitable host organ.[60-62] This concept is supported by results demonstrating that different cancer types metastasize to distinct secondary organs. For example, breast cancers preferentially metastasize to the bone, lung, and brain.[37] It is further hypothesized that specific cancer cells contain gene expression profiles that enable organ-specific seeding, survival, and proliferation known as organotropism.[63] Recent studies support this hypothesis, confirming that triple negative breast cancer cells that metastasize to the bone (BoM-1833)[38], lung (LM2-4175)[39], or brain (BrM2a-831)[40] contain unique genetic signatures that support their survival in each respective organ. Similarly, organotropism may play a unique role in tumor dormancy. The same genetic signatures that promote organ-specific survival may support the sustained survival of dormant micrometastases, allowing cells to survive in a quiescent state until microenvironmental conditions become suitable to support growth. In addition to consideration of organotropism, considering hormone status is also important in establishing a dormancy platform. For instance, studies indicate that ER^+ cancer have a significantly greater chance of entering dormancy than ER^- cancers.[64] Furthermore, dormancy in ER^+ tumors occur >5 years, in some cases >20 years, after treatment compared to ~2 years in ER^- cancers, providing a longer window of time to treat these patients.[65] Thus, with a greater chance of entering dormancy and longer periods of latency, ER^+ cancers are clinically relevant and provide a greater opportunity for effective treatment. Thus, in this work we included relevant organotropic sublines (BoM-1833, LM2-4175, and BrM2a-831) and a representative ER^+ breast cancer cell line, MCF7.

In chapter 2, we characterized hydrogels composed of 5% w/v enzymatically degradable PEG-PQ with controlled variations in ligand density (via RGDS) and degradability (via NVP), as described in chapter 2 to develop formulations mimicking three premetastatic niches: permissive gel 1 (++ adhesivity, ++ degradability: 2.1 mM RGDS, 0 mM NVP), non-permissive gel 2 (+ adhesivity, + degradability: 0.9 mM RGDS, 9.4 mM NVP), and non-permissive gel 3 (- adhesivity, ++ degradability: 0 mM RGDS, 0 mM NVP). In this chapter, we investigated if tuning matrix properties via ECM modulation can induce dormancy in organotropic sublines (BoM-1833, LM2-4175, and BrM2a-831) and an ER^+ breast cancer cell line, MCF7. The five cell lines were individually encapsulated and cultured in the three different hydrogel formulations for 15 days. Dormancy-associated metrics[7,43] including temporal measurements of cell viability, metabolic activity, proliferation, apoptosis, morphology, and phosphorylated (extracellular signal-regulated kinase 1/2) ERK and p38 were quantified.[41] Using these metrics, a classification scheme was created based on logic and well-established dormancy metrics to determine hydrogel-induced phenotypic states. Using this approach, the cells were classified as residing in either (1) growth, (2) restricted survival cellular dormancy, (3) balanced cellular dormancy, or (4) balanced tumor mass dormancy. Results were also compared between parental 231s, organotropic sublines, and MCF7s to identify differences in induced behavior across the different cell lines. Cells undergoing growth were characterized by increased viable cell density, proliferation, and metabolic activity. In restricted survival dormancy, there was significant cell death accompanied by single surviving cells that did not proliferate or undergo apoptosis throughout the 15-day culture period. Cells in balanced dormancy remained in a delicate balance between

proliferation and death with no significant differences in viable cell density, proliferating cell density, or metabolic activity. Cells undergoing balanced dormancy were further characterized as balanced tumor mass dormancy or balanced cellular dormancy depending on whether they formed clusters or remained single cells.

In the RGDS rich and highly degradable hydrogel formulation (permissive gel 1), all five cell lines adopted a growth state. Conversely, when cultured in a hydrogel formulation void of RGDS but with high degradability (non-permissive gel 3) the parental 231 and MCF7 lines adopted a restricted survival, cellular dormancy state. The three organotropic sublines cultured in non-permissive gel 3 adopted a balanced cellular dormancy state. Interestingly, in gel 3, organotropic lines displayed significantly higher viability. All five cell lines entered a balanced dormancy state when cultured in a hydrogel formulation with decreased RGDS density and degradability (non-permissive gel 2). Parental and lung-tropic 231s cultured in non-permissive gel 2 were further classified as residing in balanced cellular dormancy while the bone- and brain-tropic sublines, and MCF7s adopted balanced tumor mass dormancy. Dynamic, "on-demand" photocoupling of PEG-RGDS into non-permissive gel 3 after 15 days in culture increased proliferation and viability in all five cell lines resulting in measured values comparable with the growth state induced by permissive gel 1, indicating the ability to reactivate dormant cells. These results demonstrate the ability to achieve growth, multiple dormancy states, and reactivation in genetically distinct organotropic, triple negative and ER^+ breast cancer lines, and highlights differences in induced behavior between 231 sublines, its parental line, and ER^+ cells. The ability of the hydrogel platform to induce cancer dormancy through facile changes in hydrogel properties can enable further mechanistic studies on microenvironmental

regulation of dormancy and metastatic relapse as well as potentially facilitate identification of new targets for development of therapeutics aimed at eliminating dormant cancer.

3.2 Methods

Methods used for PEG Macromer Synthesis and Characterization, Cell Encapsulation, and measuring PEG-RGDS incorporation, mesh size, compressive modulus, swelling ratio, and degradation rate were performed as described in Chapter 2.

3.2.1 Cell Culture

The metastatic, triple negative breast cancer line, MDA-MB-231 (parental 231), and ER^+ breast cancer line, MCF7 were purchased from American Type Culture Collection (ATCC). Organotropic sublines of the parental 231s that preferentially metastasize to bone (BoM-1833)[38], lung (LM2-4175)[39], or brain (BrM2a-831)[40] were acquired from the Massague Lab at Memorial Sloan Kettering via a non-licensing, academic research agreement. All cell lines were cultured in fibronectin coated (10 μg/mL) T75 flasks with Dulbecco's Modified Eagle Medium (DMEM: Lonza C#12-741F) supplemented with 10% (v/v) fetal bovine serum (FBS: Thermo Fisher C#16000044) and 1% (v/v) penicillin-streptomycin (Lonza C#DE17-602E) to 80% confluence at 37 °C and 5% CO_2. Prior to encapsulation in hydrogels, cells were serum starved in serum-free DMEM for 48 h to synchronize the cell cycle.

The organotropic cell lines were selected via multiple rounds of *in vivo* inoculation, expansion in culture, and re-inoculation.[38-40] When conducting RNA expression analysis of MDA-MB-231 sublines, including bone-tropic, BoM-1833s,

the cells were cultured for two weeks in a 96-well plate before analysis which indicated differences in genetic expression.[38] In an attempt to maintain original organotypic properties, organotropic sublines were cultured for no longer than two weeks in standard culture and maintained at low passage numbers prior to hydrogel encapsulation. The data demonstrating significantly different responses between the 231 parental line and the organotropic sublines, and within the organotropic sublines, indicates that differential gene expression was likely maintained[66-68] but future studies to confirm that the original gene expression differences still exist should be conducted. The following passage numbers were used for each cell line: parental 231s (p 35-40), BoM-1833 (p 26-28), LM2-4175 (p 24-26), BrM2a-831 (p 41-43), MCF7s (p 7-10).

3.2.2 Quantification of Viability

At days 0 (6 h post encapsulation) and 15, cell-laden hydrogels were rinsed with PBS for 15 min and labeled with a Live/Dead® cell viability kit (ThermoFisher C#L3224) according to the manufacturer's instructions. The hydrogels were rinsed with PBS and placed between coverslips as previously described.[36] Fluorescent z-stacks (z-height: 150 μm) were acquired using structured illumination on a Zeiss AxioObserver Z1 inverted fluorescent microscope equipped with a Zeiss Apotome2 imaging system and a Hamamatsu ORCA-Flash 4.0LT camera as previously described.[36] To obtain representative images, z-stacks were captured at the approximate center of each hydrogel, between its top and bottom surfaces. We did not encounter limitations in oxygen transport as the hydrogel height (500 μm) was too low to form oxygen/transport gradients.[36] Using FIJI software (NIH), the number of live and dead cells were counted to quantify cell viability. A minimum of 5 z-stacks from 5

individual hydrogels were imaged and quantified at each time point for each hydrogel formulation for the five cell lines.

3.2.3 Quantification of Early Apoptosis

At days 0 (6 h post encapsulation) and 15, cell-laden hydrogels were rinsed with a binding buffer (HEPES-buffered saline (HBS) with 2.5 mM $CaCl_2$) for 15 min. The hydrogels were incubated at 37 °C for 30 min with a solution containing CF568 Annexin V (Biotium, 1 µg/mL C#29010), an early apoptosis marker. A nuclear stain, Hoechst 33342 (10 µg/mL), was used for counterstaining. The hydrogels were rinsed with binding buffer and imaged using structured illumination as described in section 3.2.2. FIJI software was used to quantify the percentage of cells positive for Annexin V. A minimum of 5 z-stacks from 5 individual hydrogels were imaged and quantified at each time point for each hydrogel formulation for the five cell lines.

3.2.4 Quantification of Proliferation

To measure cell proliferation, 5-ethynyl-2-deoxyuridine (EdU) incorporation via Click-It® EdU Imaging Kit (ThermoFisher C#C10340) was used according to the manufacturer's instructions at days 0 (6 h post encapsulation) and 15. Hydrogels were incubated with 10 µM EdU in medium for 24 h. Cell-laden hydrogels were rinsed with PBS and fixed with 4% paraformaldehyde (room temperature, 30 min). After fixation, cells were permeabilized in PBS-T (PBS + 0.2% (w/v) bovine serum albumin (BSA) +0.1% (v/v) Triton-X) for 15 min and blocked with blocking buffer (PBS + 3% (v/v) FBS) for 30 min. Proliferating nuclei were labeled with Alexa Fluor 647-azide and counter-stained with Hoechst 33342 (nuclei). Imaging and analysis were performed as described in section 3.2.2 to quantify the percentage of Alexa Flour 647 positive

nuclei. A minimum of 5 z-stacks from 5 individual hydrogels were imaged and quantified at each time point for each hydrogel formulation for the five cell lines.

3.2.5 Quantification of Metabolic Activity

Cell-laden hydrogels were cultured in phenol red-free media. On days 0 (6 h post encapsulation) and 15, metabolic activity was measured using an Alamar Blue assay (Thermo Fisher C#A50100). Hydrogels were rinsed with PBS and incubated at 37 °C in a working solution of Alamar Blue (10 µL of 10X stock + 100 µL phenol red-free media) for 4 h, allowing resazurin in the working solution to be converted to resorufin. Hydrogels were transferred into fresh well plates in phenol red-free media and the fluorescence intensities were measured with a plate reader (Biotek Synergy, Excitation: 550 nm, Emission: 600 nm) to quantify relative metabolic activity. Wells with media, but no hydrogel, served as background controls. Measured values were normalized to day 0 values. A minimum of 6 individual hydrogels were quantified at each time point for each hydrogel formulation for the five cell lines.

3.2.6 Quantification of Cell and Cell Cluster Properties

After 15 days in culture, cell-laden hydrogels were rinsed with PBS, fixed with 4% paraformaldehyde for 30 min, permeabilized with PBS-T for 20 min, and blocked with BSA blocking buffer (2% (w/v)) for 30 min. F-actin was fluorescently labeled with Alexa Fluor 568 Phalloidin (ThermoFisher C#A12380) (2.6 µg/mL) for 1 h and counterstained with Hoechst 33342 (10 µg/mL) for 30 min. After rinsing with PBS, hydrogels were imaged using structured illumination as described in section 3.2.2. Individual cells and cell clusters were traced using FIJI to quantify the percentage of the cell population residing as single cells or in cell clusters, round or protruding

single cells, and round or protruding cell clusters. Clusters were defined as greater than 2 nuclei clustered together. Feret diameter, aspect ratio, circularity, roundness, cluster density, and single cell density were also quantified. Solitary cells and cell clusters with a roundness value less than 0.80 were categorized as protruding.[34-36]

3.2.7 Quantification of p-ERK and p-p38 Expression

A phospho-p38 (p-p38) mitogen activated kinase (MAPK) (Th180/Tyr182) mouse antibody (C#9216S) and a phospho-p44/42 MAPK (p-ERK) (ERK1/2)(Th202/Tyr204) rabbit antibody was purchased from Cell Signaling (C#4370S). After 15 days in culture, cell-laden hydrogels were fixed using 4% paraformaldehyde for 30 min and blocked with blocking buffer (5% (w/v) BSA, 0.3% (v/v) Triton X-100 in PBS) for 30 min at room temperature. Hydrogels were incubated overnight with the p-p38 primary antibody (1:200 in dilution buffer (1% (w/v) BSA, 0.3% (v/v) Triton X-100 in PBS) at 4°C, rinsed with PBS three times, and incubated with a secondary antibody (goat anti-mouse IgG-Alexa Fluor 647: 1:500 in dilution buffer) for 2 h at room temperature in the dark. Labeled hydrogels were rinsed and incubated with the p-ERK antibody (1:200 in dilution buffer) overnight at 4°C, rinsed with PBS, and incubated with a secondary antibody (goat-anti rabbit IgG-Alexa Fluor 488: 1:500), and Hoechst 33342 (10 μg/mL) in dilution buffer. Labeled hydrogels were stored in PBS and imaged as described in section 3.2.2. FIJI software was used to quantify the mean fluorescence intensity of each z-stack to quantify p-p38, p-ERK, and the p-ERK to p-p38 ratio. For each image stack, the mean fluorescence intensity of a maximum intensity z-projection was measured for p-p38 and for p-ERK using FIJI software. To account for background noise, intensity measurements of five background regions (regions in each corner and near the center of the image), that did

not contain cells, were quantified and averaged for each image. Background measurements were subtracted and normalized intensity values from 5 individual z-stacks were averaged to obtain the p-ERK and p-p38 intensity values. A minimum of 5 z-stacks from 5 individual hydrogels were imaged and quantified for each hydrogel formulation for the five cell lines.

3.2.8 Reactivation of Dormant Cells

The 231 parental line, three organotropic sublines, and MCF7s were individually encapsulated in non-permissive gel 3 (5% w/v PEG-PQ, 0 mM PEG-RGDS, 0 mM NVP) and cultured for 15 days. On day 15, the cell-laden hydrogels were rinsed with PBS for 10 min and incubated in a solution containing 10 mM PEG-RGDS and 10 mM LAP for 1 h at 37°C as previously described.[35,36] After the solution was allowed to diffuse into the hydrogel for 1 h, the PEG-RGDS was photocoupled to the hydrogel via exposure to broad spectrum UV for 1 min. The hydrogels were rinsed with PBS for 10 min to wash away any unbound PEG-RGDS. The cell-laden hydrogels were cultured for an additional 7 days post RGDS coupling, (22 days total). At day 22, cell viability and proliferation were measured and quantified as described in section 3.2.2. A minimum of 6 z-stacks from 6 individual hydrogels were imaged and quantified for the five cell lines.

3.2.9 Statistical Analysis

Statistical analysis was performed using Minitab 17 Statistical Software (Minitab Inc.). A sample size of 5 3D stacks from 5 individual hydrogels for each formulation was used for quantification of viability, early apoptosis, proliferation, metabolic activity, morphological analysis, and p38/pERK expression. Data in all

figures represent the mean + plus one standard deviation. Raw data (without exclusion of outliers) was averaged or normalized to day 0 values as indicated in the text. Assumptions of normality and equality of variance among groups was evaluated using an Anderson-Darling test and a Levene's test respectively ($p>0.05$). For statistical comparison between values, one-way analysis of variance (ANOVA) (Tukey family error = 5%) was used implemented to determine statistical significance between multiple groups, assuming equal sample size. ANOVA analysis was followed with a Howell post-hoc test in cases of unequal variance. A 2-sample t-test was used for statistical comparison between two variables. Unless otherwise indicated, $p < 0.05$ was considered statistically significant.

3.3 Results

3.3.1 Overview of Hydrogel Properties

Hydrogel properties were carefully characterized in chapter 2. In summary, formulations without NVP (permissive gel 1, non-permissive gel 3) had a compressive modulus of 4.2 ± 0.6 kPa (cellular, day 15), a mesh size of 69 ± 5 nm, degradation rate of (0.0125 ± 0.0006 min^{-1}), and a swelling ratio of 17 ± 9 (Figure 2.1). NVP incorporation in non-permissive gel 2 increased the number of crosslinks, leading to an increased compressive modulus (7.6 ± 0.8 kPa) and decreased mesh size (55 ± 4 nm), degradation rate (0.0081 ± 0.0016 min^{-1}), and swelling ratio (13 ± 6) (Figure 2.1). To quantify the effect of tuning hydrogel composition on alterations in cell phenotype, we used the highly metastatic, triple negative breast cancer cell line MDA-MB-231 (231) (parental 231), three organotropic sublines derived from the 231 parental line that preferentially metastasize to bone (BoM-1833), lung (LM2-4175), or

brain (BrM2a-831), and ER^+ breast cancer cell line, MCF7.[38-40] Each cell line was independently encapsulated in the three hydrogel formulations and after 15 days in culture the induced cell phenotype was classified using a multimetric analysis of several dormancy-associated metrics (Figure 2.1, 3.7).[7,43] These metrics included temporal changes in cell viability, cell density, metabolic activity, proliferation, apoptosis, expression of phosphorylated p38 and ERK, and existence as solitary cells or in cell clusters (Figure 2.1). The classified phenotypic states included: 1) growth, 2) balanced cellular dormancy, 3) balanced tumor mass dormancy, and 4) restricted survival cellular dormancy.

3.3.2 Hydrogel-Induced Changes in Viability

It has been established that hydrogel properties influence cancer cell phenotype.[7,35,44,69] In a previous study, hydrogel formulations that induced growth and distinct dormant states were identified via quantification of cellular responses using the parental 231 line.[35] Here we chose three of those sixteen formulations to quantify the responses of the organotropic sublines and MCF7 cells. We encapsulated parental 231 line, BoM-1833 (bone-tropic), LM-4175 (lung-tropic), BrM2a-831 (brain-tropic), or MCF7s in formulations that induced growth (permissive gel 1:10 mM PEG-RGDS, 0 mM NVP), balanced dormancy (non-permissive gel 2: 1 mM PEG-RGDS, 9.7 μM NVP), or cellular dormancy (non-permissive gel 3: 0 PEG-RGDS, 0 NVP) in the parental 231s to determine if the organotropic sublines and MCF7s had a similar or different response.[41] Cells were cultured for 15 days in each formulation to provide enough time to respond to the hydrogel properties, while longer culture periods did not significantly alter phenotype.[34-36] At days 0 (6 h post encapsulation) and 15, we quantified viability (Figure 3.1). Viability at day 0 was >81.9% in all cases, indicating

low cytotoxicity during photopolymerization (Figure 3.1). Through day 15, viability remained high (>82.9%) for all cell lines cultured in permissive gel 1, with significantly higher viability in the lung- and brain-tropic sublines (Figure 3.1B). Viability also remained high in non-permissive gel 2 with the parental line being 91.5 ± 0.7% viable, bone-tropic 83.5 ± 1.5% viable, lung-tropic 96.9 ± 1.7% viable, brain-tropic 83.3 ± 3.6% viable, and MCF7s 80.3 ± 3.0% (Figure 3.1B). In the absence of RGDS (non-permissive gel 3), the viability of the parental 231 line (45.4 ± 3.2%) and MCF7 line (42.5 ± 2.5%) decreased significantly, while all the organotropic sublines remained >88.5% viable (Figure 3.1B).

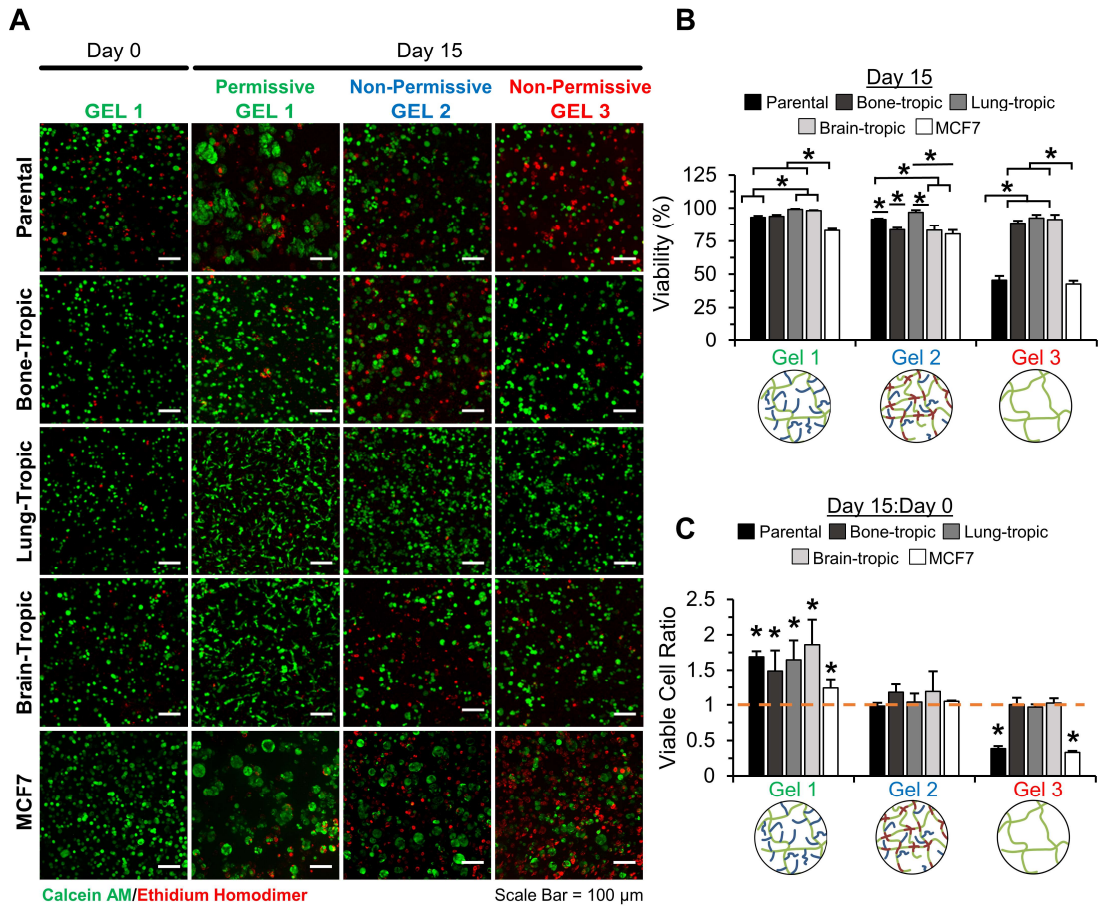

Figure 3.1: Hydrogel-Induced Changes in Viability. (A) Representative maximum intensity z-projections from 3D image stacks of MDA-MB-231s (parental), BoM-1833s (bone-tropic), LM2-4175s (lung-tropic), BrM2a-831s (brain-tropic), and MCF7s on day 0 (Gel 1, 6 h post encapsulation) or day 15 within each hydrogel formulation. Cells were labeled with Calcein AM (green: live cells) and ethidium homodimer (red: dead cells). Scale bar = 100 µm. Quantification of (B) cell viability on day 15 and (C) viable cell ratio (the number of viable cells at day 15 normalized to day 0). Dashed line indicates a ratio of 1.0 (no change in the number of viable cells). * indicates $p<0.05$ compared to 1.0. n=5 z-stacks from 5 individual hydrogels. Values represent mean + standard deviation. *Figure adapted from [41] with permission from John Wiley and Sons.*

To quantify the temporal change in viable cells throughout the 15-day culture period, we measured the number of viable cells at day 15 and normalized it to the number of viable cells at day 0 to determine the viable cell ratio, which indicates if the viable cell population is increasing, remaining constant, or decreasing over time (Figure 3.1C). In permissive gel 1, there was a 1.2 to 1.9-fold increase in the number of viable cells for all five cell lines, indicating that the hydrogel properties of permissive gel 1 promoted proliferation and survival (Figure 3.1C). In non-permissive gel 2, there were no statistically significant differences in the number of viable cells present between days 0 and 15 (viable cell ratio ~1.0) in all cell lines tested indicating a constant viable cell density over the 15-day culture period (Figure 3.1C). Consistent to viability results in non-permissive gel 3, the parental 231 and MCF7 line displayed a viable cell ratio significantly lower than 1 indicating a decrease in the viable cell density with time, while the organotropic sublines displayed a viable cell ratio ~1.0 (Figure 3.1C) indicating no statistically significant change in the viable cell density with time.

These results indicate that reduced matrix degradability (non-permissive gel 2) and cell adhesion (non-permissive gels 2 and 3) both induced an arrested growth state in the organotropic sublines as indicated by no statistically significant change in the number of viable cells over 15 days in culture (viable cell ratio ~1.0). This temporally stable viable cell ratio indicates that the cell density is staying constant over time; a characteristic that aligns with balanced dormancy. The results also highlight a unique ability for organotropic cells to survive under unfavorable conditions (non-permissive gel 3) which induced a significant decrease in cell survival in the parental 231 and MCF7 lines but not the organotropic sublines (Figure 3.1B, C), potentially due to

unique genetic signatures expressed by the organotropic lines that promote survival.[38-40]

3.3.3 Hydrogel-Induced Changes in Early Apoptosis

We quantified early apoptosis to determine the mode of cell death that was occurring. Annexin V, an early apoptosis marker, was used to label and identify cells undergoing apoptotic death at day 15 (Figure 3.2). In permissive gel 1, Annexin V^+ cells remained low with less than 10.1% of the cells undergoing early apoptosis at day 15 (Figure 3.2B). In non-permissive gel 2, Annexin V^+ cells composed 21.6 ± 3.3% of the parental line, 14.3 ± 1.7% of the bone-tropic, 11.4 ± 2.0% of the lung-tropic, 11.3 ± 2.9% of the brain-tropic sublines, and of 16.5 ± 2.3% MCF7s (Figure 3.2B). Consistent with viability results, non-permissive gel 3 induced increased apoptosis in the parental 231s and MCF7s compared to non-permissive gels 2 and 3. In non-permissive gel 3, apoptosis levels increased to 43.6 ± 4.6% in parental 231s and 43.0 ± 4.2% in MCF7s, while the three organotropic sublines remained <11.9% (Figure 3.2B). These results further indicate that the parental 231s and MCF7s are more susceptible to apoptosis under unfavorable microenvironmental conditions, in this case, lack of integrin ligation via RGDS in non-permissive gel 3, compared to the organotropic sublines.

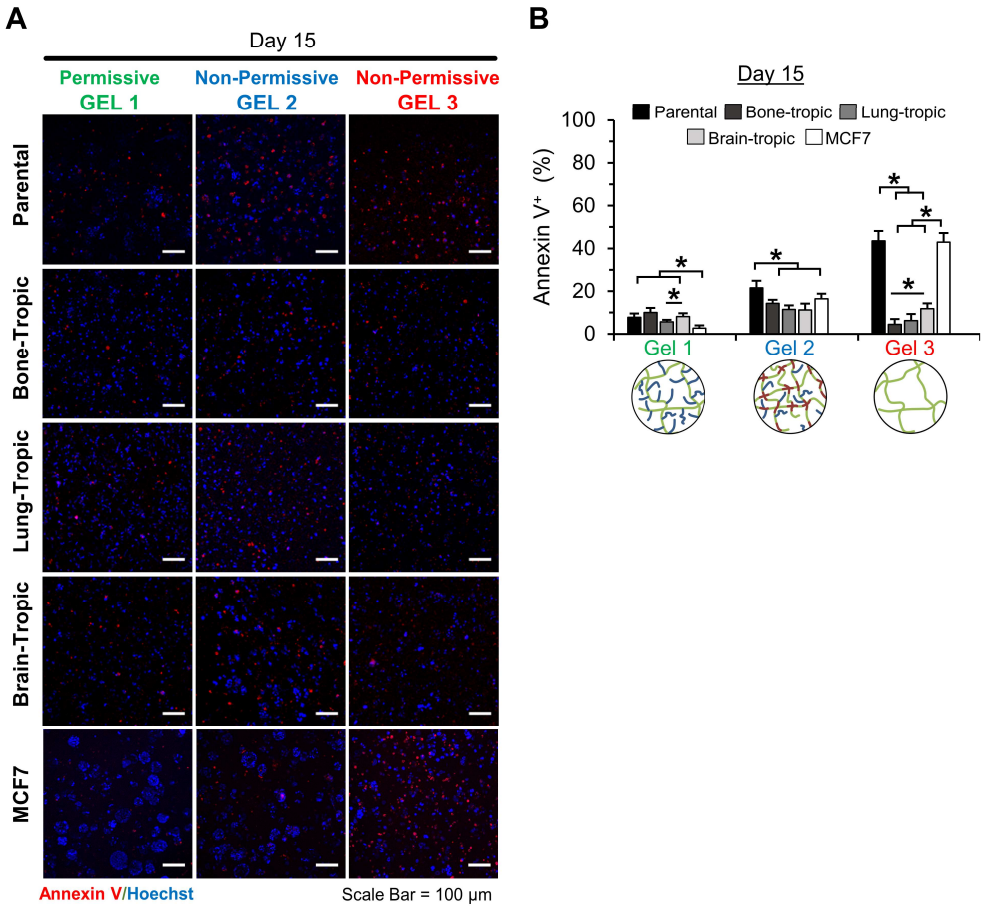

Figure 3.2: Hydrogel-Induced Changes in Early Apoptosis. (A) Representative maximum intensity z-projections from 3D image stacks of MDA-MB-231s (parental), BoM-1833s (bone-tropic), LM2-4175s (lung-tropic), BrM2a-831s (brain-tropic), and MCF7s on day 15 within each hydrogel formulation. Cells were labeled with the early apoptosis marker Annexin V (red: apoptotic cells) and Hoechst (blue: nuclei). Scale bar = 100 μm. (B) Quantification of Annexin V^+ cells on day 15. * indicates $p<0.05$. n=5 z-stacks from 5 individual hydrogels. Values represent mean + standard deviation. *Figure adapted from [41] with permission from John Wiley and Sons.*

To assess if apoptosis was the primary mode of cell death, we compared the percent of the cell population ethidium homodimer$^+$ (dead) to the percent Annexin V^+

(apoptotic) (Figure 3.3). A Pearson Correlation test demonstrated a strong correlation (R = 0.8911) indicating that apoptosis accounted for the majority of the cell death observed.

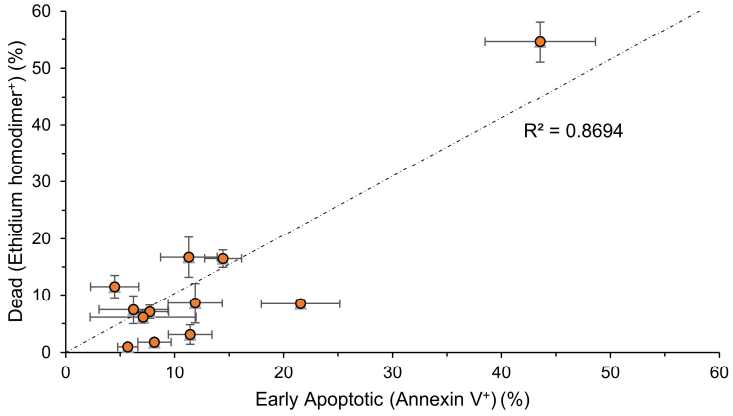

Figure 3.3: Mode of Cell Death. Quantification of the percent dead cells (via ethidium homodimer labeling) and percent Annexin V^+ cells, indicative of early apoptosis for the parental and organotropic sublines across gels 1, 2, and 3. A Pearson Correlation test indicates a strong correlation (R = 0.8911), indicating that apoptosis accounts for most of the cell death that occurs. Dashed line indicated a 1:1 ratio between % dead and % Annexin V^+ cells. n=5 z-stacks from 5 individual hydrogels for each condition. Values represent mean ± standard deviation. *Figure obtained from [41] with permission from John Wiley and Sons.*

3.3.4 Hydrogel-Induced Changes in Proliferation

Dormant cells survive in a G_0-G_1 phase, only returning to active proliferation under favorable conditions (angiogenesis, reduced microenvironmental stress, etc.).[7,53] Thus, quantifying the role of hydrogel properties on proliferation aids in understanding whether cells were in a growth or dormant state. To assess proliferation, we measured EdU incorporation into newly synthesized DNA of dividing cells. Cells

stained positive for EdU incorporation (EdU^+) were considered proliferative (Figure 3.4).

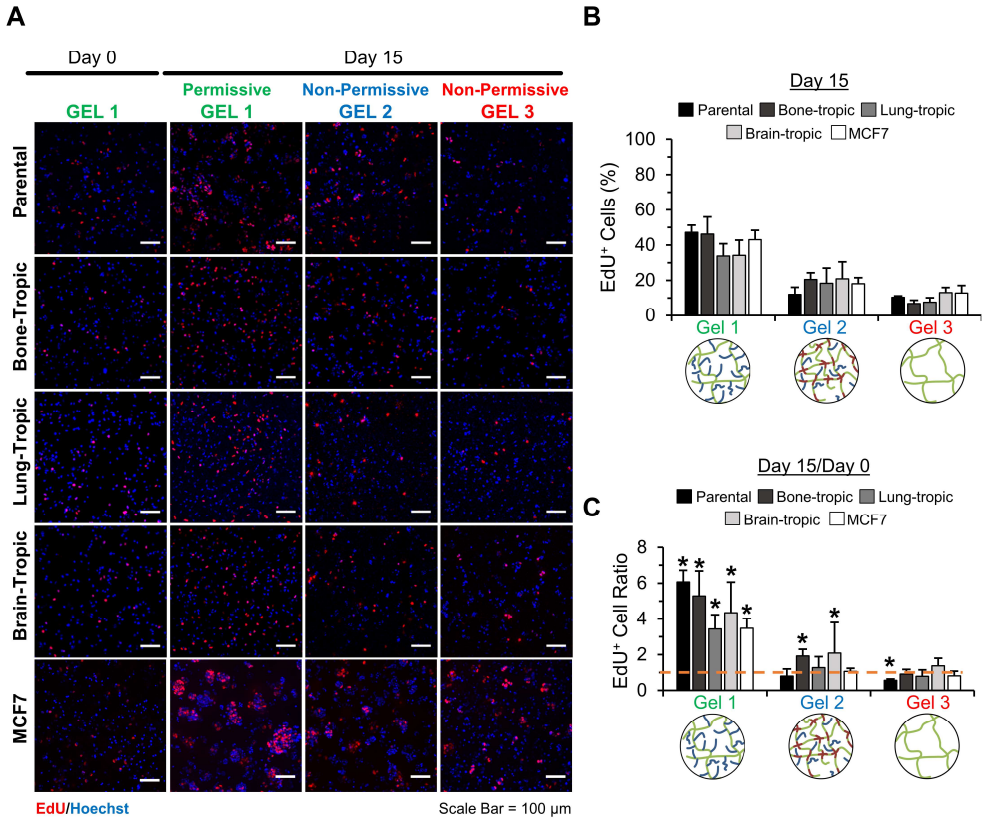

Figure 3.4: Hydrogel Induced Changes in Proliferation. (A) Representative maximum intensity z-projections from 3D image stacks of MDA-MB-231s (parental), BoM-1833s (bone-tropic), LM2-4175s (lung-tropic), BrM2a-831s (brain-tropic), and MCF7s on day 0 (Gel 1, 6 h post encapsulation) or day 15 within each hydrogel formulation. Cells were labeled with EdU (red: proliferative cells) and Hoechst (blue: nuclei). Scale bar = 100 µm. (B) Quantification of the percentage of EdU^+ cells on day 15. (C) Quantification of the EdU^+ cell ratio (the number of EdU^+ cells on day 15 normalized to day 0). Dashed line indicates a ratio of 1.0 (no change in the number of actively proliferating cells). * indicates $p<0.05$ compared to 1.0. n=5 z-stacks from 5 individual hydrogels. Values represent mean + standard deviation. *Figure adapted from [41] with permission from John Wiley and Sons.*

Day 0 values after 48 h serum starvation and 6 h culture in hydrogels ranged between 5.9 to 17.1% EdU^+ for all gel conditions. In permissive gel 1, proliferation at day 0 was 11.2 ± 2.1% for parental 231s, 10.4 ± 2.1% for bone-tropic, 10.8 ± 2.0% for lung-tropic, 10.8 ± 1.7% for brain-tropic sublines, and 16.6 ± 4.2% for MCF7s. In non-permissive gel 2, proliferation at day 0 was 13.2 ± 2.1% for parental 231s, 11.2 ± 2.3% for bone-tropic, 7.6 ± 1.1% for lung-tropic, 5.9 ± 3.2% for brain-tropic sublines, and 17.1 ± 3.8% for MCF7s. In non-permissive gel 3, proliferation at day 0 was 12.2 ± 1.6% for parental 231s, 11.0 ± 2.8% for bone-tropic, 7.9 ± 0.8% for lung-tropic, 14.0 ± 4.1% for brain-tropic sublines, and 14.8 ± 2.0% for MCF7s. The PEG-RGDS rich and highly degradable matrix (permissive gel 1) promoted proliferation across all cell lines through day 15 (EdU^+ cells >33.8%) (Figure 3.4). Consistent across all five cell lines, proliferation decreased in non-permissive gel 2 (parental: 11.9 ± 4.1%; bone: 20.5 ± 3.8%; lung: 18.4 ± 8.6%; brain: 20.9 ± 9.6%; MCF7s: 18.1 ± 3.5%) (Figure 3.4B). In the absence of PEG-RGDS (non-permissive gel 3) a further decrease in proliferation in all cell lines was observed (parental: 10.3 ± 0.8%; bone: 6.8 ± 1.9%; lung: 7.5 ± 2.6%; brain: 13.0 ± 2.9%; MCF7s: 12.8 ± 4.3%) (Figure 3.4B) which were similar values to those measured after 48 h serum starvation (5.9-17.1%).

We also analyzed temporal changes in proliferation induced by the hydrogels by comparing the number of EdU^+ cells at day 0 to day 15 (EdU^+ cell ratio) (Figure 3.4C). All cell lines in permissive gel 1 showed a statistically significant increase in the number of proliferating cells (EdU^+ ratio >1), with 3.5 to 6.1 times as many proliferating cells at day 15 compared to day 0 (Figure 3.4C). In contrast, with NVP incorporation (non-permissive gel 2), there were only significant increases in proliferation in the bone- and brain-tropic sublines, which both had twice as many

proliferating cells at day 15 compared to day 0 (Figure 3.4C). When PEG-RGDS was absent (non-permissive gel 3), only the parental line showed significantly fewer EdU^+ cells at day 15, while the number of proliferating cells throughout the 15-day culture period remained constant, at a low value (<13%), for the organotropic sublines and MCF7s cultured in non-permissive gel 3 (Figure 3.4C).

This data demonstrates that a RGDS rich and highly degradable hydrogel (permissive gel 1) promotes proliferation in all cell lines tested, while proliferation is reduced when cultured in a hydrogel formulation with decreased RGDS and decreased degradability (non-permissive gel 2), which is even further reduced when no RGDS is available for ligation (non-permissive gel 3). Along with viability data, these results indicate that most of the organotropic sublines cultured in non-permissive gels 2 and 3 remain viable but not actively proliferating (with the exception of the bone- and brain-tropic sublines in non-permissive gel 2), indicative of a quiescent or dormant state.

3.3.5 Ratiometric Analysis of Cell Viability, Death, and Metabolic Activity

To quantitatively assess if hydrogels induced a balanced survival state, we quantified the ratio of new live cells formed to new dead cells formed post-encapsulation in the hydrogels over the 15-day culture period. We counted the number of live cells and dead cells present at day 15, subtracted the number of live and dead cells present at day 0, and divided the number of new live by the number of new dead cells to obtain the new live to new dead cell ratio (Figure 3.5). This metric provides a snapshot of how the cell population density changed with time with regard to proliferation and death. As expected, all five cell lines cultured in permissive gel 1 showed significantly more new live cells at day 15 (new live: new dead cell ratio >1.0) (Figure 3.5A) further indicating an increase in the cell population over time. In non-

permissive gel 3, the parental 231 and MCF7 lines had no new live cells at day 15, further indicating growth arrest and death. All five cell lines cultured in non-permissive gel 2 and the three organotropic sublines cultured in non-permissive gel 3 displayed a new live to new dead cell ratio of ~1.0 indicating no significant change in the total number of cells from day 0 to 15 (Figure 3.5A). These results indicate that cells cultured in non-permissive gels 2 and 3 attained a near perfect balance in cell survival and death with the exception of the parental 231 and MCF7 line in non-permissive gel 3.

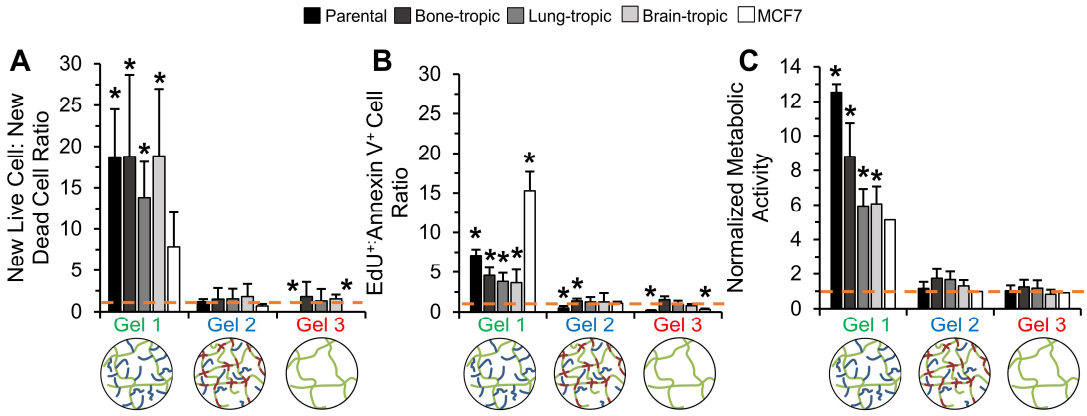

Figure 3.5: Ratiometric Analysis of Cell Viability, Death, & Metabolic Activity. (A) Ratio of new live to new dead cells formed in the hydrogels post day 0 as observed on day 15. Dashed line represents a ratio of 1.0 (indicating a perfect balance between the number of new live and dead cells formed in the gels post day 0). (B) Ratio of EdU^+ cells to Annexin V^+ cells at day 15. Dashed line indicates a ratio of 1.0 (indicating a perfect balance between proliferation and apoptosis). (C) Quantification of relative metabolic activity on day 15, normalized to day 0. Dashed line indicates a ratio of 1.0 (no change in metabolic activity post day 0). * indicates $p<0.05$ compared to 1.0. n=5 z-stacks from 5 individual hydrogels. Values represent mean + standard deviation. *Figure adapted from [41] with permission from John Wiley and Sons.*

To determine if a balance between proliferation and apoptosis existed, the ratio of EdU^+ cells to Annexin V^+ cells at day 15 (EdU^+:Annexin V^+ ratio) (Figure 3.5B) was quantified. In permissive gel 1, all cell lines showed significantly more EdU^+ cells than Annexin V^+ cells (EdU^+:Annexin V^+ ratio >1.0), confirming that more cells were proliferating than undergoing early apoptosis at day 15 (Figure 3.5B). In non-permissive gel 2, the lung- and brain-tropic sublines showed no significant difference between proliferating and apoptotic cells (EdU^+:Annexin V^+ ratio ~1.0) indicating a near perfect balance between the two (Figure 3.5B). However, the parental 231 and MCF7 lines had significantly more Annexin V^+ cells than EdU^+ cells at day 15 (EdU^+:Annexin V^+ ratio <1.0) indicating predominance of apoptosis over proliferation, while the bone-tropic line had more EdU^+ cells (EdU^+:Annexin V^+ ratio > 1.0) (Figure 3.5B). In non-permissive gel 3, the parental 231s and MCF7s behaved similar as in non-permissive gel 2 while all three organotropic sublines maintained a balance between proliferation and apoptosis (EdU^+:Annexin V^+ ratio ~1.0).

Metabolic activity is another dormancy-associated metric, since dormant populations have been shown to display reduced metabolic activity.[3,43] Thus, we compared metabolic activity at days 0 (6 h post encapsulation) and 15 in culture using an Alamar Blue assay. Parental 231s had the largest increase (12.5 ± 0.5-fold) in metabolic activity, while bone-, lung-, brain-tropic, and MCF7s displayed an 8.8±1.9, 5.9±1.0, 6.1±1.0, and 5.3±1.9-fold increase respectively when cultured in permissive gel 1 (Figure 3.5C). In non-permissive gel 2, metabolic activity remained constant over the 15-day period in all five cell lines (Figure 3.5C). Similarly, no metabolic changes were observed in non-permissive gel 3 (Figure 3.5C). These results highlight the importance of matrix degradability and integrin ligation in regulating metabolic

activity in parental 231, organotropic 231 sublines, and MCF7s and indicate that tuning these properties can induce a low metabolic state in the five cell lines implemented in this study with a value not significantly different compared to after 48 h serum starvation.

3.3.6 Hydrogel-Induced Changes in Cell and Cell Cluster Morphology

The morphology of individual, solitary cells and cell clusters was implemented to determine whether the hydrogel formulations induced a spread morphology with filopodial protrusions or not. In conditions that do not promote a spread phenotype, dormant cells are often characterized by either small, round clusters during tumor mass dormancy,[3,7,10] or by round single cells[3,7,9] during cellular dormancy. Thus, morphological analysis was conducted on the five cell lines in the three hydrogel formulations to investigate how the hydrogel properties influenced cell cluster formation and morphology. All cells were encapsulated, cultured for 15 days, fixed, fluorescently labeled for F-actin, and counterstained with Hoechst. After imaging, FIJI software was used to trace solitary cells and cell clusters and to quantify the single:clustered cell ratio, percent round cells, percent round clusters, cluster diameter, cluster density, and single cell density (Figure 3.6).

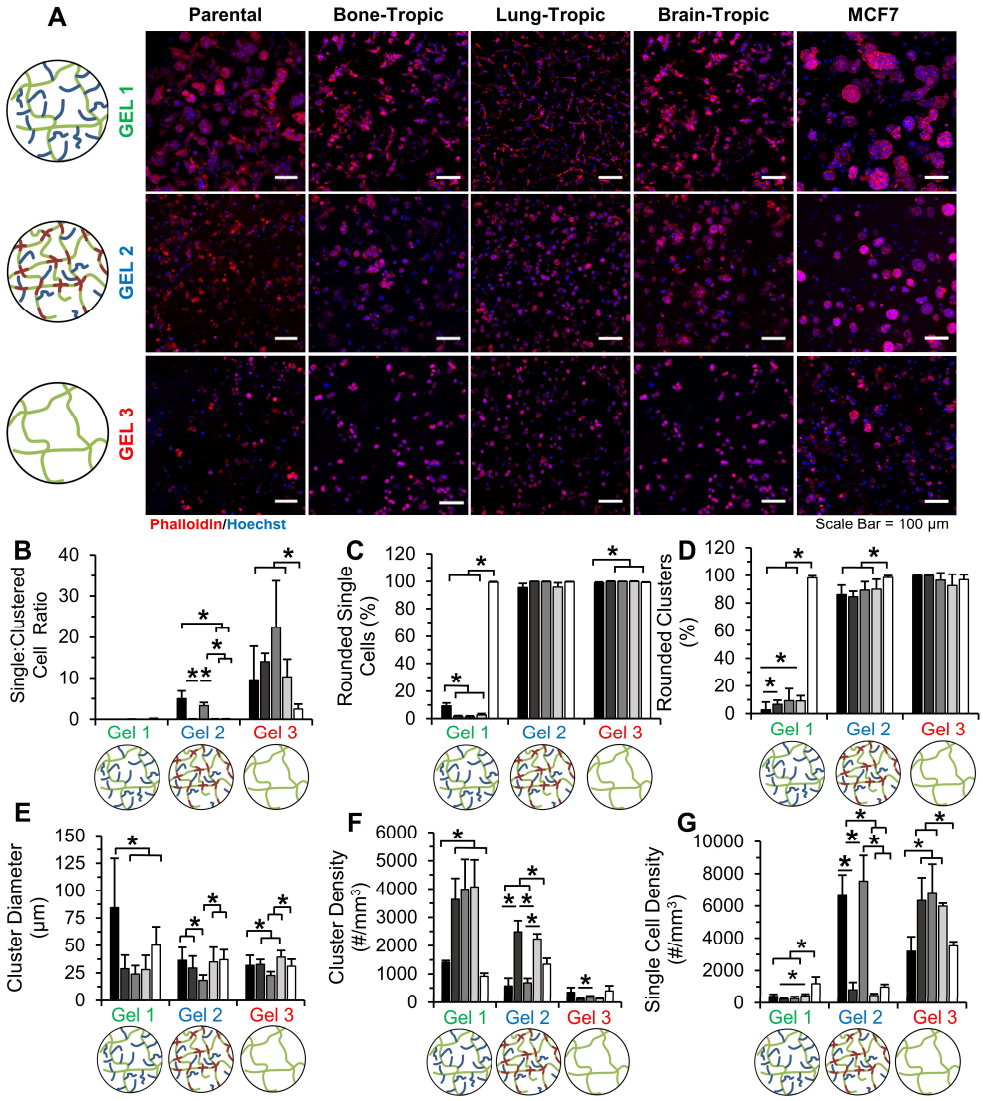

Figure 3.6: Morphological Analysis of Single Cells & Cell Clusters. (A) Representative maximum intensity z-projections from 3D image stacks of MDA-MB-231s (parental), BoM-1833s (bone-tropic), LM2-4175s (lung-tropic), BrM2a-831s (brain-tropic), and MCF7s after 15 days in culture. Cells were labeled with phalloidin (red: F-actin) and Hoechst (blue: nuclei). Scale bar = 100 µm. Quantification of (B) ratio of solitary cells to cells residing in clusters, (C) percentage of round single cells, (D) percentage of round cell clusters, (E) cluster diameter, (F) cluster density, and (G) single cell density within the hydrogels. * indicates statistically significant difference ($p<0.05$). n=5 z-stacks from 5 individual hydrogels. Values represent mean + standard deviation. *Figure adapted from [41] with permission from John Wiley and Sons.*

The percentage of cells that appeared in clusters or as single cells was quantified by measuring the single cell:clustered cell ratio. All five cell lines cultured in permissive gel 1 had a tendency to form cell clusters (single cell:clustered cell ratio <0.05), likely due to both high hydrogel degradability and RGDS density (Figure 3.6B). Addition of NVP to the hydrogel (non-permissive gel 2) also promoted cluster formation in the bone- and brain-tropic sublines and MCF7s. More than 91.9% (single cell:clustered cell ratio <0.1) of the cells in the bone- and brain-tropic sublines and MCF7s resided in cell clusters compared to less than 19.0% (single cell:clustered cell ratio >5.0) in the parental and lung-tropic lines (Figure 3.6B). In non-permissive gel 3, results were consistent across all cell lines, with greater than 86.1% of the cells residing as single cells (single cell:clustered cell ratio >10.3), confirming that integrin ligation played an important role in cluster formation (Figure 3.6B). The percentage of the cell population residing as either round or spread solitary cells or cell clusters was quantified using a roundness value cutoff of 0.80.[35,36] A majority of the cells for all 231 lines cultured in permissive gel 1 displayed spreading (<10% round), while most MCF7s (>99%) remained rounded (Figure 3.6C). In contrast, greater than 95% of the cells in non-permissive gels 2 and 3 displayed a round, non-spread morphology indicative of dormant cells for all five cell lines (Figure 3.6C).

While cells cultured in permissive gel 1 and non-permissive gel 2 formed clusters, there were distinct morphological differences. To quantify these differences, we measured cluster protrusion and diameter. The results demonstrate that all 231 cell clusters formed in permissive gel 1 adopted a protruding, spread phenotype, differing from the round clusters formed by MCF7s in permissive gel 1 or bone- and brain-tropic lines cultured in non-permissive gel 2 (Figure 3.6D). The majority of

clusters (>84.6%) in non-permissive gels 2 and 3 adopted a rounded morphology (Figure 3.6D). Regarding cluster size, that parental 231s formed ~3 times larger clusters (84.5 ± 45.0 μm diameter) in permissive gel 1 compared to the organotropic sublines (24.0-28.9 μm diameter) (Figure 3.6E). Similarly, MCF7s formed significantly larger clusters in permissive gel 1 of 50.4 ± 16.6 μm diameter. Significant differences in cluster size between cell lines were also observed in non-permissive gel 2, with clusters ranging from 18.1±5.0 μm (lung) to 37.2± 9.0 μm (MCF7s) in diameter (Figure 3.6E). Accounting for decreased cluster size, cluster density measurements show that organotropic sublines had ~3 times as many clusters per 1 mm^3 compared to the parental line (Figure 3.6F). Additionally, cluster density was significantly higher in bone- and brain-tropic sublines, and MCF7s in non-permissive gel 2, consistent with the single:clustered cell ratio measurements (Figure 3.6F). Accordingly, single cell density was higher in parental and lung-tropic cells in non-permissive gel 2, where most cells remained solitary (Figure 3.6G).

These results show distinct morphological differences induced by the three hydrogel formulations. While the four 231 cell lines in permissive gel 1 formed protruding clusters, indicative of aggressive tumor progression, parental 231s formed larger clusters, potentially suggesting a higher sensitivity to RGDS density and matrix degradation. In the case of MCF7s, clusters were round likely due to the origin of the MCF7 cell line which was originally derived from the pleural effusion of a 69-year-old woman and thus has retained many epithelial cell characteristics.[70] Interestingly, NVP incorporation led to different results among the cell lines in terms of cluster formation, diameter, and subsequent cluster and single cell densities. Bone and brain-tropic sublines, and MCF7s in non-permissive gel 2 formed round clusters, potentially

indicative of tumor mass dormancy. The parental 231s and the lung-tropic subline in non-permissive gel 2 remained as solitary, round individual cells indicative of cellular dormancy. The absence of RGDS (non-permissive gel 3) played a consistent role across the five cell lines tested and induced solitary, round cells suggesting induction of cellular dormancy.

3.3.7 Hydrogel-Induced Changes in Phosphorylated ERK (pERK) and p38 (p-38) Expression

The p-ERK:p-p38 activity ratio has been established as a determinant of whether cancer cells will enter a dormant state.[71-73] ERK activation promotes proliferation while p38 acts as an inhibitory regulator by inducing G_0-G_1 cell cycle arrest. Extensive work by Aguirre-Ghiso and colleagues has shown that decreased p-ERK and increased p-p38 expression can shift cells from a state of tumorgenicity to dormancy *in vivo*.[71,72] This mechanism has been further supported by confirmation that overexpression of genes that suppress ERK activation occur during dormancy.[64,74-76] To determine if the parental and organotropic sublines expressed differences in the p-ERK:p-p38 ratio as a function of hydrogel formulation, cells were cultured in the hydrogels for 15 days, fixed, fluorescently labeled for phosphorylated ERK1/2 and p38 and the nucleus counterstained with Hoechst (Figure 3.7-3.9).

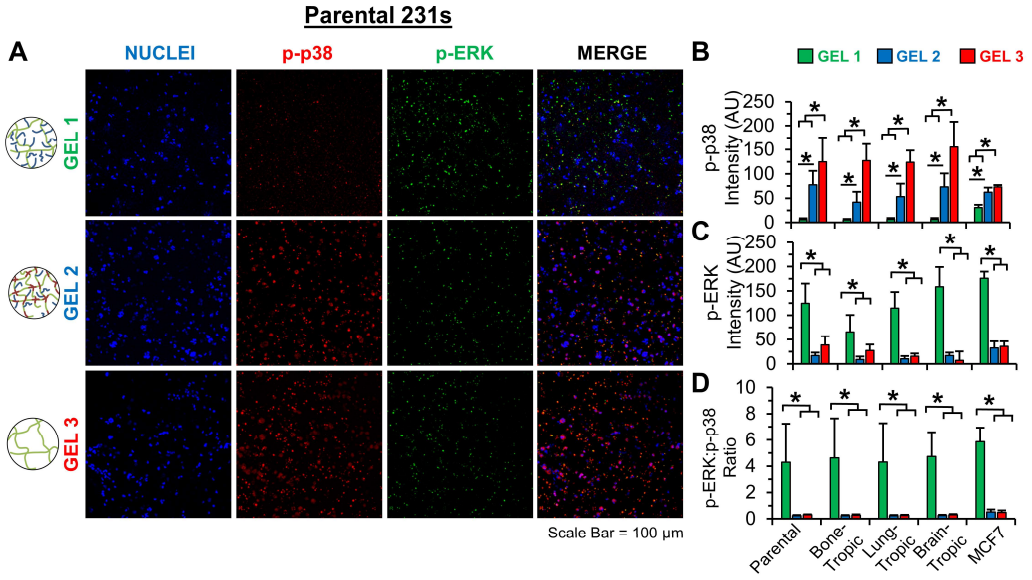

Figure 3.7: Hydrogel-Induced Changes in Phosphorylated p38 & ERK Expression. (A) Representative maximum intensity z-projections from 3D image stacks of MDA-MB-231s (parental) cultured in the three hydrogel formulations that were fixed and fluorescently labeled for phosphorylated p38 (p-p38: red) and phosphorylated ERK (p-ERK: green) and counterstained with Hoechst (nuclei: blue). Scale bar = 100 µm. Quantification of (B) p-ERK mean fluorescence intensity, (C) p-p38 mean fluorescence intensity, and (D) p-ERK:p-p38 mean fluorescence intensity ratio for MDA-MB-231s (parental), BoM-1833s (bone-tropic), LM2-4175s (lung-tropic), BrM2a-831s (brain-tropic), and MCF7s after 15 days in culture in the indicated hydrogel formulation. * indicates statistically significant difference ($p<0.05$). n=5 z-stacks from 5 individual hydrogels. Values represent mean + standard deviation. *Figure adapted from [41] with permission from John Wiley and Sons.*

The common dormancy marker, p-p38, was expressed at significantly higher levels in cells cultured in non-permissive gels 2 and 3 across all five cell lines (Figure 3.7). Conversely, all cell lines cultured in permissive gel 1 expressed significantly higher levels of p-ERK compared to gels 2 and 3 (Figure 3.7C), indicating a proliferative state.

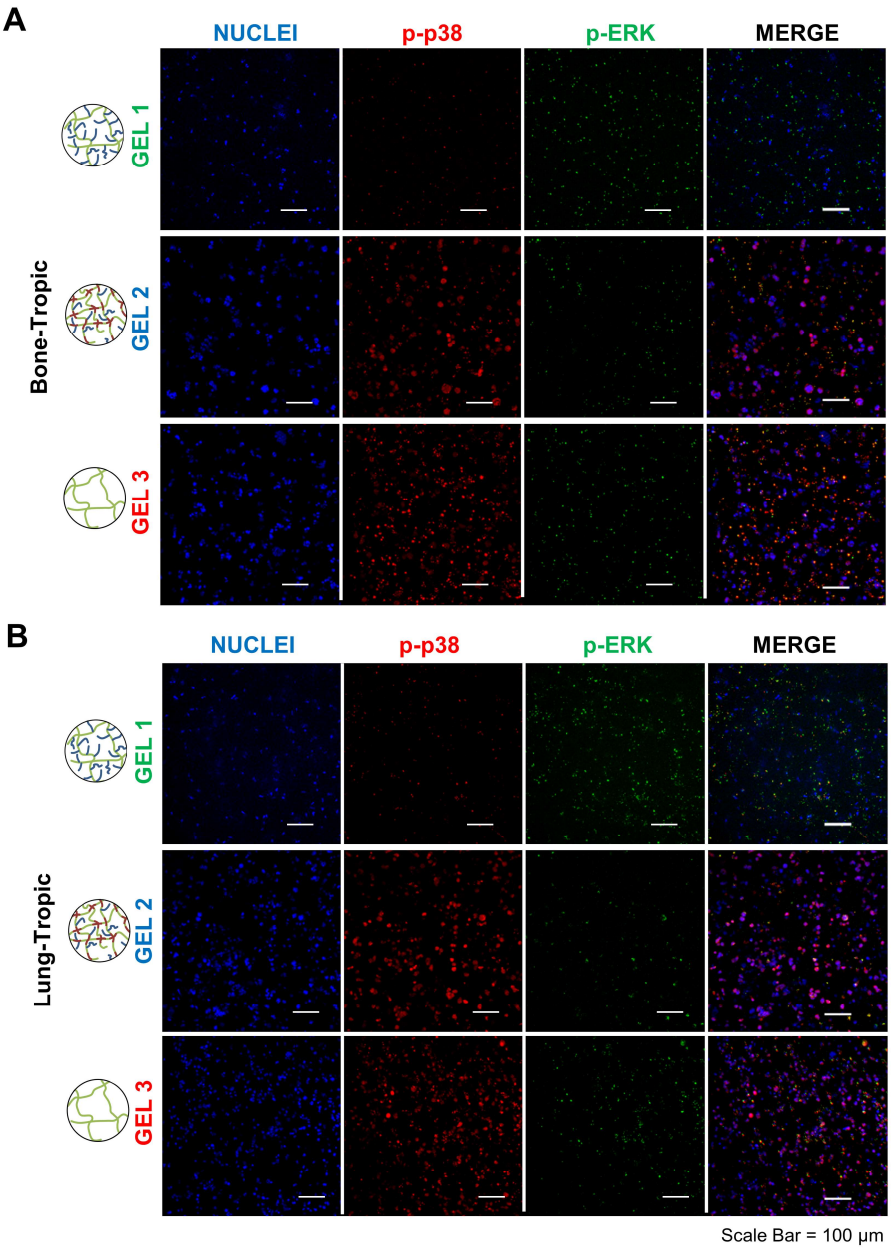

Figure 3.8: Phosphorylated p38 & ERK Expression Bone- and Lung-Tropic Cell lines. Representative maximum intensity z-projections from 3D image stacks of (A) BoM-1833s (bone-topic), and (B) LM2-4175s (lung-tropic) cell lines that were fixed and labeled for p-p38 (red) and p-ERK (green) and counterstained with Hoechst (nuclei: blue) after 15 days in culture in the indicated hydrogel formulation. n=6 z-stacks from 6 individual hydrogels. *Figure adapted from [41] with permission from John Wiley and Sons.*

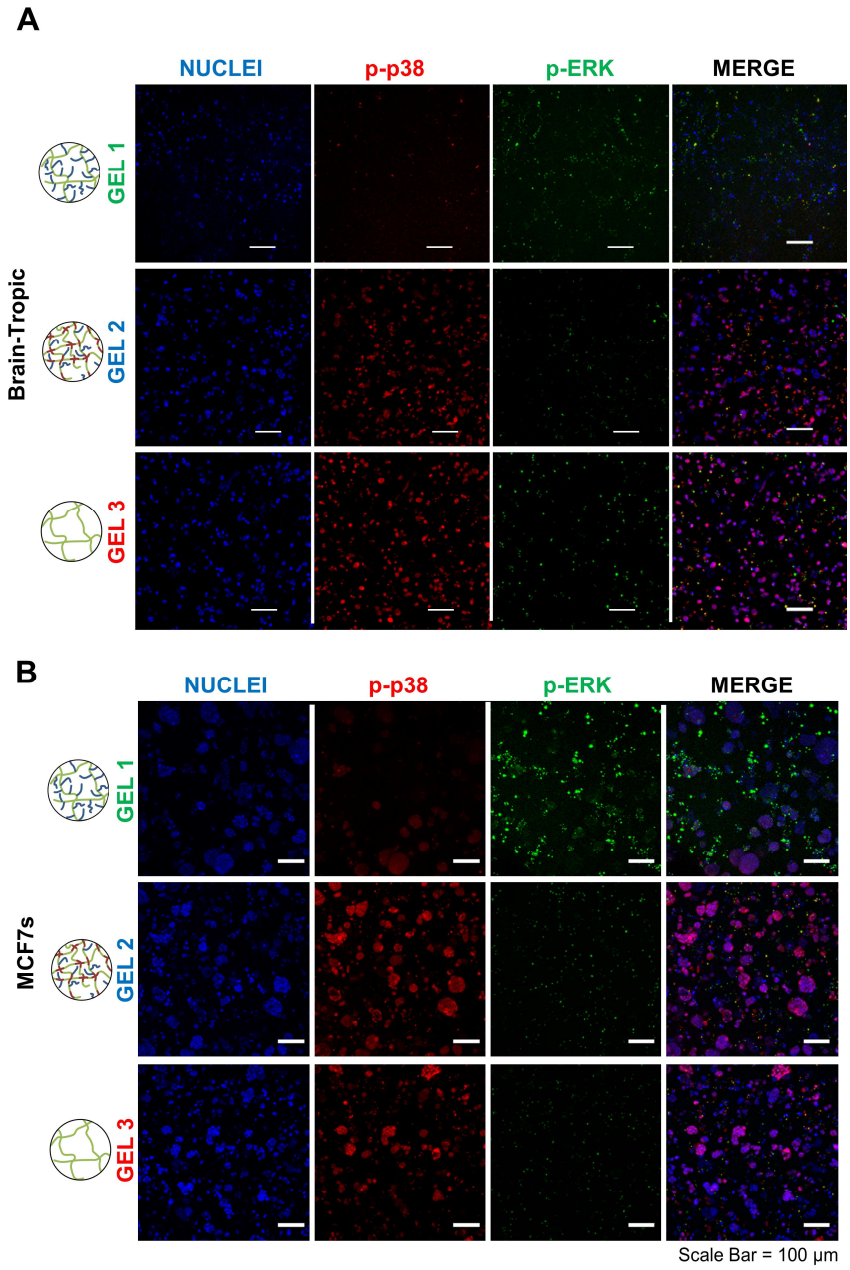

Figure 3.9: Phosphorylated p38 and ERK Expression in the Brain-Tropic 231s and MCF7s. Representative maximum intensity z-projections from 3D image stacks of (A) BrM2a-831s (brain-tropic), and (B) MCF7s that were fixed and labeled for p-p38 (red) and p-ERK (green) and counterstained with Hoechst (nuclei, blue) after 15 days in culture in the indicated hydrogel formulation. n=6 z-stacks from 6 individual hydrogels. *Figure adapted from [41] with permission from John Wiley and Sons.*

The p-ERK:p-38 ratio for each condition was measured. Results indicated a significantly higher p-ERK:p-38 ratio in permissive gel 1 compared to non-permissive gels 2 and 3 for all five cell lines (Figure 3.7D). In all cell lines, the p-ERK:p-38 ratio was greater than 4 (parental: 4.30 ± 2.94, bone: 4.63 ± 3.01, lung: 4.31 ± 2.96, brain: 4.74 ± 1.85, MCF7s: 5.9 ± 1.1) in permissive gel 1. The p-ERK:p-38 ratio significantly decreased in non-permissive gel 2 (parental: 0.24 ± 0.04, bone: 0.24 ± 0.05, lung: 0.24 ± 0.04, brain: 0.25 ± 0.05, MCF7s: 0.5 ± 0.2) and non-permissive gel 3 (parental: 0.31 ± 0.02, bone: 0.27 ± 0.06, lung: 0.26 ± 0.05, brain: 0.31 ± 0.06, MCF7s: 0.5 ± 0.1) (Figure 3.7D). These results indicate that all five cell lines cultured in non-permissive gels 2 and 3 displayed higher p-p38 expression compared to p-ERK, further validating their dormancy status as per established literature reports.

3.3.8 Classifying Hydrogel-Induced Cell Phenotype

To identify phenotypic states in the five cell lines induced by the three hydrogel formulations we applied a logic-based, multimetric classification approach (Figure 3.10A). A phenotype classification scheme was created based on well-established dormancy metrics[7,43] and general logic regarding anticipated behavior of breast cancer cells residing in a growth or dormant state. Hydrogel-induced phenotypes for each cell line, in each hydrogel formulation, were determined by applying the classification scheme to the measured metrics (Figure 3.10A) to categorize the resultant cell behavior as one of four phenotypes: (1) growth, (2) restricted survival, cellular dormancy, (3) balanced cellular dormancy, or (4) balanced tumor mass dormancy (Figure 3.10).

A

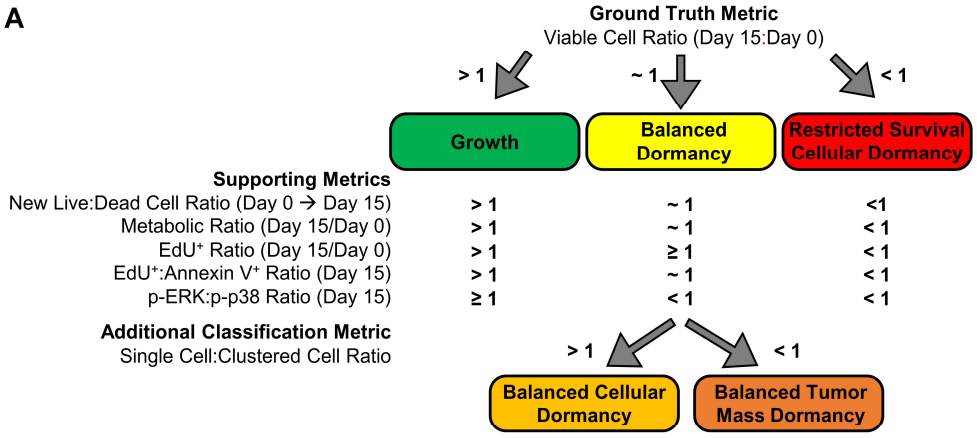

B

	Measured Metrics	Parental MDA-MB-231	Lung-Tropic LM2-4175	Bone-Tropic BoM-1833	Brain-Tropic BrM2a-831	MCF7
		Cell Type				
GEL 1	Viable Cell Ratio (D15/ D0)	1.7 ± 0.1*	1.6 ± 0.3*	1.5 ± 0.3*	1.9 ± 0.4*	1.2 ± 0.1*
	New Live:Dead Cell Ratio (D0→15)	18.7 ± 5.8*	13.8 ± 4.3*	18.8 ± 9.9*	18.9 ± 8.1*	7.8 ± 4.2*
	Metabolic Ratio (D15/D0)	12.5 ± 0.5*	5.9 ± 1.0*	8.8 ± 1.9*	6.1 ± 1.0*	5.1 ± 1.9*
	EdU+ Ratio (D15/D0)	6.1 ± 0.6*	3.4 ± 0.8*	5.3 ± 1.4*	4.3 ± 1.7*	3.5 ± 0.5*
	EdU+:Annexin V+ Ratio (D15)	7.1 ± 0.8*	3.8 ± 1.1*	4.6 ± 1.0*	3.6 ± 1.7*	15.3 ± 2.4*
	p-ERK:p-p38 Ratio (D15)	4.30 ± 2.94^	4.31 ± 2.96^	4.63 ± 3.01^	4.74 ± 1.85^	5.87 ± 1.08^
	Single Cell:Clustered Cell Ratio (D15)	0.02 ± 0.01*	0.05 ± 0.03*	0.02 ± 0.01*	0.03 ± 0.01*	0.16 ± 0.04*
GEL 2	Viable Cell Ratio (D15/D 0)	1.0 ± 0.05	1.0 ± 0.1	1.2 ± 0.1	1.2 ± 0.3	1.0 ± 0.1
	New Live:Dead Cell Ratio (D0→15)	1.2 ± 0.3	1.6 ± 1.2	1.5 ± 1.3	1.8 ± 1.5	0.7 ± 0.2
	Metabolic Ratio (D15/D0)	1.2 ± 0.4	1.7 ± 0.5	1.7 ± 0.5	1.3 ± 0.3	1.0 ± 0.1
	EdU+ Ratio (D15/D0)	0.8 ± 0.4	1.3 ± 0.6	1.9 ± 0.4*	2.1 ± 1.7*	1.1 ± 0.2
	EdU+:Annexin V+ Ratio (D15)	0.5 ± 0.3*	1.2 ± 0.6	1.4 ± 0.3*	1.2 ± 1.1	1.1 ± 0.2
	p-ERK:p-p38 Ratio (D15)	0.24 ± 0.04*	0.24 ± 0.04*	0.24 ± 0.05*	0.25 ± 0.05*	0.52 ± 0.20*
	Single Cell:Clustered Cell Ratio (D15)	5.0 ± 1.9*	3.3 ± 0.7*	0.09 ± 0.05*	0.08 ± 0.03*	0.13 ± 0.03*
GEL 3	Viable Cell Ratio (D15/D0)	0.4 ± 0.03*	1.0 ± 0.03	1.0 ± 0.1	1.0 ± 0.1	0.3 ± 0.02*
	New Live:Dead Cell Ratio (D0→15)	0*	1.3 ± 1.2	1.8 ± 1.7	1.5 ± 0.5	0*
	Metabolic Ratio (D15/D0)	1.0 ± 0.3	1.2 ± 0.5	1.3 ± 0.4	0.8 ± 0.3	0.9 ± 0.2
	EdU+ Ratio (D15/D0)	0.6 ± 0.1*	0.8 ± 0.4	0.9 ± 0.1	1.4 ± 0.4	0.8 ± 0.3
	EdU+:Annexin V+ Ratio (D15)	0.21 ± 0.02*	0.9 ± 0.5	1.5 ± 0.4	0.8 ± 0.2	0.3 ± 0.1*
	p-ERK:p-p38 Ratio (D15)	0.31 ± 0.02	0.26 ± 0.05*	0.27 ± 0.06*	0.31 ± 0.06*	0.49 ± 0.15*
	Single Cell:Clustered Cell Ratio (D15)	9.6 ± 8.2*	22.4 ± 11.3*	14.0 ± 2.1*	10.3 ± 4.3*	2.54 ± 1.20*

Figure 3.10: Defining Hydrogel-Induced Phenotypes Via Multi-metric Classification. (A) Phenotypic states were defined initially by a ground truth metric and subsequently supported by additional metrics. Balanced dormancy was further characterized as cellular or tumor mass via the single cell:clustered cell ratio. (B) Values for measured metrics and classified phenotypic states. The highlighted values indicate that the cells reside in the following states: growth (green), balanced cellular dormancy (yellow), balanced tumor mass dormancy (brown), and restricted survival cellular dormancy (red). The red and green text for some values in gel 2 indicate values that differed from the definitions used for classification. * indicates significant difference ($p<0.05$) from 1.0. *Figure adapted from [41] with permission from John Wiley and Sons.*

The viable cell ratio (number of viable cells at day 15 normalized to the number of viable cells at day 0 (6 h post encapsulation)) was used as a ground truth metric to determine whether the hydrogel induced a growth or dormant state. The logic driving this decision was that if the cells were in a dormant state then one would anticipate either no significant increase in the viable cell population (a viable cell ratio not statistically significantly different from 1) or potentially a decrease (a viable cell ratio significantly less than 1) if cell death also occurred. Conversely, if the hydrogel induced a growth state, then one would anticipate a significant increase in the viable cell population (a viable cell ratio significantly greater than 1). This ground truth metric allowed for classification of cells as residing in either a growth or dormant state. To further support classification based on the ground truth metric, and to further classify the hydrogel-induced phenotypes, additional logic-based and dormancy-associated metrics were implemented including the: (1) new live to new dead cell ratio, (2) metabolic ratio, (3) EdU^+ ratio, (4) EdU^+ to Annexin V^+ ratio, (5) p-ERK to p-p38 ratio, and (6) the single cell to clustered cell ratio as described below.

The new live to new dead cell ratio was quantified by counting the number of new live cells and the number of new dead cells formed in the hydrogel from day 0 (6 h post encapsulation) to day 15 and dividing the number of new live cells by the number of new dead cells over this time period. If the ratio is statistically significantly greater than 1, the hydrogel induced an increase in the cell population (growth) which further supports the ground truth metric (viable cell ratio). Conversely, if the new live to new dead cell ratio is statistically significantly less than 1, this indicates that cell death dominated over growth, and when combined with other supporting metrics, may indicate a restricted survival, cellular dormancy phenotype. In this state, a majority of

the cell population undergoes apoptosis with surviving cells existing in a quiescent, dormant state. This is relevant to what occurs *in vivo*, as studies have demonstrated the inefficiency of the metastatic process in which only a small percentage of DTCs survive after infiltration of foreign tissues.[6,77,78] If the new live to new dead cell ratio is not statistically significantly different than 1, this indicates a near perfect balance in cell proliferation and death (likely apoptosis, see Figure 3.3) and can help explain how the ground truth metric (viable cell ratio) achieved a value not significantly different than 1. We and others have defined this as a balanced dormancy state due to the near perfect balance in cell proliferation and death as further rationalized with additional metrics.[3,7,10-12] The results of the new live to new dead cell ratio can be further elucidated by examining the EdU^+ ratio. The EdU^+ ratio was quantified by counting the number of EdU^+ cells on day 0 (6 h post encapsulation) and day 15 and dividing the day 15 value by the day 0 value. It is important to note that the cells were serum-starved for 48 h prior to encapsulation in hydrogels. This was done for three reasons: (1) to synchronize the cell cycle, (2) to start the experiments with cells in a quiescent state, and (3) to ensure a similar starting state for all experiments which allows for the influence of the hydrogel properties to be more easily interpreted without other confounding factors. This also means that the number of proliferating cells at day 0 should be as low as it can get due to the 48 h serum starvation. Accordingly, if the hydrogel induced a growth state then one would anticipate the EdU^+ ratio to be statistically significantly greater than 1 as the population must increase through proliferation. Conversely, if the hydrogel is perceived as a harsh, unfavorable environment by the cells one would anticipate the EdU^+ ratio to be significantly less than 1 as proliferation would be inhibited. If the hydrogel formulation induced a

dormant state, then two outcomes are possible. The EdU^+ ratio could be significantly greater than 1 and the cell population still not increasing if cell proliferation was balanced by apoptosis. In this scenario the number of cells undergoing apoptosis would need to be similar to the number of cells proliferating to maintain a constant cell density over time. Another potential outcome is that the EdU^+ ratio is not significantly different than 1 indicating that the proliferation rate did not change from the initial value after 48 h serum starvation and encapsulation. The cell population in hydrogel formulations inducing this behavior would either stay constant if apoptosis was occurring or increase very slowly relative to cells cultured in hydrogels that induced a growth state if no apoptosis was occurring.

Additional insight into the results of the EdU^+ ratio can be achieved by examining the EdU^+ to Annexin V^+ ratio. At day 15, the number of cells labeled EdU^+ (actively proliferating) were counted, as well as the number of cells labeled Annexin V^+ (early apoptosis). Dividing the number cells EdU^+ by the number Annexin V^+ provides additional insight into the new live to new dead cell ratio and viable cell ratio by describing how the measured values were achieved. For example, an EdU^+ to Annexin V^+ ratio statistically significantly greater than 1 indicates that there were more actively proliferating cells than cells undergoing apoptosis (the primary mode of death observed in these studies). (Figure 3.3). Accordingly, one would also anticipate a new live to new dead cell ratio greater than 1, a viable cell ratio greater than 1, and an EdU^+ ratio greater than 1 in this case as the cell population would be increasing. When these three classification metric values are met, along with additional supporting metrics, the cells were classified as being in a growth state. Conversely, if the EdU^+ to Annexin V^+ ratio was statistically significantly less than 1, apoptotic death

outweighed proliferation and the hydrogel formulation induced a restricted survival state. In this case, one would anticipate the viable cell ratio, new live to new dead cell ratio, and EdU^+ ratio to all be significantly less than 1. An EdU^+ to Annexin V^+ ratio not statistically significantly different from 1 indicates a near perfect balance between proliferation and apoptosis and will result in a viable cell ratio and new live to new dead cell ratio not significantly different than 1 but could potentially have an EdU^+ ratio greater than 1, as long as the EdU^+ to Annexin V^+ ratio was not significantly different from 1, which again supports a balanced dormancy phenotype.

The metabolic ratio was quantified by dividing the metabolic activity measured on day 15 to that measured on day 0 (6 h post encapsulation) and provides additional insight into both the cell population density and metabolic activity. If one assumes that metabolic activity is not different between cells in a growth or dormant state then this ratio is additional support for the cell density measurements as cell density and metabolic activity would be linearly related in this case. This may not be the case as it has been shown that cells in a dormant state may switch from oxidative phosphorylation to glycolysis.[79-81] The Alamar blue assay utilized to quantify metabolic activity in this study accounts for both modes of metabolism and thus, if the mechanism of metabolism changed, would be accounted for in the data used for classification. Accordingly, if cells are actively proliferating, highly metabolic, and the cell population increasing, one would anticipate the metabolism to increase and thus a metabolic ratio statistically significantly greater than 1, further validating a growth state. Conversely, if the cell population significantly decreased due to cell death or if metabolic activity decreased due to quiescence one would anticipate a metabolic ratio significantly less than 1. If the cells are in a low metabolic, dormant state one would

anticipate the metabolic ratio to not be significantly different from 1 as the cells were serum starved prior to encapsulation and would have initially low metabolism at day 0. This indicates that cells classified as undergoing balanced dormancy in this study (metabolic ratio ~1) displayed a metabolic activity that was not significantly different from cells that were serum-starved for 48 h and thus a very low activity.

In addition to metrics utilizing temporal changes in proliferation, apoptosis, metabolism, and population density discussed above, a well-established, dormancy-associated metric was also applied: phosphorylated ERK and p38.[15,71,72] The phosphorylated ERK to phosphorylated p38 ratio as measured at day 15 is a predictor of whether cells will enter a dormant state. Work by Aguirre-Ghiso and colleagues has demonstrated that a ↓p-ERK:↑p-p38 ratio can shift cells from a state of tumorgenicity to dormancy *in vivo*.[71,72] Studies that quantified gene expression in dormant cancer support this result as p38, p38 regulated transcription factors, and genes that suppress ERK activation were all overexpressed in dormant cancer.[74] Accordingly, one would anticipate a p-ERK to p-p38 ratio statistically significantly greater than, or equal to 1, for cells residing in a growth state and statistically significantly less than 1 for cells residing in a dormant state. The temporal metrics concerning population density changes and the p-ERK to p-p38 ratio indicated that hydrogel formulation 1 (permissive gel 1) induced a growth state in all five cell lines.

All of the metrics discussed above were implemented to classify the resultant cell phenotype, as a function of cell line and hydrogel formulation, as either growth, balanced dormancy, or restricted survival, cellular dormancy. For cells residing in the balanced dormancy state, we observed two different responses in the five cell lines when cultured in non-permissive gel 2. In one response, a majority of the cell

population resided as solitary, individual cells and in the other the majority resided in cell clusters. To differentiate between these two responses, the single cell to clustered cell ratio was quantified. On day 15, the cells were fixed, fluorescently labeled with phalloidin and Hoechst, and imaged. The 3D image stacks were used to quantify the percent of the cell population residing as solitary, individual cells or in cell clusters. The single cell to clustered cell ratio was calculated by dividing the number of cells residing as solitary individuals by the number of cells residing in clusters. Accordingly, a value statistically significantly greater than 1 indicates that a majority of the cells were solitary whereas a value significantly less than 1 indicates that a majority of cells were residing in clusters. This metric was used to differentiate between cells residing in a balanced cellular dormant state (single cell to clustered cell ratio significantly greater than 1) from those residing in a balanced tumor mass dormant state (single cell to clustered cell ratio significantly less than 1).

The ground truth and supporting metrics, along with the rationale describing anticipated results, were applied to classify the phenotypes induced in the five cell lines cultured in the three hydrogel formulations (Figure 3.10B). Figure 3.10B provides the measured values for each metric for each cell line and hydrogel formulation. The data is color-coded and matches the phenotypes outlined in Figure 3.10A. The results demonstrate that permissive gel 1 induced a growth state in all five cell lines indicated by a >1 viable cell ratio and supported by a >1 new live:new dead cell ratio, significant increases (>1) in metabolic activity and the number of EdU^+ cells at day 15, significantly more EdU^+ than Annexin V^+ cells at day 15, a >1 p-ERK:p-p38 ratio, and cluster formation (Figure 3.10).

The results also demonstrate that non-permissive gel 3 induced a restricted survival, cellular dormancy state only in the parental 231 and MCF7 lines and a balanced cellular dormancy state in the three organotropic sublines indicating a potential cell line dependence where the sublines were able to survive better, albeit in a dormant state, in an unfavorable environment. Restricted survival, cellular dormancy was confirmed in the parental and MCF7 lines in non-permissive gel 3 by a <1 viable cell ratio, <1 new live:new dead cell ratio, <1 EdU^+ ratio, and <1 EdU^+:Annexin V^+ ratio, and <1 p-ERK:p-38 ratio (Figure 3.10B). All organotropic populations cultured in non-permissive gel 3 adopted a balanced cellular dormancy state characterized by a balanced (~1) viable cell ratio, new live:new dead cell ratio, EdU^+ ratio, EdU^+:Annexin V^+ ratio, and metabolic ratio, <1 p-ERK:p-p38 ratio, and >1 single cell:clustered cell ratio (Figure 3.10B).

Additional cell line differences were observed in non-permissive gel 2. The parental 231 line and lung-tropic subline both displayed balanced cellular dormancy while the bone- and brain-tropic sublines, and MCF7s adopted balanced tumor mass dormancy. It should be noted that the all of the black text in Figure 3.7B indicates measurements that matched the anticipated values while the two colored text values (EdU^+:Annexin V^+ ratio for the parental 231 line in gel 2 (red) and the same metric for the bone-tropic subline in non-permissive gel 2 (green)) varied from the anticipated values. As discussed in the previous text, one would anticipate that cells residing in a balanced dormancy state would have an EdU^+:Annexin V^+ ratio not significantly different from 1. However, parental 231s in non-permissive gel 2 had an EdU^+:Annexin V^+ ratio significantly less than 1 (0.5 ± 0.3) indicating apoptosis was higher than proliferation. A potential reason for this may be that proliferation and

apoptosis measurements were only taken at two timepoints (day 0 and day 15). Quantifying the number of proliferating and apoptotic cells with higher temporal resolution throughout the 15-day culture period may provide additional information regarding the rate of change in the proliferation/apoptosis ratio. Similarly, it was anticipated that the bone-tropic subline, when cultured in non-permissive gel 2, would have an EdU^+:Annexin V^+ ratio not significantly different from 1 but the measured value was 1.4 ± 0.3 and statistically significantly greater than 1. Similar to the parental line in non-permissive gel 2, this may be due to a lack of temporal measurements when analyzing proliferation and early apoptosis. Alternatively, this case may be similar to a moderate growth state that we previously characterized in other hydrogel formulations in the parental 231 line.[35] However, since bone-tropic cells in non-permissive gel 2 fulfill all other expected metrics for balanced dormancy, they were determined to reside in balanced tumor mass dormancy due to the high density of cell clusters measured.

3.3.9 "On-Demand" Reactivation of Dormant Breast Cancer Cells

Dormant cancer cells retain the ability to exit dormancy and re-enter the cell cycle, leading to tumor growth and metastatic relapse. Changes in microenvironmental cues or immune surveillance can alter downstream signaling to reactivate dormant cells.[82] To assess whether dormant breast cancer lines can be reactivated in this platform, hydrogel adhesivity was dynamically increased in non-permissive gel 3 after 15 days in culture, effectively turning non-permissive gel 3 into permissive gel 1. Cell-laden hydrogels in non-permissive gel 3 (5% w/v PEG-PQ, 0 mM PEG-RGDS, 0 mM NVP) were cultured for 15 days, allowing the cells to enter a dormant state. At day 15,

the RGDS density was dynamically increased via photocoupling of 10 mM PEG-RGDS, and the cell-laden hydrogels cultured for an additional 7 days.

To quantify changes in cell viability, viability was measured at day 22 (7 days post RGDS incorporation) and compared to values at day 15 (prior to RGDS incorporation). Prior to RGDS incorporation, viability was 45.8 ± 3.7% in the parental 231 line, 42.5 ± 2.5% in the MCF7 line, and ranged from 89.1-90.7% in the three organotropic sublines. At day 22, viability significantly increased to 95.0 ± 1.5% in the parental 231 line, 85.6 ± 2.0% in the MCF7 line, and ranged between 92.3-94.5% in the three organotropic sublines (Figure 3.11). To quantify the change in viable cell density, we measured the number of viable cells at day 22 and normalized it the number of viable cells at day 15. RGDS incorporation significantly increased the number of viable cells by 2.1 ± 0.2-fold in the parental 231 line, 2.2 ± 0.2 in the MCF7 line, 1.5 ± 0.1 in the bone-tropic line, 1.7 ± 0.1 in the lung-tropic line, and 1.5 ± 0.1 in the brain-tropic line (Figure 3.11C). Similarly, the percentage of the cell population EdU^+ was quantified to determine if dynamically increasing hydrogel adhesivity altered proliferation. Proliferation significantly increased from 9.4-14.0% prior to RGDS incorporation to 44.2-52.7%, values comparable to cells in the growth state in permissive gel 1 (33.8-47.1%) (Figure 3.11D). The parental 231 line increased from 14.0 ± 2.5% to 52.7 ± 4.0%, the MCF7 line increased from 12.8 ± 4.3% to 49.5 ± 2.5%, the bone-tropic line increased from 9.4 ± 1.2% to 51.3 ± 4.3%, the lung-tropic line increased from 7.5 ± 2.6% to 55.1 ± 4.0%, and the brain-tropic line increased from 13.0 ± 2.9% to 44.2 ± 5.5% EdU^+ cells. Similarly, the number of EdU^+ cells increased significantly between days 15 and 22 (parental: 4.3 ± 0.4-fold, MCF7s: 5.9 ± 1.0-fold, bone: 7.0 ± 0.6, lung: 5.7 ± 0.4, brain: 5.0 ± 0.8) (Figure 3.11E). Overall, the

results indicate that dynamically increasing hydrogel adhesivity via “on-demand” incorporation of RGDS significantly increased viability and proliferation, indicating the ability to reactivate dormant cancer cells using this platform and approach.

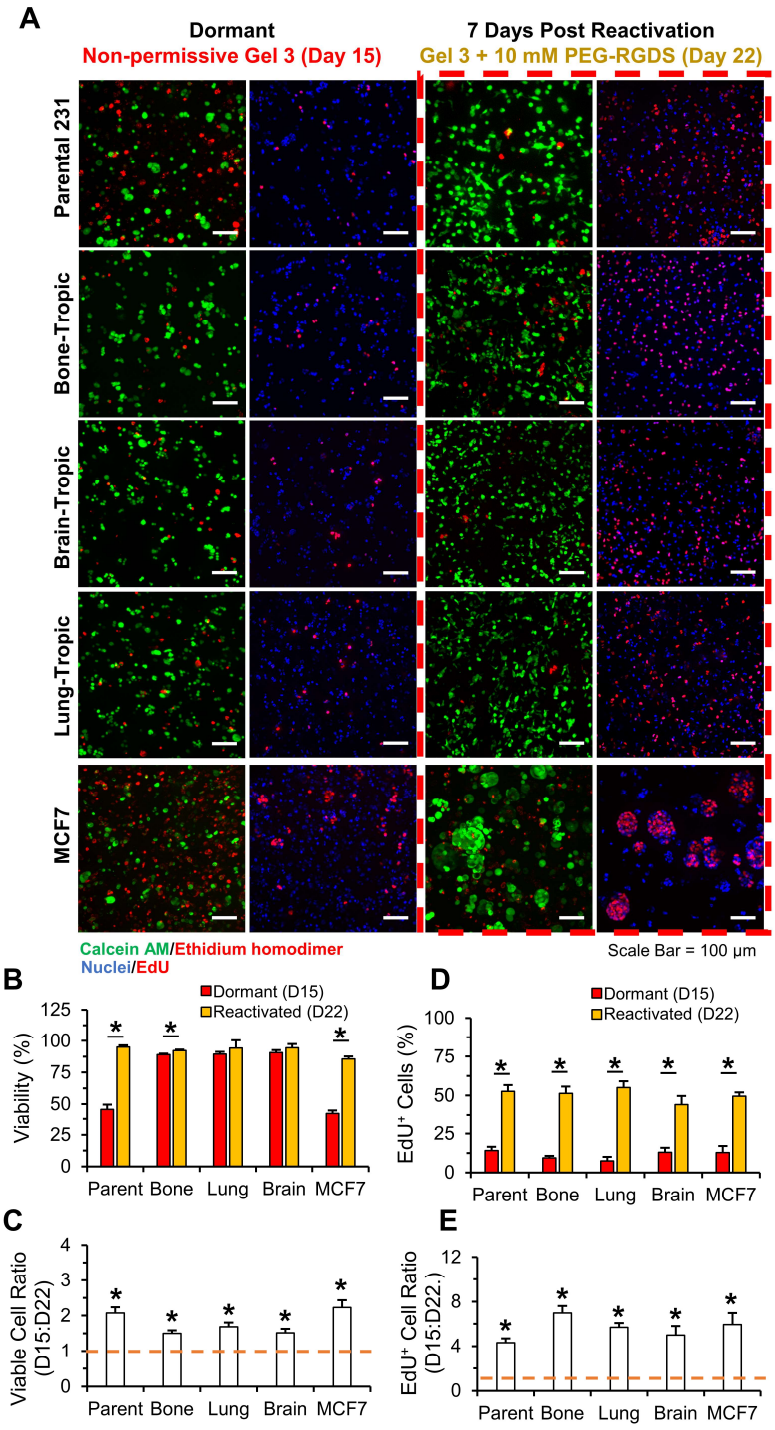
A
Dormant
Non-permissive Gel 3 (Day 15)
7 Days Post Reactivation
Gel 3 + 10 mM PEG-RGDS (Day 22)
Parental 231
Bone-Tropic
Brain-Tropic
Lung-Tropic
MCF7
Calcein AM/Ethidium homodimer
Nuclei/EdU
Scale Bar = 100 µm
B
Dormant (D15)
Reactivated (D22)
Viability (%)
Parent Bone Lung Brain MCF7
C
Viable Cell Ratio (D15:D22)
Parent Bone Lung Brain MCF7
D
Dormant (D15)
Reactivated (D22)
EdU+ Cells (%)
Parent Bone Lung Brain MCF7
E
EdU+ Cell Ratio (D15:D22.)
Parent Bone Lung Brain MCF7

Figure 3.11: Reactivation of Dormant Cells. (A) Representative maximum intensity z-projections from 3D image stacks of dormant MDA-MB-231s (parental), BoM-1833s (bone-tropic), LM2-4175s (lung-tropic), BrM2a-831s (brain-tropic), and MCF7s cultured in non-permissive gel 3 (0 RGDS, 0 NVP) at day 15 (columns 1 and 2). At day 15, cells were reactivated via incorporation of 10 mM PEG-RGDS, and cells were further cultured for 7 days (day 22) (columns 3 and 4). Cells were labeled with Calcein AM (green: live cells) and ethidium homodimer (red: dead cells) (columns 1 and 3) , or EdU (red: proliferative cells) and Hoechst (blue: nuclei) (columns 2 and 4). Quantification of (B) % viability when dormant (day 15) and reactivated (day 22) and (C) the number of reactivated viable cells at day 22 relative to dormant cells at day 15 prior to RGDS incorporation. Quantification of (D) proliferation at day 15 and day 22 and (E) the number of EdU^+ cells at day 22 relative to day 15 prior to RGDS incorporation. * indicates statistically significant difference ($p<0.05$). n=6 z-stacks from 6 individual hydrogels. Values represent mean + standard deviation. *Figure adapted from [41] with permission from John Wiley and Sons.*

3.4 Discussion and Conclusion

A better understanding of the molecular mechanisms that induce and maintain cancer dormancy is necessary for developing new strategies for the prevention and treatment of metastatic cancer. Tumor dormancy can be regulated by a multitude of factors (immune responses, nutrient deprivation, stromal cell signaling, etc.) including the tumor microenvironment.[7,83] In a favorable pre-metastatic niche, cancer cell survival is supported by ECM proteins and proteoglycans that allow cells to ligate the matrix to invade, migrate, and proteolytically degrade their surrounding matrix, and by pro-tumorigenic signaling which suppresses anti-tumor immune responses.[84] Here, we focused on the role of ECM properties in regulating breast cancer phenotype. Proteins in the ECM support cell-matrix interactions through integrin-mediated focal adhesions, which can activate pathways that influence cell fate. However, foreign environments that fail to promote these interactions in a non-permissive ECM can

induce a quiescent, dormant state. Additionally, dense matrices that physically confine cells or cell clusters via inhibition of matrix degradation can also induce dormancy.[7,30,31] To better understand how matrix properties influence cancer cell fate, *in vitro* studies have manipulated ECM properties via regulation of physical confinement (matrix degradation), cell-matrix interactions, and strain/deformation to induce dormancy.[7,31,33-36,69,85,86]

In this study, we tuned hydrogel properties to mimic favorable and unfavorable pre-metastatic niches, albeit in a simplified form. Permissive gel 1 aimed to mimic a favorable niche with high adhesivity and degradability. Similarly, in an unfavorable niche, DTCs may not be able to form integrin-mediated adhesions or efficiently degrade the surrounding matrix due to differences in protein composition compared to the organ they originated from. Again, we aimed to generally mimic this unfavorable environment using non-permissive gel 3 which contained no RGDS for integrin ligation and non-permissive gel 2 which contained moderate adhesivity but significantly decreased degradability. The three formulations were composed of the following: (permissive gel 1) 2.1 mM PEG-RGDS and 0 mM NVP, (non-permissive gel 2) 0.9 mM PEG-RGDS and 9.4 mM NVP, or (non-permissive gel 3) 0 mM PEG-RGDS and 0 mM NVP. We varied ligand density by altering the RGDS density incorporated into the hydrogel, and degradability by forming nondegradable crosslinks via incorporation of NVP to induce different phenotypic changes in parental and organotropic 231s. In chapter 1, we quantified how altering hydrogel composition alters key characteristics that can affect cancer cell phenotype including RGDS incorporation, mesh size, compressive modulus, swelling ratio, and degradation rate. Overall, results indicated that NVP incorporation (non-permissive gel 2) increased

RGDS incorporation and compressive modulus, while decreasing mesh size, swelling ratio, and degradation rate, compared to hydrogels without NVP (permissive gel 1, non-permissive gel 3).

We previously developed, thoroughly characterized, and implemented a suite of sixteen unique hydrogel formulations with well-controlled, systematic variations in hydrogel chemical (ligand density and degradability) and mechanical (elasticity, pore size, swelling) properties to regulate the fate of the parental 231 line.[35] The results of that study, which investigated the influence of a broader landscape of hydrogel properties on the fate of the 231 parental line, indicated that ligand density and degradability had the most influence over cell fate. In this study, we utilized three of the sixteen formulations that induced distinct dormant and growth phenotypes in the 231 parental line to investigate their influence on three organotropic sublines, and MCF7s. While this study did not investigate the entire hydrogel property landscape as before, we make the claim that ligand density and degradability will likely have the most influence on cancer cell fate based on our previous work as well as the data presented here. With that said, there are differences in elasticity between non-permissive gel 2 and permissive gel 1 and non-permissive gel 3. Non-permissive gel 2 had an elastic modulus of 10.1 ± 0.5 kPa 6 h post cell encapsulation while gels 1 and 3 had a value of 4.6 ± 0.4 kPa. After 15 days in culture, the elastic moduli of the gels decreased with non-permissive gel 2 at 7.6 ± 0.8 kPa and gels 1 and 3 at 4.2 ± 0.6 kPa. Since the values are still significantly different, one cannot rule out the possibility that elasticity will play some role, but as stated, our previous study[35] indicated it was a minor role compared to ligand density and hydrogel degradability. A limitation of our polymerization scheme is that hydrogel degradability and elasticity are coupled,

meaning that changing one changes the other. To independently tune these two parameters would require the implementation of multi-arm PEG chemistry to gain independent control over these parameters[87-90] and is of interest in future studies.

After serum starvation, cells were encapsulated in one of three hydrogel formulations. While we anticipate elasticity played a minor role in influencing cancer cell fate, we found that ligand density had a significant influence on cancer cell phenotype. This influence was highlighted by observed hydrogel-induced differences in cell behavior between permissive gel 1 and non-permissive gel 3. Permissive gel 1 contained a high level of adhesive ligand density (0.9 mM PEG-RGDS) and 0 mM NVP, which supported integrin-mediated cell adhesion and cell mediated-hydrogel degradation, encouraging proliferation and survival in all five cell lines. However, when RGDS was excluded from the hydrogel in non-permissive gel 3 (0 mM PEG-RGDS) cell-matrix adhesion was inhibited, leading to different phenotypes. This formulation resulted in high levels of cell death in (~40% viability) the parental 231s and MCF7 lines. Therefore, parental 231s and MCF7s in non-permissive gel 3 were determined to be in a restricted survival, cellular dormancy state. Interestingly, organotropic cells were not as sensitive to absence of RGDS. Viability at day 15 remained >88.5% for all three organotropic sublines cultured in non-permissive gel 3. Furthermore, organotropic cells in non-permissive gel 3 were categorized to be in a balanced cellular dormancy state. Increased survival in the organotropic sublines may be due to differences in gene expression.[38-40] While dormancy was induced in all five cell types in non-permissive gel 3, there were distinct differences between the parental 231s, MCF7s, and organotropic sublines, potentially due to the nature of how the organotropic sublines were developed. The sublines were selected via multiple rounds

of *in vivo* inoculation.[38-40] Subpopulations of cells that survived and metastasized to either the bone, lung, or brain were collected. These subpopulations express specific genes that promote their invasion and subsequent survival in their respective organ.[38-40] These pro-survival genes may also allow organotropic cells to survive in unfavorable conditions in which the parental 231 cells displayed greater cell death, potentially explaining the results observed in gel 3. Another factor investigated in this study was matrix degradability, highlighted by comparing results attained from permissive gel 1 and non-permissive gel 2. Non-permissive gel 2 has significantly decreased degradability compared to permissive gel 1 due to increased crosslinking with a non-degradable crosslinker (NVP) during photopolymerization. Non-permissive gel 2 induced different phenotypes in the five cell lines with the parental and lung-tropic lines entering balanced cellular dormancy and the bone- and brain-tropic, and MCF7 lines entering balanced tumor mass dormancy.

Distinct gene expression profiles among organotropic lines may account for differences observed in the behaviors induced by non-permissive gel 2. For instance, brain-tropic cells are known to overexpress ST6GALNAC5[40] which is a sialyltransferase that transfers sialic acid to oligosaccharides that can alter both cell-cell and cell-ECM interactions.[91,92] ST6GALNAC5 mediates infiltration into the brain by enhancing adhesion to, and interactions with, brain endothelial cells allowing penetration through the blood brain barrier.[40] In the same manner that ST6GALNAC5 mediates cell-ECM interactions in the brain, ST6GALNAC5 may also alter ECM interactions in the hydrogels implemented here, leading to the observed existence as cell clusters rather than solitary cells observed in non-permissive gel 2. Bone-tropic cells overexpress genes that aid in their survival and facilitate homing, invasion,

angiogenesis, and osteolysis in the bone marrow.[38] Overexpressed genes include chemokine receptor type 4 (CXCR4), matrix metalloproteinase 1 (MMP1), fibroblast growth factor 5 (FGF5), connective tissue growth factor (CTFG), interleukin 11 (IL-11), follistatin, and proteoglycan-1.[38] Proteoglycans are proteins with anionic glycosaminoglycans that provide hydration and swelling and can alter ECM composition.[93] Proteoglycans are also involved in cell signaling,[94] growth factor sequestration,[95] and modulating cell adhesion and proliferation.[96,97] It is possible that bone-tropic cells cultured in non-permissive gel 2 adopted a clustered morphology and increased proliferation due to the bioactive functions of increased proteoglycan-1 expression although further experimentation is required to test this hypothesis. In non-permissive gel 2, the parental 231s had statistically significantly lower proliferation than apoptosis as demonstrated by an EdU^+:Annexin V^+ ratio of 0.5±0.3, while bone-tropic sublines displayed more proliferation with an EdU^+:Annexin V^+ ratio of 1.4±0.3. Both of these values deviated from the anticipated value of ~1.0. However, in both cases the viable cell population and new live to new dead ratio remained constant, with no significant increase or decrease (ratio ~1.0). Additionally, in both cases all other metrics (metabolic ratio, and p-ERK:p-38 ratio) supported a balanced dormant state. A potential reason for this discrepancy may be that we only monitored changes in proliferation and early apoptosis at two timepoints, 6 h and 15 days post encapsulation. Additional measurements between these two timepoints could provide additional insight regarding temporal changes in proliferation and apoptosis throughout the culture period.

We implemented the viable cell ratio (number of viable cells at day 15 normalized to the number of viable cells at day 0) as a ground truth metric to classify

hydrogel-induced phenotypic states. This is based on the logic that cells in a dormant state would either display either (1) no significant increase in the number of viable cells (~1 ratio), or (2) a decrease in viable cell population (<1 ratio) if dormancy was accompanied by apoptosis. In contrast, one would anticipate that a hydrogel that induced a growth state would display a significant increase in the viable cell population (>1 ratio). To support this initial characterization, we implemented supporting metrics including the new live to new dead cell ratio to indicate the balance between cell survival and apoptosis, the metabolic ratio to provide insight into cell population density and metabolic activity, the EdU^+ ratio to account for changes in proliferation, and the EdU^+ to Annexin V^+ ratio to measure the balance between proliferation and apoptosis. Similarly, other studies have used viability, metabolic activity, proliferation, and other phenotypic assays to identify and classify dormant cell populations.[7,42-44].

Another approach to identifying dormant populations is quantifying the expression of dormancy markers including p27, NR2F1, and the p-ERK/p-p38 ratio.[43,71] In this study, we measured p-ERK and p-p38 concentration using immunofluorescent labeling for further validation. While phenotypic metrics can indicate observable traits in parental and organotropic 231s and MCF7s, they do not provide information regarding ECM-induced genetic changes, which is an alternative method that can be used to determine dormancy. Segall and colleagues used published data from experimental models, breast cancer cell line expression data, and clinical studies with primary breast cancers to develop a cell dormancy signature consisting of 22 upregulated and 27 downregulated genes used to calculate a dormancy score. Higher scores indicate a higher probability that DTCs will enter a dormant state.[64]

Genes included in this signature are involved in a multitude of cellular processes including cell cycle regulation, developmental processes, motility, and differentiation. Another advantage of using gene expression analysis is the ability to compare *in vitro* genetic expression levels to that observed *in vivo*, thereby validating clinical relevance.[69] While we did not include gene expression analysis here, future studies to quantify similarities and differences in gene expression between the four phenotypic states could further support classification and insight into hydrogel-induced changes in behavior. While other approaches can be used to identify dormant populations, we believe that quantifying the phenotypic changes in encapsulated 231s and MCF7s and using logic-based, multimetric classification is a strong indication of hydrogel-induced phenotypic growth or dormant states in this platform.

To investigate how tuning ECM composition can alter cell phenotype, we aimed to mimic unfavorable conditions of the premetastatic niche in which cells are unable to establish integrin-mediated adhesions or proteolytically degrade their surrounding matrix. While we did not incorporate organ-specific ECM peptides to control these processes, although this is of interest in future studies as organ-specific hydrogel formulations can significantly impact cell behavior.[88,98] Additionally, while the hydrogels used in these studies ranged from ~4-7 kPa, the formulations were not tuned to match brain (~1-4 kPa)[99], bone marrow (~0.5-1.5 kPa)[99], or lung (~1-5 kPa)[100] as the focus was to investigate matrix adhesivity and degradability, though future work that incorporates organ-specific mechanical and biochemical properties is of interest.

It is important to note that the cells were serum-starved for 48 h prior to encapsulation to synchronize the cell cycle and ensure a similar starting point for all

experiments thereby making it possible to compare the resulting cell behavior across all five cell lines and three hydrogel formulations without having to account for other confounding factors. We anticipate that the same phenotypes would be achieved without serum starvation prior to encapsulation but that the time to achieve them would vary. For example, one would anticipate cells in the growth state (permissive gel 1) to have much higher cell densities and proliferation rates at the day 15 time point due to being highly metabolically active during encapsulation if serum starvation was not implemented. Similarly, one would anticipate cells cultured in non-permissive gels 2 and 3 to start off with higher values for metabolic activity, proliferation, etc. and it could take longer than 15 days to end up with the same resultant dormant phenotype. Also, since the cells would have a different initial behavior at day 0 (6 hours post encapsulation), the logic-based classification would need to be reworked. For example, cells classified as residing in a balanced dormancy state are partially defined by the supporting metric, metabolic ratio, not being statistically significantly different than the value 1 due to serum starvation-induced low metabolic activity prior to encapsulation. If the cells were not serum starved, then their day 0 metabolic activity value would be higher and thus the defining metric would need to be changed from ~1 to <1 to account for this initial condition. This is important to note as other groups may utilize the classification scheme presented here (Figure. 3.10A) for studies that do not implement serum starvation prior to encapsulation and need to take the initial conditions into account.

While other factors including nutrient/oxygen deprivation, secondary cell signaling, and immune responses can play a role in inducing and maintaining cancer dormancy,[7] this study excluded these factors to solely focus on ECM-induced changes.

We previously demonstrated that the differences in pore size between the hydrogel formulations had no statistically significant impact on the transport of 3 kDa dextran[35] indicating that no differences in the transport of nutrients, oxygen, or other small molecules occur between the hydrogel formulations thereby eliminating differences in transport as a source of phenotypic control in this study. There is still the potential of inducing transport limitations if large volume hydrogels are implemented which could impact cell phenotype. To avoid this situation, we implemented 500 μm thick hydrogels, which is well below the distance that is necessary to develop potentially harmful nutrient and oxygen limitations for cells in the center of the hydrogels.[36] However, future studies incorporating the influence of other environmental factors could provide additional insights into the synergistic roles of these factors in regulating breast cancer cell fate.

Metastatic relapse can occur when changes in environmental cues encourage dormant cells to re-enter the cell cycle for proliferation. Several factors including secondary cell signaling, angiogenesis, and chronic inflammation can activate this phenotypic switch.[82] Integrin signaling has emerged as a critical regulator of reactivation both *in vitro* and *in vivo*.[73] In this study, we investigated if dynamically increasing hydrogel adhesivity can be used to reactivate previously dormant cancer cells. PEG-RGDS was incorporated to non-permissive gel 3 (0 mM PEG-RGDS) after 15 days in culture effectively converting non-permissive gel 3 into permissive gel 1 and the cells were cultured for additional 7 days. Results indicated that the number of viable cells significantly increased between 1.5-2.1-fold and the number of EdU^+ cells increased between 4.3-7.0-fold at day 22 (7 days post RGDS coupling) compared to day 15 (prior to RGDS incorporation) (Figure 3.11). Furthermore, the percentage of

viable and EdU^+ cells increased to values observed in the growth phenotype (permissive gel 1). These results demonstrate the ability to reactivate dormant cell populations and mimic metastatic relapse. The ability to model the transition into and out of dormancy is a powerful tool that could be particularly useful to study the mechanisms driving these cellular events.

Additionally, while we focused on breast cancer, other cancer types can also undergo dormancy and are of interest to our group. Furthermore, future studies investigating differences in gene expression between cell and gel types can be performed to obtain a better understanding of the underlying mechanisms driving ECM-induced dormancy in this platform.

In conclusion, this study investigated the role of hydrogel properties in regulating the phenotype of parental 231s, three organotropic sublines, and MCF7s. We tuned hydrogel properties to induce four distinct phenotypic states. A PEG-RGDS rich and highly degradable matrix (permissive gel 1) promoted growth in all cell types, while reducing ligand density and matrix degradability (non-permissive gel 2) induced balanced cellular dormancy in parental and lung-tropic 231s, and balanced tumor mass dormancy in bone- and brain-tropic 231s, and MCF7s. Absence of PEG-RGDS (non-permissive gel 3) led to restricted survival, cellular dormancy in the parental 231s and MCF7s, and balanced cellular dormancy in the three organotropic sublines. A distinct feature of dormant populations, reactivation, was also achieved in all five cell lines through a dynamic increase in hydrogel adhesivity. Overall, these results indicate the ability to mediate cancer cell fate and regulate dormancy status via facile, controlled changes to hydrogel properties. We envision that future implementation of this hydrogel-based platform may help identify potential anti-dormancy therapeutic targets

for pre-emptive treatment of dormant cancers prior to reawakening and metastatic progression. Our efforts towards this goal are explained in the following chapters.

Chapter 4

HYDROGEL-INDUCED DORMANCY AND REACTIVATED CELL CHEMORESISTANCE

Sections in this chapter have been adapted from the following articles:

(1) Farino CJ, Pradhan S, Slater JH. The Influence of Matrix-Induced Dormancy on Metastatic Breast Cancer Chemoresistance. ACS Applied Biomaterials 2020, 3(9), 5832-5844.

(2) Farino Reyes CJ, Pradhan S, Slater JH. The Influence of Ligand Density and Degradability on Hydrogel Induced Breast Cancer Dormancy and Reactivation. Advanced Healthcare Materials 2021, 10(11), 2002227.

4.1 Introduction

Despite significant advances in cancer detection, diagnosis, and treatment, metastasis (dissemination, invasion, and proliferation of tumor cells in secondary organs) is still responsible for 90% of cancer-associated mortality.[2] As described in chapters 2 and 3, the latency period that often occurs prior to metastatic relapse can serve as a therapeutic "window of opportunity" to eliminate dormant cells or prevent their reactivation. One major roadblock in treating dormant cancer cells and preventing cancer recurrence is that current chemotherapeutics often fail to effectively treat dormant, quiescent cells. Several patient studies indicate that dormant DTCs resist common forms of chemotherapy.[15-20] For example, patients treated with adjuvant therapy that had DTCs present in bone marrow aspirates displayed a significantly decreased 5-year survival rate.[17]

In vitro platforms that induce cancer dormancy can be implemented to characterize chemoresistance.[31,33,101] For example, ECM-induced dormant cells displayed a 0.9 to 10.6-fold increase in the half maximal inhibitory concentration (IC_{50}) compared to control conditions.[33] Several *in vitro* studies have confirmed these findings and have even used chemotherapy as a method of inducing dormancy.[7,31,33,101,102] One study seeded 231s in an *ex vivo* system and used standard chemotherapeutics to selectively target and eliminate proliferating 231s while dormant sub-populations remained viable.[103] While dormant cancer cells can display increased chemoresistance, the underlying mechanisms dictating this resistance remain elusive and platforms available for such studies are lacking. Current hypotheses state that cytotoxic therapies meant to target proliferative cells fail to target quiescent, dormant DTCs,[31,54] while others suggest dormant cells may have evolved mechanisms (such as increased expression of efflux pumps) to increase resistance to therapy.[54,103,104] An understanding of how ECM properties induce dormancy-associated chemoresistance could potentially lead to the development of therapeutics to prevent metastasis or relapse.

Towards this effort, in chapters 2 and 3 we demonstrated the ability to tune the biochemical and mechanical properties in three hydrogels (permissive gel 1, non-permissive gels 2 and 3) to induce either (1) growth, (2) balanced tumor mass dormancy, (3) balanced cellular dormancy, or (4) restricted survival dormancy in parental 231s, 231-derived organotropic sublines (BoM-1833s (bone-tropic), LM2-4175s (lung-tropic), BrM2-831s (brain-tropic)), and ER^+ MCF7s. Additionally, we demonstrated the ability to reactivate dormant cells in non-permissive gel 3 via RGDS incorporation. In this chapter, we used this dormancy and reactivation platform to

characterize chemoresistant behavior of dormant parental 231, organotropic 231s, and MCF7s compared to cells in a growth state.[45]

Parental 231s were encapsulated and cultured to induce a growth, dormant, or reactivated phenotype, exposed to doxorubicin (DOX), paclitaxel (PAC), or 5-fluorouracil (5-FU) for 48 h, labeled for live cells, imaged, and analyzed to assess the efficacy of each drug and quantify differences in cellular responses among the three phenotypic states. For all three drugs tested, parental 231s undergoing either restricted survival or balanced cellular dormancy demonstrated significantly increased chemoresistance compared to parental 231s in the growth state. For instance, dormant parental 231s in non-permissive gels 2 and 3 exposed to PAC displayed statistically significant higher cell viability compared to those in the growth state (permissive gel 1), with >72% of dormant cells viable compared to 39 ± 4% of growing cells when exposed to 1 mM PAC, compared to their respective vehicle control conditions (Figure 4.2). Similarly, dormant parental 231s exposed to 5-FU displayed significantly greater cell viability, with >93% cell viability in 231s residing in either dormant state, compared to 75 ± 5% for cells in the grow state at 10 mM 5-FU, compared to their respective vehicle control conditions (Figure 4.4). For DOX, studies were also performed on organotropic and MCF7 cell lines. Results showed that half maximal effective concentration (EC_{50}) values obtained from DOX exposure were significantly greater in dormant cells for all five cell lines tested, compared to growing cells (Figure 4.5, 4.6). Furthermore, reactivated cells sustained this chemoresistance, with significantly greater EC_{50} values compared to both dormant and growing states of the same cell type (Figure 4.5, 4.6).

To investigate if DOX transport played a role in chemoresistance observed in dormant and reactivated cells, intracellular DOX accumulation rate was quantified via intensity measurements of DOX autofluorescence over 48 h. DOX accumulated at a significantly greater rate in growing cells in permissive gel 1 compared to dormant (non-permissive gels 2 and 3) and reactivated cells in most cases (Figure 4.7). To determine DOX localization, nuclear to cytoplasmic (NC) drug ratio was also quantified in growing, dormant, and reactivated cells (Figure 4.8). Corresponding with accumulation results, data indicated that dormant and reactivated cells had significantly lower NC ratios compared to growing cells, suggesting that dormancy-associated chemoresistance may be due to both decreased drug intracellular accumulation and nuclear localization, at least for DOX.

These results demonstrate how tuning matrix properties alter parental 231, organotropic 231, and MCF7 phenotypes and subsequent chemoresistance, lends additional validation that this hydrogel platform can be used to induce breast cancer dormancy, and supports its use for future development and testing of new anti-dormancy therapeutic approaches. While this platform does not include other microenvironmental stimuli that influence dormancy such as immune responses, hypoxia, nutrient deprivation, soluble factors, and secondary cell signaling, the results highlight the contributions of hydrogel properties in inducing and maintaining cancer dormancy and the influence of matrix properties on dormant cancer chemoresistance.

4.2 Methods

Methods used for PEG Macromer Synthesis and Characterization, Cell Encapsulation, Reactivation, and measuring PEG-RGDS incorporation, cell viability, and degradation rate were performed as described in Chapters 2 and 3.

4.2.1 Measuring Drug Responses in 2D

Parental 231s were trypsinized, counted, and seeded in a fibronectin coated (10 μg/mL), 96 well plate at a density of 5,000 cells/well in serum-containing media. To measure the drug response of cells independent of encapsulation, we replicated pre-encapsulation conditions by allowing the cells to adhere overnight followed by culture in serum-free medium for 48 h. DOX, PAC, and 5-FU were purchased (Cayman Chemical) and reconstituted in DMSO to a stock concentration of 172.4, 58.5, and 384.6 mM, respectively. Stock solutions were diluted in media to a range of concentrations: DOX (0.001, 0.01, 0.1, 1, 10, 100, or 1000 μM), PAC (0.001, 0.01, 0.1, 1, 10, or 100 μM), and 5-FU (0.001, 0.01, 0.1, 1, 10, 100, or 1000 μM) and added to the 231s for 48 h (n=6 wells per concentration).[35] At the highest drug concentration tested, the DMSO concentration remained ≤0.1% (v/v); thus, 0.1% (v/v) DMSO was used as a vehicle control in 2D studies. Cells were rinsed in PBS twice to remove excess media, followed by labeling with a Live/Dead® cell viability kit (Invitrogen). Only live cells were labeled, as dead cells detached from the wells and were washed away. Labeled cells were imaged using the proper filter cubes and analyzed using FIJI software (NIH).

4.2.2 Measuring Drug Responses in Cells Cultured in Different Hydrogels

DOX, PAC, and 5-FU stocks were diluted in media to desired concentrations: DOX (0.001, 0.01, 0.05, 0.1, 0.55, 1, or 2 mM), PAC (0.05, 0.1, 0.55, or 1 mM), and 5-FU (1.0, 4.0, 7.0, or 10 mM). At the highest concentrations tested, the DMSO concentration ranged between 1-2% (v/v) for all drugs used. A vehicle study was conducted and showed no significant differences in cell viability between 1 or 2% (v/v) DMSO and serum-containing media (Figure 4.3). Thus, all vehicle controls used

in this study contained media with 1% (v/v) DMSO. We also tested higher concentrations (18%, 26% (v/v)) of DMSO required to use higher doses of PAC and 5-FU, however these concentrations were cytotoxic to parental 231s (Figure 4.3) and therefore not used.

Cell-laden hydrogels that had been cultured for 15 (gel 1, 2, 3) or 22 days (reactivated) were rinsed with PBS, and incubated in a given concentration of DOX, PAC, 5-FU, or a vehicle control for 48 h. Next, cells were rinsed with PBS to remove excess media, and labeled with a Live/Dead® cell viability kit (Invitrogen) in PBS for 30 min, according to the manufacturer's instructions. The hydrogels were rinsed with PBS for 10 min to remove excess stain, placed on coverslips, and imaged using structured illumination on a Zeiss AxioObserver Z1 inverted fluorescent microscope as previously described.[34-36] Fluorescent z-stacks (z-height: 150 μm) were acquired approximately at the center of the hydrogels, between the bottom and top surfaces of each sample, and analyzed using FIJI software (NIH). Due to the red autofluorescence of DOX, only the live cells were imaged for viability studies. To quantify cell viability, the number of live cells was normalized to the number of live cells measured in the vehicle control. A minimum of 6 z-stacks from 6 individual hydrogels were analyzed for each condition.

4.2.3 Doxorubicin Accumulation and Localization

After 15 (gel 1, 2, 3) or 22 days (reactivated) in culture, cell-laden hydrogels were exposed to 0.05 mM DOX for 48 h. To measure accumulation, 6 hydrogels for each formulation were imaged at varying time points over 48 h (1, 2, 3, 4, 5, 6, 12, 24, 36, 48 h).[105-107] To determine DOX accumulation over time, a sum z-projection was acquired from each z-stack and the mean fluorescence intensity of each projection was

measured. Background noise was accounted for by measuring the intensity of five background regions that did not contain cells for each projection. These background measurements were averaged and subtracted to obtain DOX mean fluorescence intensity. To obtain DOX accumulation rate at 0.05 mM DOX, mean fluorescence intensity was plotted over time and the slope of the linear portion of the graph (between 0-6 h) was determined to be the accumulation rate (h^{-1}). Measurements were obtained from a minimum of 6 z-stacks from 6 individual hydrogels for each experimental condition.

To measure DOX localization, cells exposed to 0.05 mM DOX for 48 h were rinsed with PBS, co-stained with Hoechst 33342 to locate cell nuclei, and imaged. Sum z-projections of each z-stack were used to acquire fluorescence intensity measurements of the cytoplasmic and nuclear regions, with a minimum of 70 cells measured per image. Mean DOX intensity in the nucleus was divided by mean cytoplasmic intensity to obtain nuclear to cytoplasmic ratio for each cell in a total of 4 z-stacks obtained from 4 individual hydrogels for each experimental condition.

4.2.4 Statistical Analysis

For statistical comparison between viability values, distribution normality was assessed via quantification of skewness and kurtosis, where values within ±2 indicated a normal distribution. Equal variance among groups was additionally evaluated. A one-way analysis of variance (ANOVA) with a post-hoc Tukey-Kramer test was implemented to determine statistical significance between multiple groups. Unless otherwise indicated, $p<0.05$ was considered statistically significant. OriginLab software was used to fit DOX viability data. A nonlinear, growth/sigmoidal curve fit using a dose response function with a Levenberg Marquardt iteration algorithm was

performed and allowed to converge for all conditions with a chi-square tolerance of 1E-9.

4.3 Results

4.3.1 Response of MDA-MB-231s to Doxorubicin, Paclitaxel, and 5-Fluorouracil in 2D Culture

Preliminary experiments to determine DOX, PAC, and 5-FU efficacy in parental 231 cells cultured in 2D were performed. Parental 231s were cultured on 96 well plates and serum-starved for 48 h, following the same protocol used for encapsulation for ease of comparison. The 231s were exposed to drug-containing medium at the following concentrations (DOX: 0.001, 0.01, 0.1, 1, 10, 100, or 1000 μM; PAC: 0.001, 0.01, 0.1, 1, 10, or 100 μM; and 5-FU: 0.001, 0.01, 0.1, 1, 10, 100, or 1000 μM) for 48 h. The live 231s were fluorescently labeled, imaged, and quantified (Figure 4.1).

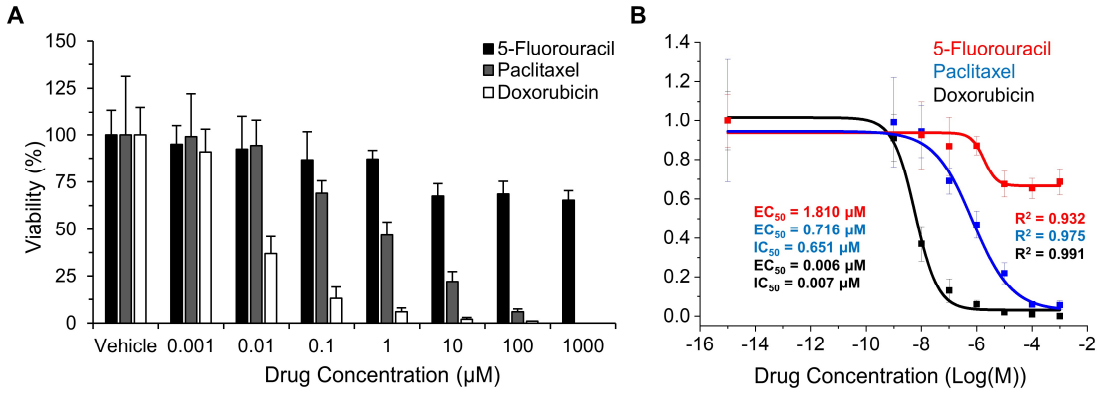

Figure 4.1: Response of MDA-MB-231s Cultured on Tissue Culture Plastic (2D) to 5-Fluorouracil, Paclitaxel, and Doxorubicin. (A) Quantification of MDA-MB-231 cell viability cultured on tissue culture plastic (2D) after 48 h drug exposure. n=6 images from 6 individual wells. Values represent mean ± standard deviation. (B) Dose-response curves for doxorubicin, paclitaxel, and 5-fluorouracil with EC_{50} and IC_{50} values. Data points represent mean ± standard deviation. *Figure obtained from [45] with permission from ACS Publications.*

As expected, 231s demonstrated significant decreases in cell viability with increased drug concentration for all three drugs tested. DOX was the most effective, followed by PAC, and 5-FU (Figure 4.1). The results demonstrate that viability decreased to 37 ± 9% at 0.01 μM before gradually dropping to 1 ± 0% at 100 μM for DOX (Figure 4.1). Fitting the dose-response curve for DOX resulted in an EC_{50} of 0.006 μM and IC_{50} of 0.007 μM (Figure 4.1B). PAC was less effective than DOX. At 0.01 μM, viability remained high at 94 ± 13%, but decreased to 6 ± 2% at the highest concentration tested (100 μM) (Figure 4.1A. Calculated EC_{50} (0.716 μM) and IC_{50} (0.651 μM) values were higher for PAC compared to DOX (Figure 4.1B). 5-FU was the least effective with an EC_{50} of 1.81 μM and with 65 ± 3% of the cell population viable at the highest dosage of 1 mM (Figure 4.1). An IC_{50} could not be calculated for 5-FU, as viability did not drop below 65% (Figure 4.1B).

4.3.2 Response of MDA-MB-231s to Paclitaxel

It is well established that dormant cells often display increased chemoresistance.[18-20] To quantify the degree of chemoresistance imparted on parental 231s in dormant states compared to the growth state, the response of parental 231s cultured in the three hydrogel formulations (permissive gel 1, non-permissive gel 2, and non-permissive gel 3) to PAC was quantified. Post encapsulation, the cells were cultured for 15 days in the desired hydrogel formulation to provide enough time for the cells to respond to the hydrogel properties; culturing for longer time periods did not significantly alter phenotype.[34-36] Cells were exposed to varying concentrations of PAC for 48 h (0.05-1 mM) and cell viability was quantified (Figure 4.2).[108] To assess the drug-response of 231s in the three phenotypic states, the cells were labeled with Calcein AM to fluorescently label live cells, imaged (Figure 4.2A), and the number of live cells normalized to the vehicle control (media containing 1% DMSO) to quantify cell viability (Figure 4.2B).

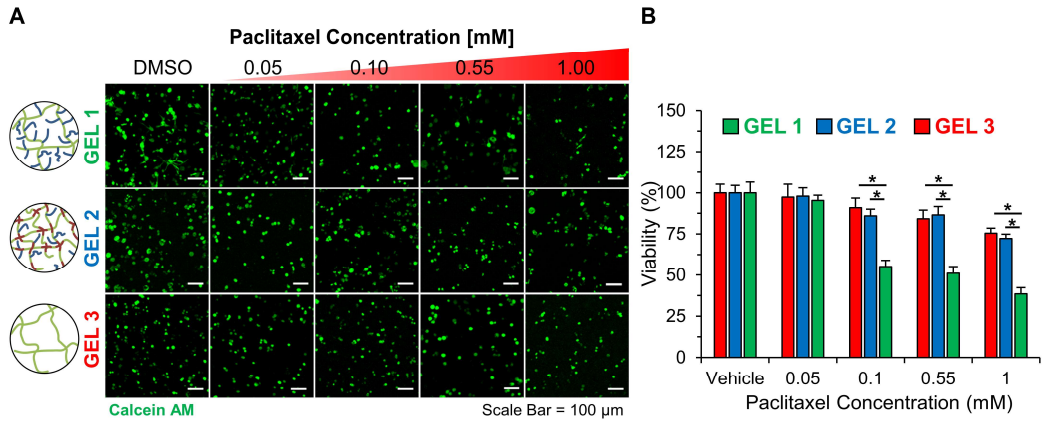

Figure 4.2: Chemosensitivity to Paclitaxel. (A) Representative maximum intensity z-projections of 3D image stacks of MDA-MB-231s fluorescently labeled with Calcein AM (live cells:green) after 48 h exposure to a media + 1% v/v DMSO vehicle control (DMSO) or varying concentrations of paclitaxel. Top row: growth (permissive gel 1); middle row: tumor mass dormancy (non-permissive gel 2); bottom row: restricted survival dormancy (non-permissive gel 3). Scale bar = 100 µm. (B) Quantification of cell viability. * indicates statistically significant difference ($p<0.05$). n=5 z-stacks from 5 individual hydrogels. Values represent mean + standard deviation. *Figure adapted from [53] with permission from ACS Publications.*

Results showed that parental 231s undergoing restricted survival cellular dormancy (in non-permissive gel 3) had statistically significant higher viability for most PAC concentrations compared to parental 231s in the growth state. For instance, at 0.10 and 0.55 mM, parental 231s in non-permissive gel 3 remained 91 ± 6% and 84 ± 5% viable compared to 55 ± 4% and 51 ± 4% for cells in the growth state respectively, compared to their respective DMSO control conditions (Figure 4.2B). Furthermore, at the highest PAC concentration tested (1 mM), 75 ± 3% of dormant cells in non-permissive gel 3 remained viable while only 39 ± 4% of parental 231s in the growth state were viable (Figure 4.2B). Parental 231s in balanced cellular

dormancy (non-permissive gel 2) also exhibited significant chemoresistance to PAC. For example, at 0.55 mM and 1.00 mM, viability was 86 ± 5% and 72 ± 3% for cells non-permissive gel 2, and 51 ± 4% and 39 ± 4% for growing cells in permissive gel 1 respectively. There were no statistically significant differences in viability between the two dormant states for any concentration of PAC tested (Figure 4.2B).

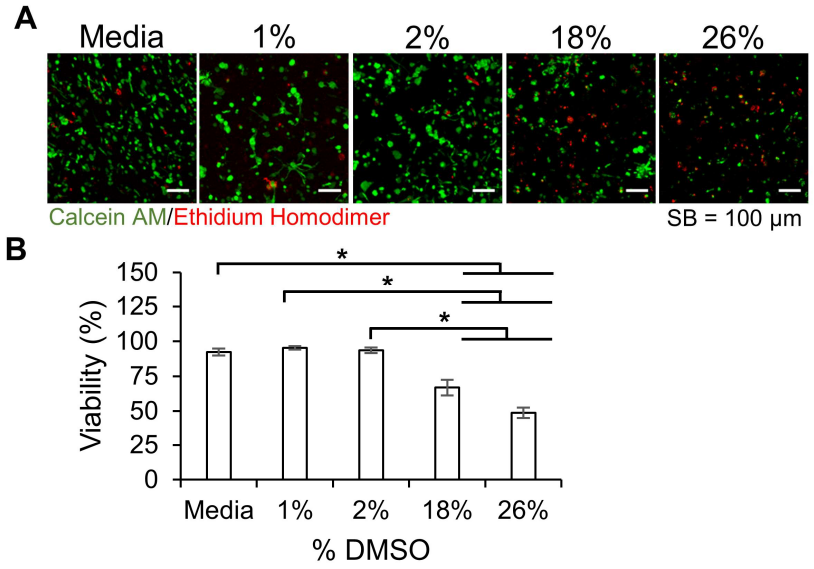

Figure 4.3: Influence of DMSO on Cell Viability for Cells Cultured in a Growth Hydrogel Formulation. (A) Representative maximum intensity z-projections of 3D image stacks of encapsulated MDA-MB-231s after 48 h exposure to varying concentrations (% v/v) of DMSO in serum-containing medium. Live cells are labeled with Calcein AM (green). Dead cells are labeled with Ethidium homodimer (red). SB=100 µm. (B) Quantification of cell viability. * indicates $p<0.05$. n=5 z-stacks from 5 individual hydrogels. Values represent mean ± standard deviation. *Figure adapted from [45] with permission from ACS Publications.*

PAC was dissolved in minimal DMSO according to its solubility and manufacturer's instructions. Due to the upper limits of PAC efficacy, we were unable

to test higher drug doses, as higher doses would exceed the concentration of DMSO that the parental 231s could tolerate and thus would no longer represent cells targeted by the mechanism of the drug but instead by the DMSO itself (Figure 4.3). For this reason, we were unable to fit a dose-response curve to this data. However, viability data demonstrates that cells in both dormant states showed significant chemoresistance to PAC.

4.3.3 Response of MDA-MB-231s to 5-Fluorouracil

To determine if dormant-cell chemoresistance was also observed in other chemotherapeutics, we investigated the effect of a second, commonly used breast cancer drug, 5-FU on parental 231s in the three phenotypic states. The same protocol was followed to encapsulate, label, image, and quantify live cells. Compared to PAC, the 2D studies indicated that 5-FU was the least effective and therefore required higher dose concentrations (Figure 4.4A,B), which was also limited by DMSO toxicity as discussed. Nonetheless, a significant increase in chemoresistance was observed for dormant parental 231s in non-permissive gels 2 and 3, compared to growing cells in permissive gel 1 (Figure 4.4A,B).

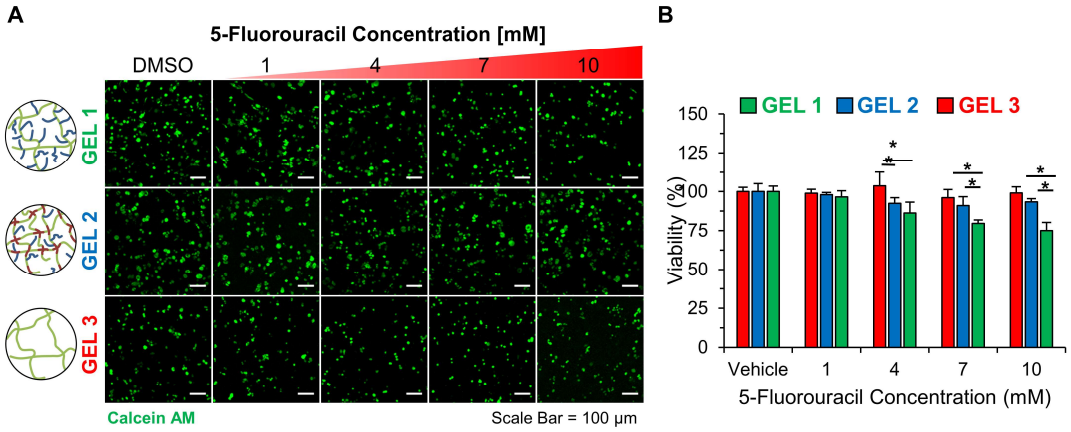

Figure 4.4: Chemosensitivity to 5-Fluorouracil. (A) Representative maximum intensity z-projections of 3D image stacks of MDA-MB-231s fluorescently labeled with Calcein AM (live cells:green) after 48 h exposure to a media + 1% v/v DMSO vehicle control (DMSO) or varying concentrations of 5-Fluorouracil. Top row: growth (permissive gel 1); middle row: tumor mass dormancy (non-permissive gel 2); bottom row: restricted survival dormancy (non-permissive gel 3). Scale bar = 100 µm. (B) Quantification of cell viability. * indicates statistically significant difference ($p<0.05$). n=5 z-stacks from 5 individual hydrogels. Values represent mean + standard deviation. *Figure adapted from [45] with permission from ACS Publications.*

At 1 mM, parental 231s remained highly viable in all three hydrogel formulations. However, at 4 mM, growing 231s in permissive gel 1 decreased to 86 ± 7% viability while those undergoing restricted survival cellular dormancy in non-permissive gel 3 remained 100 ± 6 % viable and 231s undergoing balanced cellular dormancy in non-permissive gel 2 displayed 92 ± 4% viability, compared to their respective DMSO control conditions (Figure 4.4B). A similar trend was observed at 7 mM, with growing 231s in permissive gel 1 further decreasing to 80 ± 2% viability while cells in both dormant states remained >90% viable (Figure 4.4B). At the highest concentration tested (10 mM), dormant 231s undergoing in non-permissive gel 3 were

99 ± 4% viable compared to only 75 ± 5% for those in the growth state (Figure 4.4B). No statistically significant differences were measured between 231s in either dormant state (Figure 4.4B). These results indicate that dormant parental 231s remain >90% viable at all concentrations of 5-FU tested and display greater chemoresistance to 5-FU than parental 231s in the growth state (Figure 4.4B).

4.3.4 Response to Doxorubicin

A third chemotherapeutic, DOX was also implemented to assess dormant cell chemoresistance. Based on the 2D studies, DOX had the greatest overall efficacy, therefore DOX studies were performed on growing and dormant parental 231s, as well as reactivated 231s to determine if reactivated cells had similar sensitivity to growing cells in permissive gel 1. Furthermore, this study was also performed on the other cell lines shown to enter growth, dormancy, and reactivation in chapter 3: 231-derived organotropic sublines with preferential metastasis to bone (BoM-1833)[38], lung (LM2-4175)[39], or brain (BrM2a-831)[40] and ER^+ MCF7s.

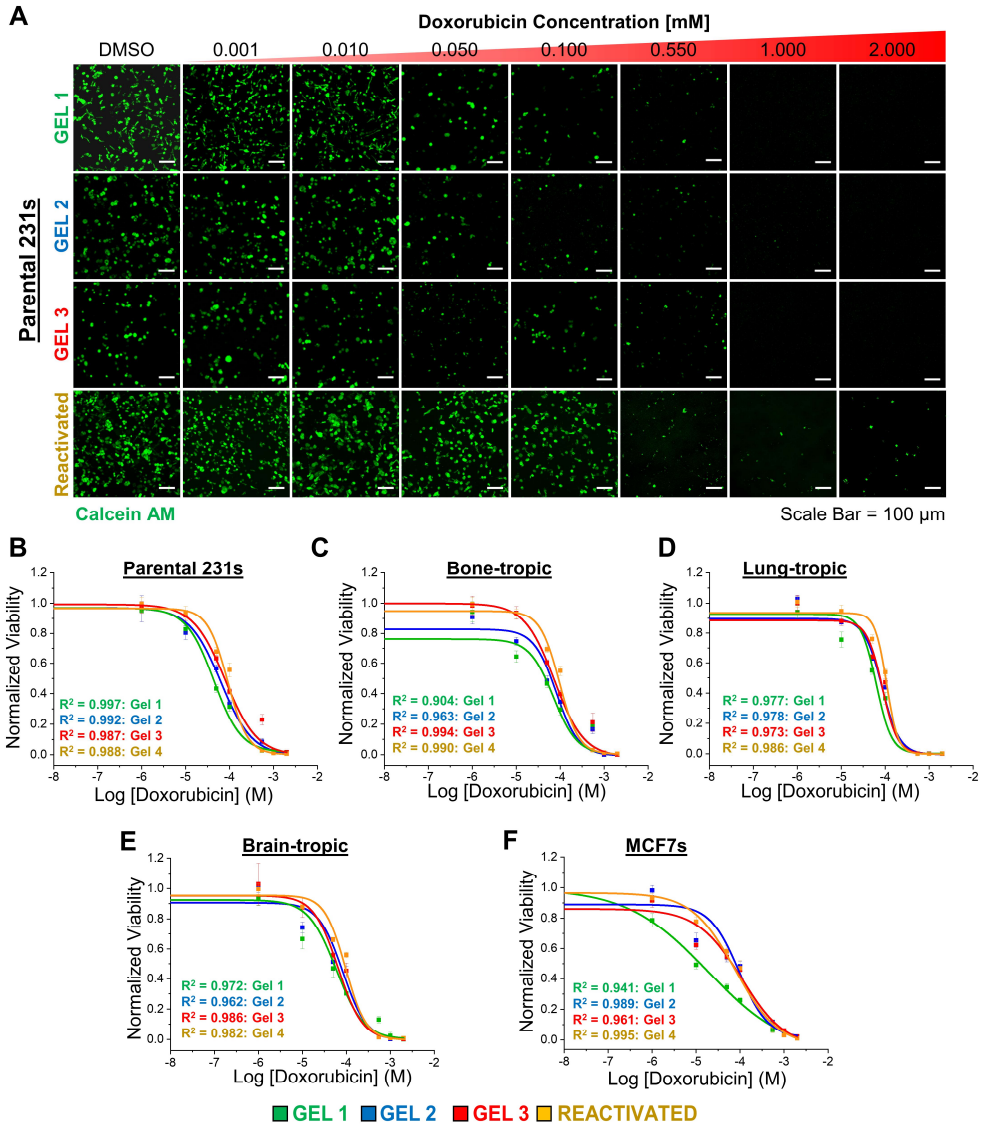

Figure 4.5: Chemosensitivity to Doxorubicin. (A) Representative maximum intensity z-projections from 3D image stacks of live (Calcein AM:green) MDA-MB-231s (parental 231s) after 15 days in culture followed by 48 h exposure to doxorubicin at the indicated concentration. Scale bar = 100 µm. Dose-response curves for (B) parental 231s and (C) BoM-1833s (bone-tropic), (D) LM2-4175s (lung-tropic), (E) BrM2-831s (brain-tropic), and (F) MCF7s. * indicates statistically significant difference ($p<0.05$). n=6 z-stacks from 6 individual hydrogels. Values represent mean ± standard deviation. *Figure adapted from [41] with permission from John Wiley and Sons.*

Cells were cultured in each formulation for 15 days to achieve growth or dormancy. In reactivated cases, dormant cells grown for 15 days were cultured an additional 7 days after PEG-RGDS incorporation. Cell-laden hydrogels were then exposed to varying concentrations of DOX for 48 h, labeled for viability, imaged, and quantified (Figure 4.5).

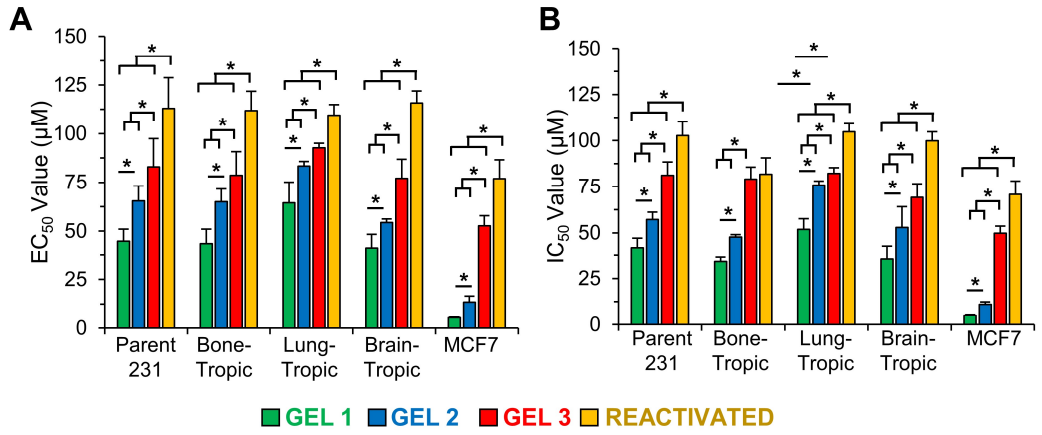

Figure 4.6: Doxorubicin EC_{50} and IC_{50} Values. (A) EC_{50} and (B) IC_{50} values for MDA-MB-231s (parental), BoM-1833s (bone-tropic), LM2-4175s (lung-tropic), BrM2-831s (brain-tropic) sublines, and MCF7s. * indicates statistically significant difference ($p<0.05$). n=6 z-stacks from 6 individual hydrogels. Values represent mean + standard deviation. *Figure adapted from [41] with permission from John Wiley and Sons.*

Overall, dormant populations exhibited increased chemoresistance to DOX compared to growing populations. For instance, at 0.01 and 0.05 mM, viability remained 91 ± 2% and 62 ± 5% for dormant parental 231s in non-permissive gel 3 and 82 ± 1% and 44 ± 3% for growing cells in permissive gel 1 respectively, compared to their respective DMSO control conditions (Figure 4.5). Increased differences in

viability were observed at higher concentrations (0.55, 1.00 mM) where viability was 4-6 times higher for dormant parental 231s compared to those in the growth state (Figure 4.5). Parental 231s undergoing balanced dormancy in non-permissive gel 2 also displayed higher viability compared to parental 231s in permissive gel 1 over a range of concentrations, with significant differences observed at 0.05 mM and 0.55 mM (Figure 4.5).

Dose response curves were fit to the viability data for the growth and two dormant states to quantify EC_{50} and IC_{50} values (Figure 4.5, 4.6), in which higher concentrations indicate that more of a drug is required to produce the same effect, and therefore indicates increased chemoresistance. Results confirmed that dormant cells had increased chemoresistance to DOX for all five cell lines (Figure 4.5, 4.6). These findings were expected as DOX targets actively proliferating cells and dormant cells in non-permissive gels 2 and 3 have low proliferation levels. However, we also found that reactivated cells (with higher proliferation levels similar to permissive gel 1) also maintained a similar, and in most cases significantly greater, chemoresistance to DOX. For instance, growing parental 231s in permissive gel 1 had an EC_{50} value of 44.9 ± 6.2 μM, while dormant parental 231s in non-permissive gels 2 and 3 had significantly greater EC_{50} values of 65.5 ± 7.7 μM (gel 2) and 82.9 ± 14.5 μM (gel 3) (Figure 4.5, 4.6). Interestingly, reactivated parental 231s had an EC_{50} of 113.0 ± 15.7 μM, which was significantly greater than both growing (~2.5-fold increase) and dormant (~1.4-1.7-fold increase) cells. This suggests that other mechanisms may be involved in observed chemoresistance.

Both organotropic 231s and MCF7s showed similar trends with significantly greater EC_{50} values for dormant cells in non-permissive gels 2 and 3 compared to

growing cells in permissive gel 1, and significantly greater EC_{50} values for reactivated cells: bone (permissive gel 1: 43.6 ± 7.5 μM, non-permissive gel 2: 65.0 ± 6.5 μM, non-permissive gel 3: 78.5 ± 12.3 μM, reactivated: 111.9 ± 9.8 μM), lung (permissive gel 1: 64.5 ± 10.5 μM, non-permissive gel 2: 83.3 ± 2.4 μM, non-permissive gel 3: 92.7 ± 2.4 μM, reactivated: 109.4 ± 5.5 μM), brain (permissive gel 1: 41.4 ± 6.9 μM, non-permissive gel 2: 54.4 ± 1.9 μM, non-permissive gel 3: 77.1 ± 9.8 μM, reactivated: 115.8 ± 6.2 μM), MCF7s (permissive gel 1: 5.3 ± 0.5 μM, non-permissive gel 2: 13.5 ± 3.1 μM, non-permissive gel 3: 52.7 ± 5.2 μM, reactivated: 76.9 ± 9.7 μM). IC_{50} values showed similar trends (Figure 4.5, 4.6).

This data confirms that both dormant and reactivated cells in this platform exhibit increased chemoresistance. Since this was observed for triple negative parental 231s, derived organotropic sublines, and ER^+ MCF7s, it is likely that this increased resistance is not cell-type dependent. Furthermore, this data also suggests that while reactivated cells have similar proliferation and viability values to growing cells in permissive gel 1, reactivated cells have unique characteristics likely due to their transition into dormancy, or their exit from dormancy and into reactivated growth.

4.3.5 Doxorubicin Intracellular Accumulation

To determine the cause of increased chemoresistance to DOX displayed by dormant and reactivated parental 231s, organotropic sublines, and MCF7s compared to those in the growth state, we took advantage of DOX autofluorescence[104,105] to quantify intracellular drug accumulation over time[109-111] (Figure 4.7A,B). After 15 (gel 1, 2, 3) or 22 days (reactivated) in culture, cells were exposed to 0.05 mM DOX for 48 h. Cell-laden hydrogels were imaged throughout the 48 h at varying time points (1, 2, 3, 4, 5, 6, 12, 24, 36, 48 h). Mean fluorescence intensity was measured to determine

DOX accumulation at each time point (Figure 4.7). From this data, we obtained DOX intensity over time which was used to calculate accumulation rate (the slope of the linear region (between 0 to 6 h)). Note, while 231s in the growth formulation appear invasive after 15 days in culture, they revert to a rounded morphology after 48 h DOX exposure.

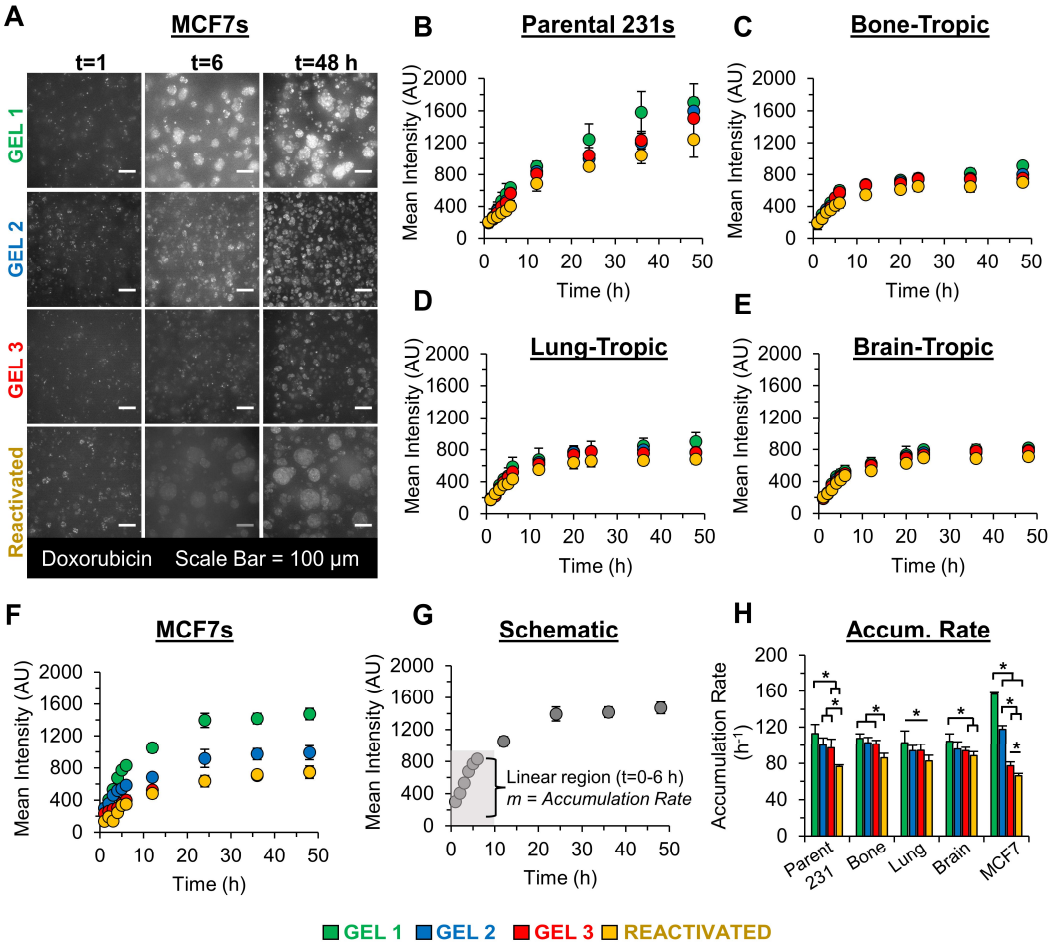

Figure 4.7: Doxorubicin Intracellular Accumulation. (A) Representative sum intensity z-projections from 3D image stacks of 0.05 mM doxorubicin in MCF7s after 1, 6, and 48 h. Scale bar = 100 µm. Quantification of doxorubicin (0.05 mM) accumulation in (B) MDA-MB-231s (parental 231s), (C) BoM-1833s (bone-tropic), (D) LM2-4175s (lung-tropic), (E) BrM2-831s (brain-tropic) sublines, and (F) MCF7s over 48 h via fluorescence intensity. (G) Schematic indicating how accumulation rate was determined (the slope of the linear portion (0-6 h) from each accumulation graph). (H) Doxorubicin accumulation rate. * indicates statistically significant difference ($p<0.05$). n=6 z-stacks from 6 individual hydrogels. Values represent mean ± standard deviation.

In the parental 231 line, results indicated that DOX accumulated at a greater rate in growing cells in permissive gel 1 (accumulation rate: 112.8 ± 10.1 h^{-1}), compared to dormant (100.5 ± 7.7 h^{-1} (non-permissive gel 2), 97.2 ± 9.4 h^{-1} (non-permissive gel 3) or reactivated cells (76.6 ± 1.7 h^{-1}) (Figure 4.7H). Consistent with chemoresistance results, accumulation rate in reactivated parental 231s was significantly lower than in dormant or growing cells.

Organotropic sublines had varying results depending on cell line. In bone-tropic 231s, there was no significant difference in accumulation between dormant and growing cells, however, DOX did accumulate at a significantly lower rate in reactivated cells compared to both growing and dormant states (permissive gel 1: 107.6 ± 4.9 h^{-1}, non-permissive gel 2: 102.6 ± 5.9 h^{-1}, non-permissive gel 3: 101.4 ± 4.0 h^{-1}, reactivated: 86.03 ± 5.2 h^{-1}) (Figure 4.7H). In lung-tropic 231s, there was only a significant difference in accumulation rate between growing cells in permissive gel 1 and reactivated cells, with no significant difference between dormant and reactivated states (permissive gel 1: 102.6 ± 13.1 h^{-1}, non-permissive gel 2: 94.0 ± 5.8 h^{-1}, non-permissive gel 3: 94.3 ± 6.7 h^{-1}, reactivated: 82.6 ± 6.4 h^{-1}) (Figure 4.7H). Growing brain-tropic 231s in permissive gel 1 had a significantly greater accumulation rate than dormant cells in non-permissive gel 3 and reactivated cells (permissive gel 1: 104.5 ± 8.1 h^{-1}, non-permissive gel 2: 95.8 ± 8.05 h^{-1}, non-permissive gel 3: 94.0 ± 3.6 h^{-1}, reactivated: 88.4 ± 4.5 h^{-1}).

Finally, MCF7s showed the greatest differences in accumulation rate with significant differences observed between each phenotypic state with the greatest accumulation rate observed in permissive gel 1 (156.5 ± 1.7 h^{-1}), followed by dormant cells in non-permissive gel 2 (117.5 ± 4.0 h^{-1}), dormant cells in non-permissive gel 3

($77.2 \pm 4.5\ h^{-1}$), and reactivated cells ($66.3 \pm 2.5\ h^{-1}$)(Figure 4.6H). Overall, results show DOX accumulates at greater rate in chemosensitive, growing cells compared to more chemoresistant dormant and reactivated cells.

4.3.6 Doxorubicin Intracellular Localization

Once we determined that DOX accumulation varied between formulations and phenotypic state, we aimed to quantify potential differences in the intracellular distribution. To measure DOX localization, cells were cultured for 15 (gel 1, 2, 3) or 22 days (reactivated), and exposed to 0.05 mM DOX for 48 h. The cells were counterstained to visualize the nucleus and imaged. To calculate nuclear: cytoplasmic (NC) ratio, fluorescence intensity measurements of the cytoplasm and nuclei were made and compared.

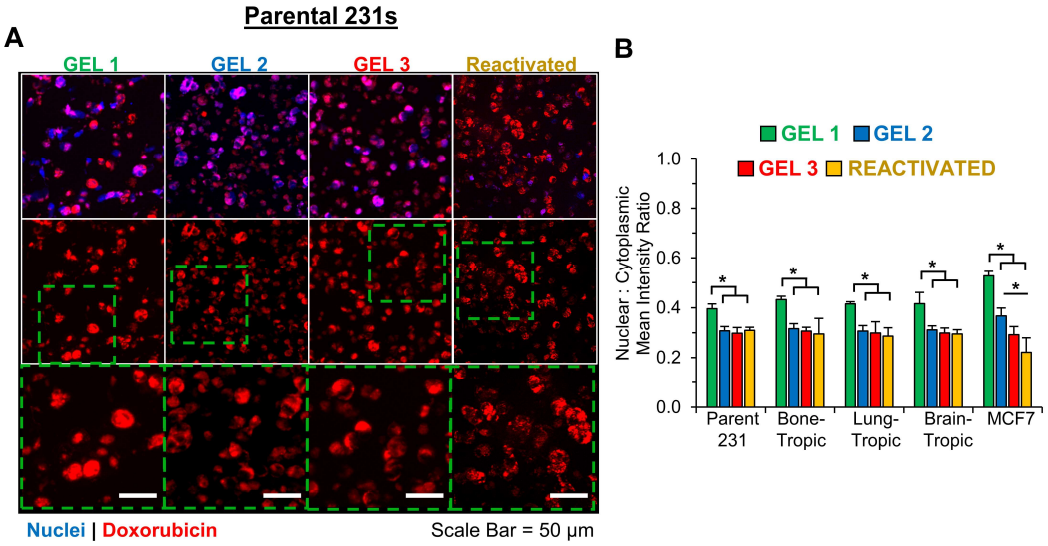

Figure 4.8: Doxorubicin Nuclear and Cytoplasmic Localization. (A) Representative sum intensity z-projections from 3D image stacks of doxorubicin (0.05 mM) in MDA-MB-231s (parental 231s) after 48 h (nuclei: blue, doxorubicin: red). Scale bar = 50 µm. (B) Quantification of nuclear to cytoplasmic localization of doxorubicin (0.05 mM, 48h) in MDA-MB-231s (parent 231), BoM-1833s (bone-tropic), LM2-4175s (lung-tropic), BrM2a-831s (brain-tropic), and MCF7s cell lines using intensity measurements of the cell cytoplasm and nucleus. * indicates $p < 0.05$ determined by a one-way ANOVA. n = 4 z-stacks from four individual hydrogels. Values represent mean + standard deviation.

Results showed that across all cell lines, there was significantly greater DOX localization in the nuclei of growing cells in permissive gel 1 compared to dormant or reactivated cells (Figure 4.8). For instance, parental 231s had an NC ratio of 0.40 ± 0.02 in growing cells (permissive gel 1), 0.31 ± 0.02 (non-permissive gel 2) or 0.30 ± 0.02 (non-permissive gel 3) in dormant cells, and 0.31 ± 0.01 in reactivated cells (Figure 4.8B). Organotropic sublines showed similar trends: bone ((growing) permissive gel 1: 0.43 ± 0.01, (dormant) non-permissive gel 2: 0.32 ± 0.02, (dormant) non-permissive gel 3: 0.31 ± 0.02, reactivated: 0.29 ± 0.06), lung ((growing)

permissive gel 1: 0.41 ± 0.01, (dormant) non-permissive gel 2: 0.31 ± 0.02, (dormant) non-permissive gel 3: 0.30 ± 0.05, reactivated: 0.29 ± 0.03), brain ((growing) permissive gel 1: 0.42 ± 0.05, (dormant) non-permissive gel 2: 0.31 ± 0.02, (dormant) non-permissive gel 3: 0.30 ± 0.02, reactivated: 0.29 ± 0.02 (Figure 4.8B). In MCF7s, growing cells in permissive gel 1 (0.53 ± 0.02) also had significantly greater nuclear localization than dormant (non-permissive gel 2: 0.37 ± 0.03, non-permissive gel 3: 0.29 ± 0.03) and reactivated cells (0.22 ± 0.06)(Figure 4.8B). Additionally, there was significantly greater nuclear localization in dormant MCF7s in non-permissive gel 2 compared to reactivated cells.

Overall, results show that along with increased accumulation, growing cells in permissive gel 1 have greater nuclear localization. Since DOX induces DNA damage and cell death via methods including intercalation into DNA, this data suggests there is more DNA-bound DOX in 231s in the growth state compared to those undergoing dormancy or reactivation. This suggests that the chemoresistance displayed by dormant and reactivated cells may be due to decreased DOX accumulation and nuclear localization.

4.4 Discussion and Conclusion

An important step toward preventing and treating cancer metastasis and recurrence includes forming a better understanding of the various factors that induce and mediate cancer latency and dormancy and mechanisms of chemoresistance imparted on dormant cells. A significant roadblock in preventing cancer metastasis is that many current chemotherapeutics fail to effectively treat dormant cells. In chapters 2 and 3, we developed and implemented three hydrogel formulations that induced distinct phenotypic states (growth, balanced tumor mass dormancy, balanced cellular

dormancy, and restricted survival cellular dormancy) in triple negative breast cancer cells, parental 231s and 231-derived organotropic lines, and ER^+ breast cancer cells, MCF7s, by altering cell-matrix interactions.[34-36,41] Here, we implemented these engineered hydrogels to quantify the drug response of dormant cells to commonly used chemotherapeutics.[45] While other methods can be used to induce dormancy in cancer cells, this study particularly focuses on hydrogel induced dormancy.

Control studies were performed in 2D to assess parental 231 drug response to DOX, PAC, and 5-FU (Figure 4.1). Following the same protocol used for encapsulation, parental 231s were cultured, serum starved for 48 h, and exposed to common breast cancer drugs, DOX, PAC, or 5-FU for 48 h. Viability data demonstrates IC_{50} values of 0.007 and 0.651 μM for DOX and PAC respectively and EC_{50} values of 0.006, 0.761, and 1.810 μM for DOX, PAC, and 5-FU respectively (Figure 4.4, 4.5) which are comparable to previously reported values from 2D studies.[112-114]

For 3D studies, parental 231s were cultured for 15 (gel 1, 2, 3) or 22 (reactivated) days and then exposed to DOX, PAC, or 5-FU, for 48 h.[108] Viability assays were conducted to quantify the response to each drug. As expected, parental 231s in 3D were less sensitive to drugs compared to 2D culture. Differences between 2D and 3D systems in the context of drug screening have previously been reviewed[115] and it is accepted that 3D drug platforms better represent drug responses observed *in vivo*.[115,116] Cells may respond differently to drugs in 3D due to oxygen gradients similar to those in *in vivo* tumors, spatial organization of cell surface receptors, matrix diffusion, and physical constraints that influence gene expression.[116] Differences in our system may be do physical constraints imparted by the matrix and spatial

organization of encapsulated cells. However, we do not expect there to be oxygen gradients or transport limitations since hydrogels are only 500 μm in thickness, which is below the distance range necessary to form these gradients. Additionally, we expect no limitations in drug transport as drugs used in these studies are small molecules with molecular weights ranging from 130 to 854 g/mol. For instance, DOX was estimated to be <2 nm in diameter using a molecular model.[117] Additionally, molecules of similar molecular weights do not exceed 2 nm in size.[118] The average mesh size of the hydrogels, without NVP (permissive gel 1, and non-permissive gel 3) and with NVP (non-permissive gel 2) was 69 ± 5 nm and 55 ± 4 nm respectively. Since the drugs used here were an order of magnitude smaller than the hydrogel mesh size, we anticipate high levels of diffusion throughout the hydrogel.

Changes in drug response were also observed between parental 231s undergoing growth, balanced cellular dormancy, and restricted survival dormancy. In both PAC and 5-FU, dormant parental 231s in either state had significantly higher viability than those in the growth state. PAC and 5-FU were less effective in reducing cell viability and therefore required higher concentrations (Figure 4.1-4.4). Even though all drugs tested were dissolved in minimal DMSO according to solubility, we were unable to test higher drug doses as higher doses would lead to cytotoxic effects from DMSO alone and would confound interpretation of the results. Therefore, we were not able to generate a dose-response curve for these drugs, however, the viability data demonstrates that parental 231s in either dormant state showed significant chemoresistance to PAC and 5-FU.

Since DOX had higher efficacy, shown by 2D studies, we investigated DOX chemosensitivity in growing (permissive gel 1), dormant (non-permissive gels 2 and

3), and reactivated parental 231s, as well as 231-derived organotropic lines, and MCF7s. Dose-response curves demonstrated that cells undergoing either form of dormancy had significantly greater EC_{50} and IC_{50} values compared to growing cells, for all five cell lines. This indicates that a higher dosage of DOX is required to induce 50% death in dormant cells compared to actively proliferating cells. Furthermore, reactivated cells had even greater EC_{50} values than both dormant and growing cells for all 5 cell lines tested. While our IC_{50} and EC_{50} values fall within the range of other 3D DOX studies, it is worth noting that current IC_{50} and EC_{50} values reported in 3D drug studies vary significantly in magnitude, due to differences in key factors including matrix properties, experimental duration, and cell growth rates.[35] Overall, these results agree with current data that indicates dormant cells show increased chemoresistance *in vivo* and *in vitro*.[15,16,18-20,31] This data also serves to further validate the ability to induce dormant states using engineered hydrogels composed of simple components as demonstrated here.

All drugs used in these studies target proliferating cells through various mechanisms. DOX interferes with cell cycle progression by preventing DNA replication via intercalation and inhibition of topoisomerase II. Additionally, DOX can be oxidized to a semiquinone radical, that can generate reactive oxygen species causing DNA damage.[119] PAC disrupts proliferating cells by preventing microtubule disassembly during mitosis. 5-FU inhibits RNA transcription and interferes with DNA synthesis.[108,120] Cells unable to proliferate due to DNA damage will activate apoptotic mechanisms during cell cycle check points.[121] Furthermore, cancer cells often have inhibited or deficient repair mechanisms that prevent them from repairing damaged DNA.[122] According to the fractional kill theory, a drug will only eliminate those cells

that pass through the relevant cell cycle phase during drug exposure.[121,123] Positive correlations between clinical response of DNA-targeted chemotherapy and rate of proliferation support this theory.[121,124] Thus, DOX, and other cancer drugs, preferentially target proliferating cells and may even kill rapidly dividing cells that are not cancerous such as blood cells in the bone marrow. Therefore, dormant cells in a quiescent state (G_0-G_1 arrest) that are slow cycling, such as those in this study, would not be susceptible to drug-induced death for drugs that target cell division.[18,121] Dormancy-associated resistance is supported by multiple patient studies that indicate dormant DTCs are resistant to common forms of chemotherapy.[15-20] Interestingly, reactivated cells that have proliferation levels similar to chemosensitive growing cells in permissive gel 1 showed significant chemoresistance exceeding that of growing and dormant cells, suggesting that DOX chemoresistance may be due to other mechanisms aside from proliferation levels, including unique gene expression or chemoresistant-associated proteins (further explored in chapter 5).

Studies that quantify DOX accumulation and localization have been used to understand chemoresistance mechanisms. To test if drugs accumulated differently in dormant and reactivated cells compared to those in the growth state, DOX autofluorescence[105-107] was implemented to quantify drug accumulation rate[109-111] by temporally measuring the intracellular fluorescence intensity (concentration) of DOX over 48 h. The results indicated significant differences in intracellular accumulation rate, with significantly lower accumulation rates in chemoresistant dormant and reactivated cells in all 5 cell lines. These results indicate that drug accumulation (difference in uptake and efflux)[125] was greater in growing cells in permissive gel 1. This suggests that dormant and reactivated 231s may use efflux pumps that actively

expel DOX out of the cell, similar to known chemoresistant cells. This theory is further explored in chapter 5.[125,126] Overall, this data indicates drug accumulation may play a role in dormant and reactivated cell chemoresistance, at least for DOX.

While drug accumulation can indicate if DOX made it into a cell, translocation into the nucleus better indicates its chemotherapeutic effect since DOX works by intercalating into DNA.[126] To measure this, we calculated the NC ratio by measuring the DOX fluorescence intensity in the nucleus and cytoplasm of each cell using a nuclear co-stain (Figure 4.7).[125-127] Data showed that dormant and reactivated cells had significantly lower NC ratios, compared to growing cells in permissive gel 1 across all 5 cell lines. This data suggests DOX accumulation along with distribution within the cell leads to a difference in chemotherapeutic response.

As it is also well-established that dormant DTCs in secondary organs often display enhanced chemoresistance,[17-20,101,102] the work presented here further validates that our simple hydrogel platform can be used to induce dormant and reactivated states in metastatic breast cancer with increased chemoresistance. Such a platform potentially provides the ability to better understand how dormancy is initiated, the mechanisms of chemoresistance used by dormant cells, and the ability to screen new therapeutics. While a multitude of factors can induce dormancy, this platform focuses solely on the influence of matrix properties with respect to ligand density and degradability. While the influence of other dormancy inducing factors including immune responses, hypoxia, nutrient deprivation, soluble factors, and secondary cell signaling were excluded in this study they could potentially be included in future studies although additional complexity needs to be carried out in a well-controlled, well-characterized, and thorough manner to understand their synergistic roles in

influencing the observed cancer cell response. Similarly, although we focused exclusively on breast cancer, we speculate that other cancers could be induced to undergo dormancy, which could be tested in future studies.

Overall, this study builds on the characterization of our hydrogel platform (chapter 2), and its ability to induce growth, distinct forms of dormancy, and reactivation (chapter 3) to quantify chemosensitivity and provide valuable insight into the mechanisms involved in dormancy-associated chemoresistance, aiding in the ultimate goal to find novel ways to target and eliminate dormant cells to prevent metastatic relapse.

Chapter 5

EFFLUX PUMPS IN DORMANT AND REACTIVATED CELL CHEMORESISTANCE

Sections in this chapter have been adapted from the following articles:

(1) Farino CJ, Pradhan S, Slater JH. The Influence of Matrix-Induced Dormancy on Metastatic Breast Cancer Chemoresistance. ACS Applied Biomaterials 2020, 3(9), 5832-5844.

(2) Farino Reyes CJ, Pradhan S, Slater JH. The Influence of Ligand Density and Degradability on Hydrogel Induced Breast Cancer Dormancy and Reactivation. Advanced Healthcare Materials 2021, 10(11), 2002227.

5.1 Introduction

It is well-established that metastases originating from many types of primary cancer (breast, lung, prostate, etc.) undergo periods of latency or dormancy and whose length depends on a multitude of factors including origin, receptor status, and microenvironmental properties of the secondary organ infiltrated.[4,7] It is also well-established that dormant DTCs in secondary organs often display enhanced chemoresistance.[15-20] Since metastasis is one of the leading causes of cancer-associated morbidity and mortality there is an urgent need for simple platforms that allow for thorough investigations of how dormancy is induced and maintained. Such platforms could be beneficial in developing and testing new therapeutic strategies targeted at eliminating dormant cancer cells or preventing cells from escaping dormancy.[3,4,108] Although tumor dormancy can be induced in animal models and

dormant cells isolated,[128,129] implementation of these models for drug discovery can be cumbersome due to the difficulty in monitoring their response over time due to resolution limitations of current *in vivo* imaging modalities. Accordingly, *in vitro* platforms could potentially accelerate therapeutic development assuming that the cellular responses induced by these platforms are biomimetic enough to recapitulate important aspects of what occurs *in vivo*.

Toward this goal, we demonstrated the ability to induce growth, distinct forms of dormancy and reactivation in the triple negative parental 231s, organotropic sublines (BoM-1833s (bone-tropic), LM2-4175s (lung-tropic), BrM2a-831s (brain-tropic), and ER^+ MCF7s by tuning matrix adhesivity (via RGDS) and degradability (via NVP) in chapters 2 and 3. "On-demand" reactivation for all 5 cell lines was also achieved via RGDS incorporation which effectively converted non-permissive gel 3 into permissive gel 1. Once a dormancy and reactivation system were established, this platform was implemented to quantify dormant and reactivated cell chemoresistance in chapter 4. Findings indicated that both dormant (in non-permissive gels 2 and 3) and reactivated cells exhibited increased chemoresistance to DOX, indicated by significantly greater EC_{50} and IC_{50} values than corresponding growing cells in permissive gel 1. Insight into this chemoresistance was provided by results that showed DOX accumulated at a significantly lower rate in chemoresistant dormant (in non-permissive gels 2 and 3) and reactivated cells. Furthermore, once in the cell, DOX nuclear localization was significantly decreased in chemoresistant cells, compared to chemosensitive cells in permissive gel 1, indicated by the NC ratio. This data suggests that dormant (in non-permissive gels 2 and 3) and reactivated cells attain increased chemoresistance via reduced DOX accumulation and nuclear localization. With the

ultimate goal of finding new therapeutic strategies to target and eliminate dormant cells, this chapter sought to expand on these findings by investigating what drives these differential levels of DOX transport into and within the cell.

Cancer chemoresistance involves a myriad of mechanisms depending on multiple factors. Some of the most commonly studied mechanisms include transporter pumps, tumor suppressor genes, oncogenes, autophagy, mitochondrial alteration, epithelial-mesenchymal transition (EMT), cancer stemness, and others.[130] Many of these mechanisms work in conjunction to decrease drug toxicity, including EMT-related stemness and oncogenes that modulate apoptosis-related genes.[130] This study focused on transport pumps, as previous results confirmed that DOX intake correlates with increased chemoresistance (chapter 4), however future studies that examine the role of other mechanisms mentioned are of interest.

In particular, ATP-binding cassette (ABC) transporters belong to a superfamily of proteins involved in extrusion and importing of biomolecules.[131] ABC efflux proteins have gained interest as studies have established their influence in multidrug resistance across varying cell types, with particular focus on ABCB1 (P-gp),[46,47] ABCC1 (MRP1),[48,49] and ABCG2 (BCRP).[50,51] Furthermore, studies that use inhibitors including tariquidar (3rd generation P-gp inhibitor),[132] MK-571 (MRP1 inhibitor),[133] and Ko 143 (BCRP inhibitor)[134] have increased drug efficacy both *in vitro* and *in vivo*. However, no studies have investigated the role of these efflux pumps in dormant and reactivated-cell chemoresistance. To determine if efflux pumps play a role in dormant and reactivated cell chemoresistance, this study investigated P-gp, MRP1, and BCRP expression in growing, dormant (in non-permissive gels 2 and 3), and reactivated parental 231s, organotropic sublines, and MCF7s.

Results showed expression of all three efflux pumps in all 5 cell lines. In the parental 231 line, there was significantly greater P-gp expression in dormant parental 231s in non-permissive gel 3, and greater MRP1 and BCRP expression in chemoresistant dormant (non-permissive gels 2 and 3) and reactivated cells, compared to growing parental 231s in permissive gel 1. Similar trends were observed in all three efflux pumps in organotropic sublines, and for P-gp and MRP1 in MCF7s. Based on these findings, we investigated whether efflux pump inhibition via tariquidar (10 nM P-gp inhibitor), MK-571 (50 μM MRP1 inhibitor), Ko 143 (10 μM BCRP inhibitor), or a combination of these inhibitors influenced DOX efficacy in parental 231s, brain-tropic 231s, and MCF7s via quantification of EC_{50}, accumulation rate, and NC ratio. Results showed that efflux inhibition significantly decreased EC_{50} values for all cells in all formulations. Furthermore, combining all inhibitors decreased dormant (non-permissive gels 2 and 3) and reactivated EC_{50} values to levels significantly lower than cells in permissive gel 1 for parental 231s, brain-tropic 231s, and MCF7s. These findings were accompanied by significant increases in DOX accumulation rate and nuclear localization across all formulations and cell types.

Taken together, this data suggests that dormant and reactivated cells use efflux pumps, P-gp, MRP1, and BCRP to reduce DOX accumulation rate and nuclear localization, leading to increased drug resistance. Inhibition of these efflux pumps significantly increased DOX uptake and nuclear localization and reduced subsequent EC_{50} values, resulting in significantly greater chemosensitivity than growing cells in permissive gel 1. This data indicates that inhibiting P-gp, MRP1, and BCRP in dormant and reactivated breast cancer cells increases drug efficacy, providing a

potential therapeutic strategy to eliminate dormant and reactivated cells, and ultimately aid in preventing metastatic relapse.

5.2 Methods

Methods used for PEG Macromer Synthesis and Characterization, Cell Encapsulation, Reactivation, Statistical Analysis, and measuring PEG-RGDS incorporation, cell viability, degradation rate, Drug Response to DOX, and DOX accumulation and localization were performed as described in Chapters 2, 3, and 4.

5.2.1 Quantification of Efflux Pump Protein Expression

After cell-laden hydrogels were cultured for 15 (gel 1, 2, 3) or 22 days (reactivated), cells were fixed (4% PFA, 30 min), blocked (5% (w/v) BSA, 0.3% (v/v) Triton X-100 in PBS, 30 min), and incubated overnight with anti-MDR1/ABCB1 primary rabbit antibody (Cell Signaling #13342), anti-MRP1 primary mouse antibody (abcam #ab24102), or anti-BCRP/ABCG2 primary mouse antibody (abcam #ab130244) (1:100 in dilution buffer (1% (w/v) BSA, 0.3% (v/v) Triton X-100 in PBS, 4°C). After a PBS wash (30 min), cells were incubated with a goat anti-rabbit or anti-mouse IgG-AlexaFluor647 secondary antibody (1:500 in dilution buffer, 2 h in the dark). Next, cells were incubated with Alexa Fluor 488 Phalloidin (ThermoFisher C#A12379) (6.6 μM) and 10 μg/mL Hoechst 33342 (nuclei) in PBS (30 min). Labeled cells were stored in PBS at 4°C. Imaging was performed as described in section 3.2.2. To quantify protein expression, a sum z-projection was acquired from each z-stack and the mean fluorescence intensity of each projection was measured accounting for background noise as described in chapter 3. Using the Hoechst nuclear counterstain, the total number of cells were counted and used to obtain mean fluorescence (AU) for

P-gp, MRP1, and BCRP for each cell line in each gel type. Measurements were obtained from a minimum of 6 z-stacks from 6 individual hydrogels for each experimental condition.

5.2.2 Efflux Inhibition in Doxorubicin Drug Studies

DOX stock solutions were prepared as described in chapter 4. In experiments involving efflux inhibition, 5mM stock solutions of P-gp inhibitor (tariquidar dihydrochloride (Tocris #5757)), MRP1 inhibitor (MK 571 (Tocris #2338)), and BCRP inhibitor (Ko 143 (Tocris #3241) were prepared in DMSO. Stock solutions were diluted in media to desired concentrations (P-gp inhibitor (10 nM), MRP1 inhibitor (50 μM), and BCRP inhibitor (10 μM)). At day15 or 22, cell-laden hydrogels were incubated with each inhibitor or a cocktail of inhibitors for 24 h.

For dose-response experiments, cells were next exposed to varying concentrations of DOX (0.001, 0.01, 0.05, 0.1, 0.55, 1 mM) dosed with each inhibitor condition for 48 h, rinsed, labeled, and analyzed as described in chapter 4. To measure DOX accumulation or localization, cells were exposed to 0.05 mM DOX dosed with each inhibitor condition for 48 h. Accumulation was then measured over 48 h as described in chapter 4, and localization was measured as described in chapter 4. Measurements were obtained from a minimum of 6 z-stacks from 6 individual hydrogels for each experimental condition.

5.3 Results

5.3.1 Efflux Pump (P-gp, MRP1, BCRP) Expression

Based on the findings that chemoresistant dormant and reactivated cells display lower levels of DOX accumulation and nuclear localization (described in

chapter 4), we were interested in determining if efflux pump expression played a role in breast cancer cell chemosensitivity. To first determine if the cells in our system expressed efflux pumps, cells were grown to day 15 (gel 1, 2, 3) or 22 (reactivated), fixed, and labeled for chemoresistance-associated efflux pumps P-gp, MRP1, or BCRP. Cell nuclei and cytoskeleton were also labeled. Efflux pump expression was measured by quantifying fluorescence intensity per cell (AU).

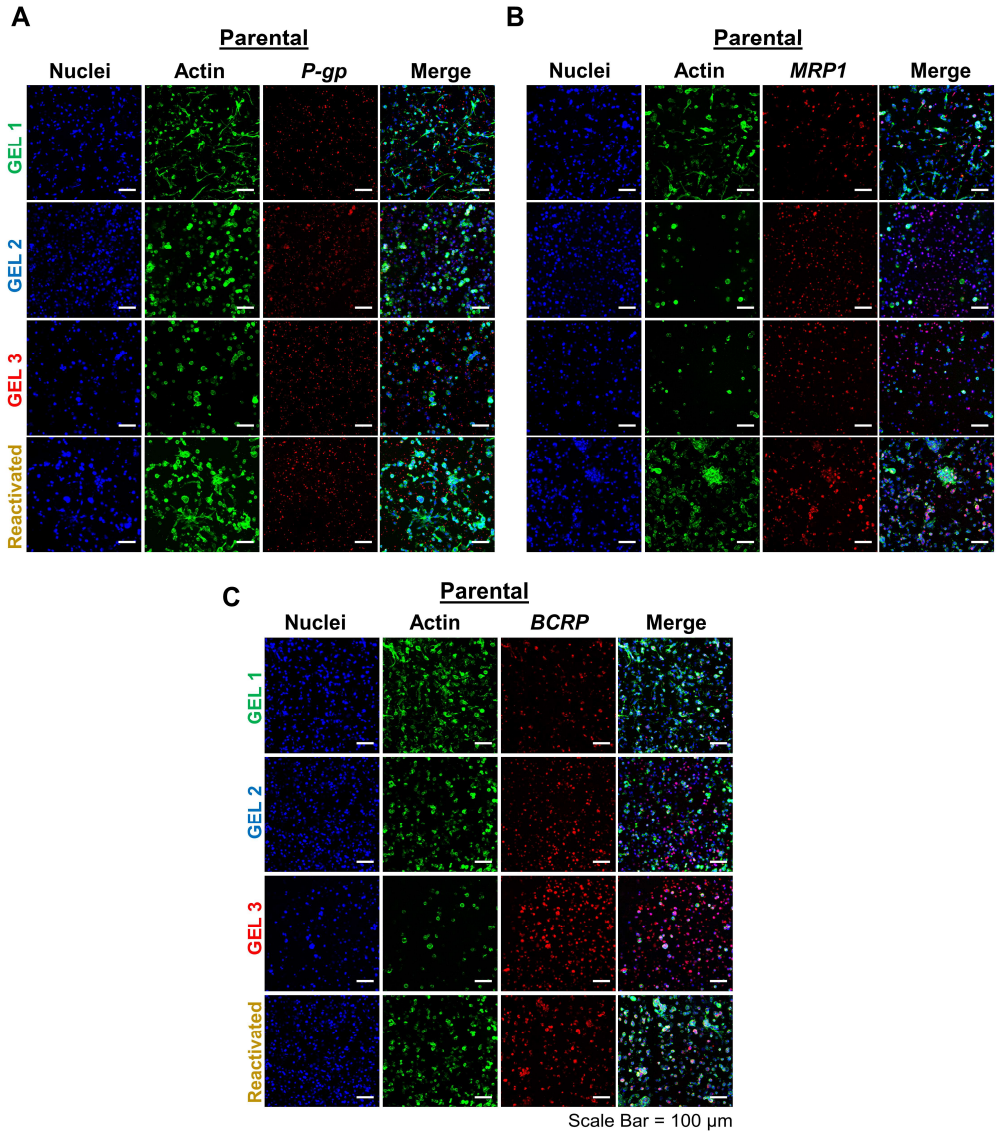

Figure 5.1: Efflux Pump Expression in Dormant and Reactivated Parental 231s. Representative sum intensity z-projections from 3D image stacks of MDA-MB-231s (parental 231s) that were cultured in each hydrogel formulation, fixed, and fluorescently labeled for (A) P-gp, (B) MRP1, or (C) BCRP (red), phalloidin (F-actin: green), and counterstained with Hoechst (nuclei: blue). Scale bar = 100 µm.

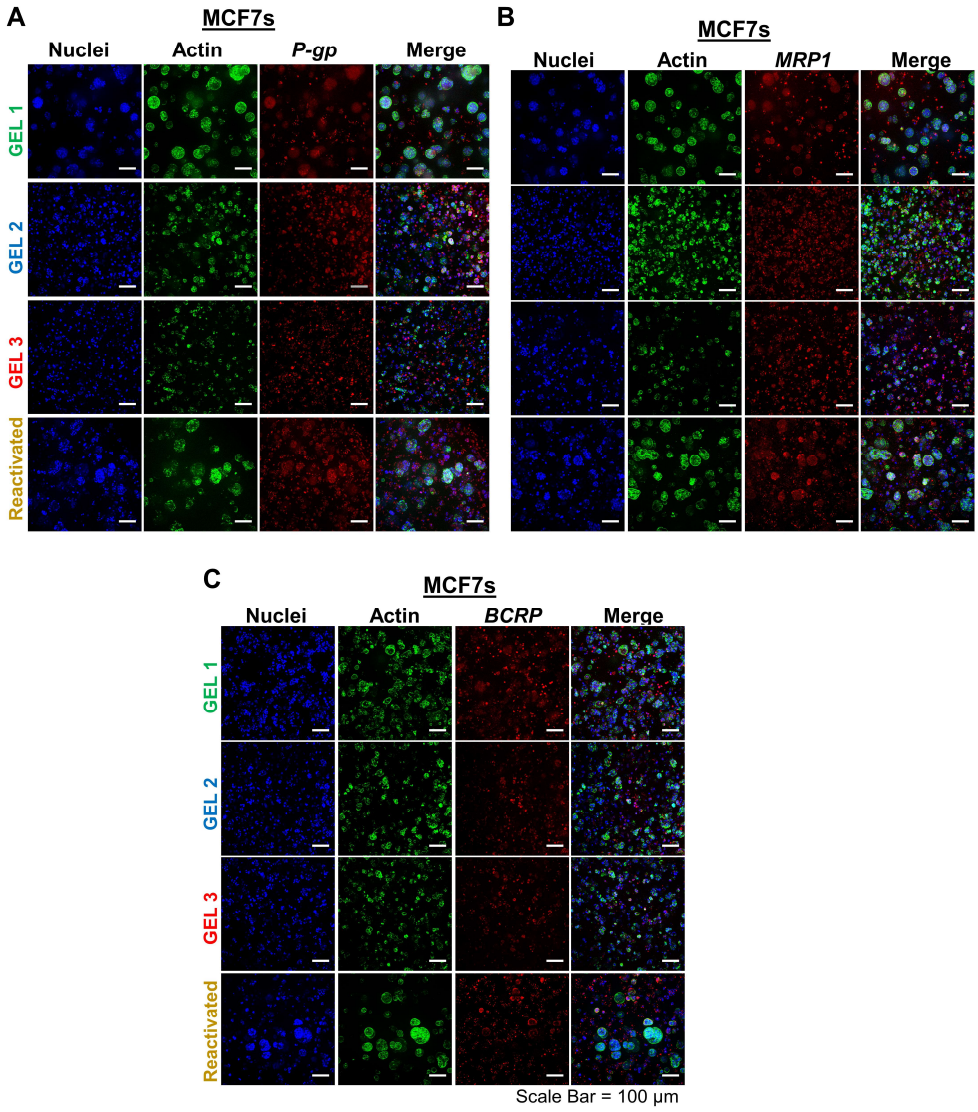

Figure 5.2: Efflux Pump Expression in Dormant and Reactivated MCF7s. Representative sum intensity z-projections from 3D image stacks of MCF7s that were cultured in each hydrogel formulation, fixed, and fluorescently labeled for (A) P-gp, (B) MRP1, or (C) BCRP (red), phalloidin (F-actin: green), and counterstained with Hoechst (nuclei: blue). Scale bar = 100 µm.

Results showed that dormant parental 231s in non-permissive gel 3 expressed significantly greater levels of P-gp compared to all other formulations (permissive gel

1: 0.24 ± 0.06, non-permissive gel 2: 0.29 ± 0.07, non-permissive gel 3: 0.53 ± 0.20, reactivated: 0.24 ± 0.05) (Figure 5.1, 5.6). When quantifying MRP1 expression, we found that there was significantly greater MRP1 expression in chemoresistant dormant (non-permissive gel 2: 0.71 ± 0.15, non-permissive gel 3: 0.93 ± 0.23) and reactivated cells (1.88 ± 0.21), compared to chemosensitive, growing cells in permissive gel 1 (0.15 ± 0.04) (Figure 5.6). The same trend was observed for BCRP expression, with dormant cells in non-permissive gel 3 having the highest BCRP levels (permissive gel 1: 0.27 ± 0.06, non-permissive gel 2: 1.22 ± 0.23, non-permissive gel 3: 3.12 ± 0.65, reactivated: 1.42 ± 0.26) (Figure 5.6).

In organotropic lines, greater levels of efflux pump expression in chemoresistant dormant and reactivated cells were also observed (Figure 5.2-5.6). For instance, bone-tropic 231s had P-gp expression levels of 0.29 ± 0.12 ((growing) permissive gel 1), 0.73 ± 0.15 ((dormant) non-permissive gel 2), 1.04 ± 0.31 ((dormant) non-permissive gel 3), and 0.67 ± 0.05 (reactivated). Bone-tropic MRP1 expression was 0.23± 0.07 ((growing) permissive gel 1), 1.05 ± 0.15 ((dormant) non-permissive gel 2), 1.10 ± 0.14 ((dormant) non-permissive gel 3), and 0.81 ± 0.07 (reactivated)), with significantly greater MRP1 expression in dormant cells, followed by reactivated cells, compared to growing cells in permissive gel 1.

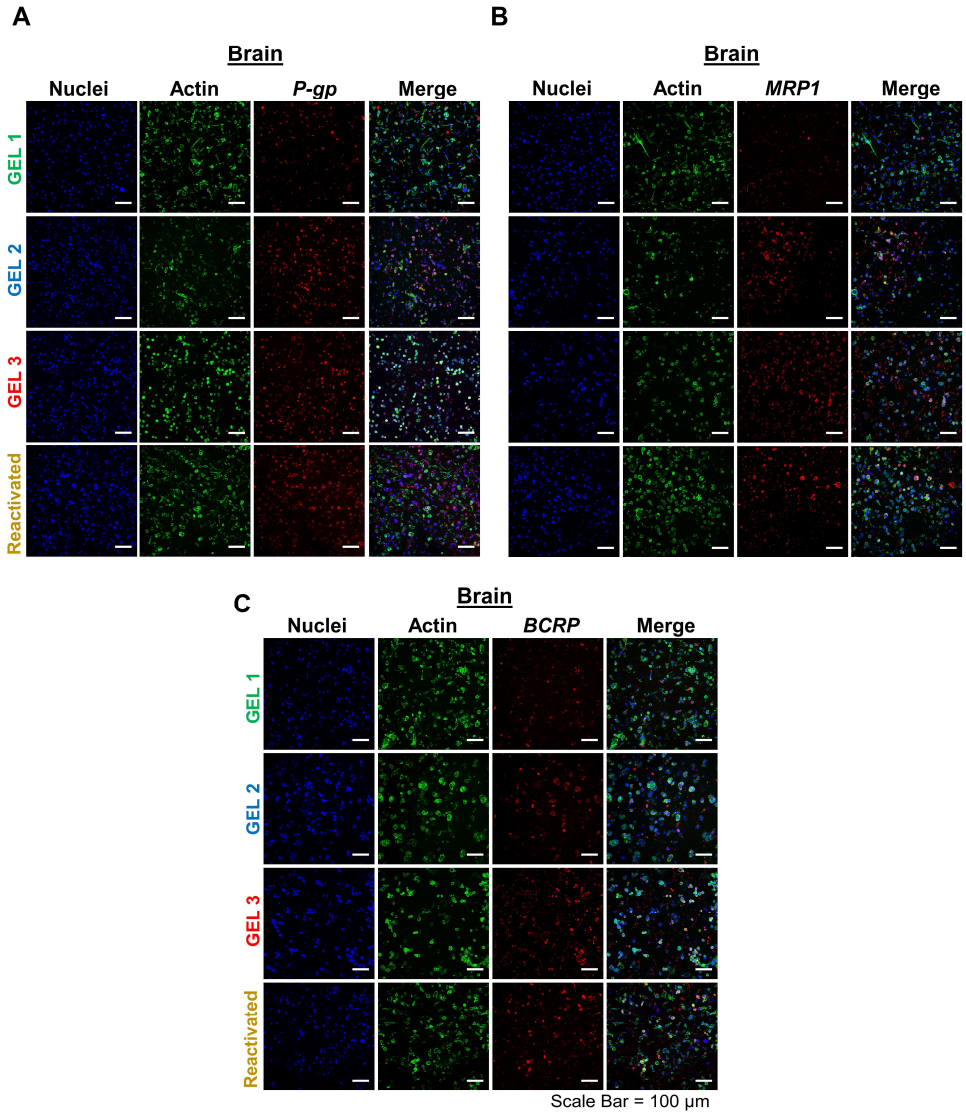

Figure 5.3: Efflux Pump Expression in Dormant and Reactivated Brain-tropic cells. Representative sum intensity z-projections from 3D image stacks) BrM2-831s (brain-tropic) sublines that were cultured in each hydrogel formulation, fixed, and fluorescently labeled for (A) P-gp, (B) MRP1, or (C) BCRP (red), phalloidin (F-actin: green), and counterstained with Hoechst (nuclei: blue). Scale bar = 100 µm.

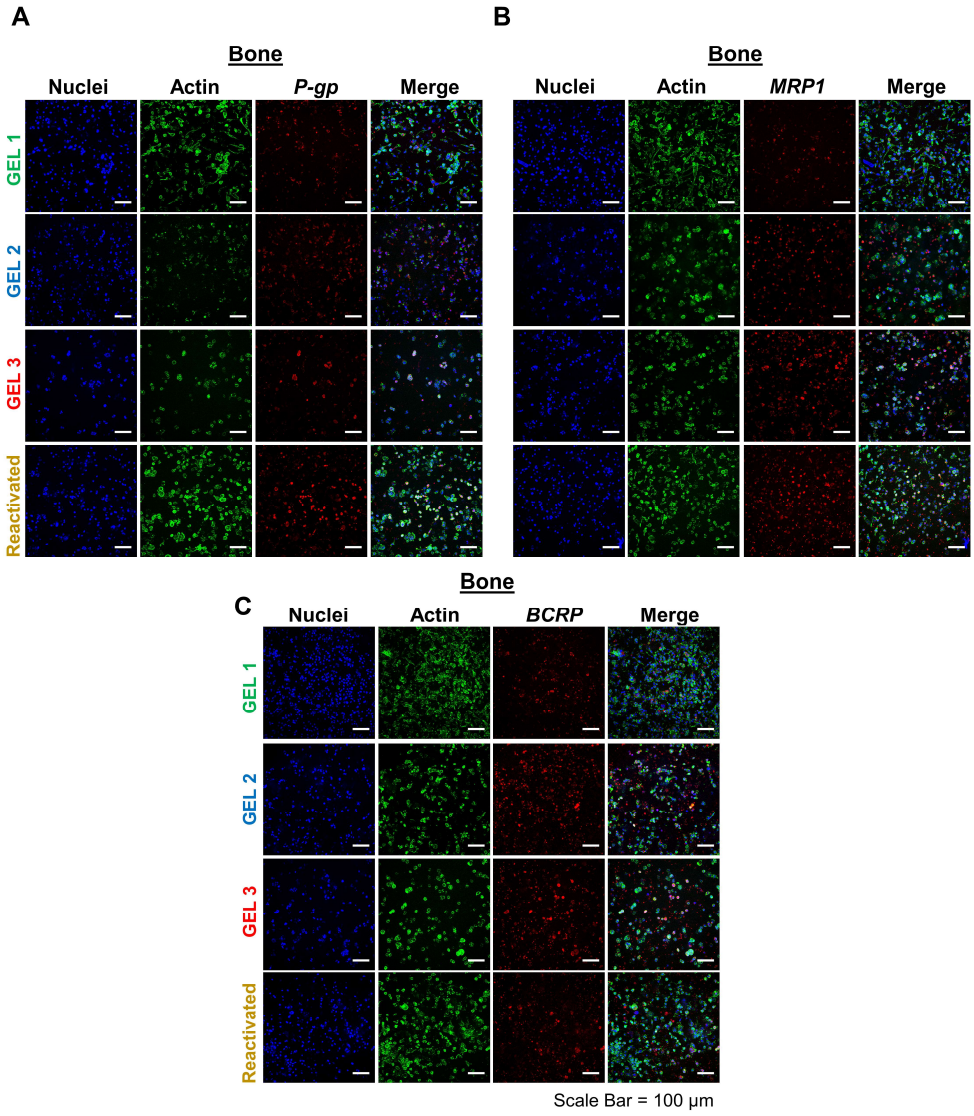

Figure 5.4: Efflux Pump Expression in Dormant and Reactivated Bone-tropic cells. Representative sum intensity z-projections from 3D image stacks) BoM-1833s (bone-tropic) sublines that were cultured in each hydrogel formulation, fixed, and fluorescently labeled for (A) P-gp, (B) MRP1, or (C) BCRP (red), phalloidin (F-actin: green), and counterstained with Hoechst (nuclei: blue). Scale bar = 100 µm.

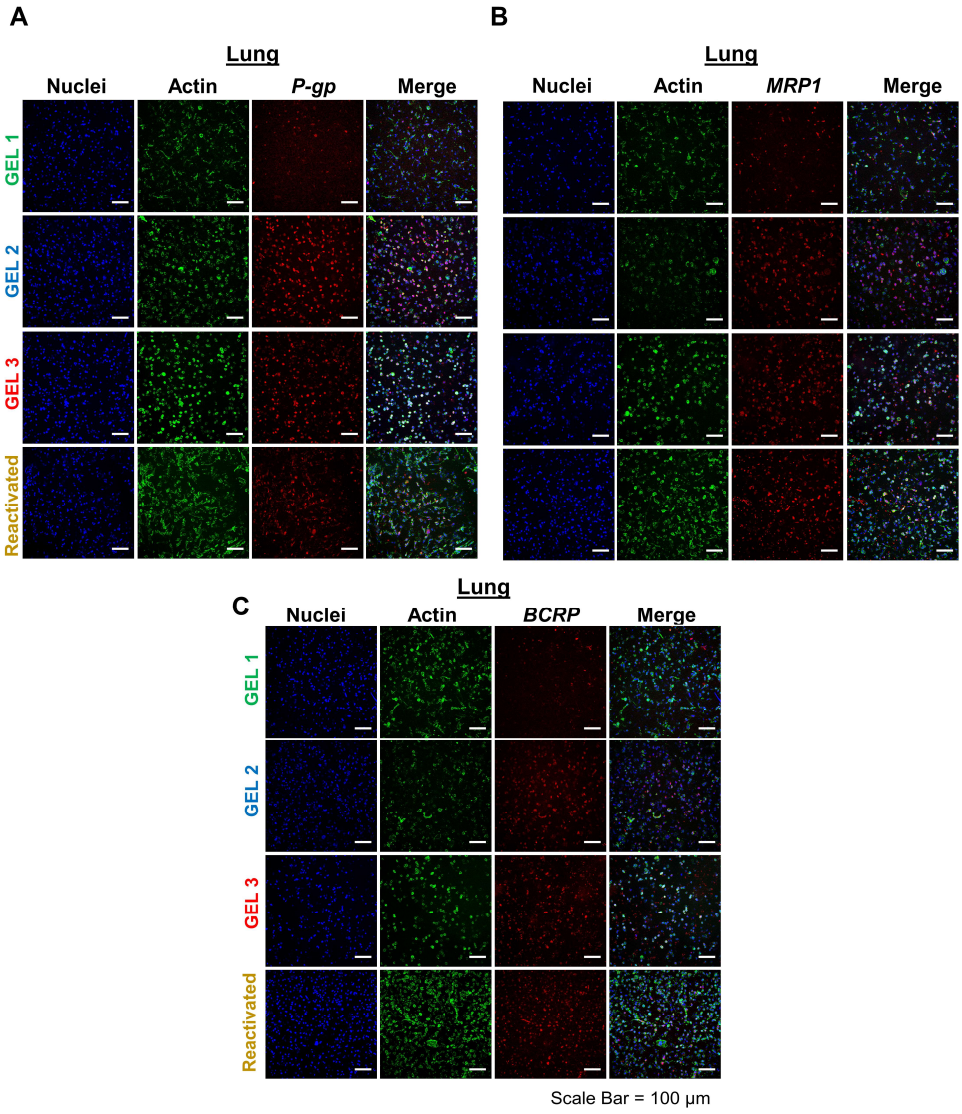

Figure 5.5: Efflux Pump Expression in Dormant and Reactivated Lung-tropic cells. Representative sum intensity z-projections from 3D image stacks) LM2-4175s (lung-tropic) sublines that were cultured in each hydrogel formulation, fixed, and fluorescently labeled for (A) P-gp, (B) MRP1, or (C) BCRP (red), phalloidin (F-actin: green), and counterstained with Hoechst (nuclei: blue). Scale bar = 100 µm.

BCRP was also expressed in significantly lower amounts in growing bone-tropic cells ((growing) permissive gel 1: 0.35 ± 0.08, (dormant) non-permissive gel 2: 0.68 ± 0.12, (dormant) non-permissive gel 3: 0.86 ± 0.09, reactivated: 0.63 ± 0.17). Similar trends were observed for lung-tropic P-gp ((growing) permissive gel 1: 0.26 ± 0.05, (dormant) non-permissive gel 2: 0.89 ± 0.13, (dormant) non-permissive gel 3: 1.01 ± 0.13, reactivated: 0.65 ± 0.01), MRP1 ((growing) permissive gel 1: 0.23 ± 0.06, (dormant) non-permissive gel 2: 0.57 ± 0.07, (dormant) non-permissive gel 3: 0.91 ± 0.10, reactivated: 0.94 ± 0.05), and BCRP expression ((growing) permissive gel 1: 0.25 ± 0.07, (dormant) non-permissive gel 2: 0.90 ± 0.07, (dormant) non-permissive gel 3: 0.99 ± 0.11, reactivated: 0.62 ± 0.12), as well as brain-tropic P-gp ((growing) permissive gel 1: 0.27 ± 0.10, (dormant) non-permissive gel 2: 0.84 ± 0.17, (dormant) non-permissive gel 3: 0.83 ± 0.14, reactivated: 0.55 ± 0.09), MRP1 ((growing) permissive gel 1: 0.24 ± 0.04, (dormant) non-permissive gel 2: 0.75 ± 0.11, (dormant) non-permissive gel 3: 0.98 ± 0.15, reactivated: 0.74 ± 0.08), and BCRP expression ((growing) permissive gel 1: 0.28 ± 0.08, (dormant) non-permissive gel 2: 0.78 ± 0.15, (dormant) non-permissive gel 3: 0.77 ± 0.10, reactivated: 0.48 ± 0.08).

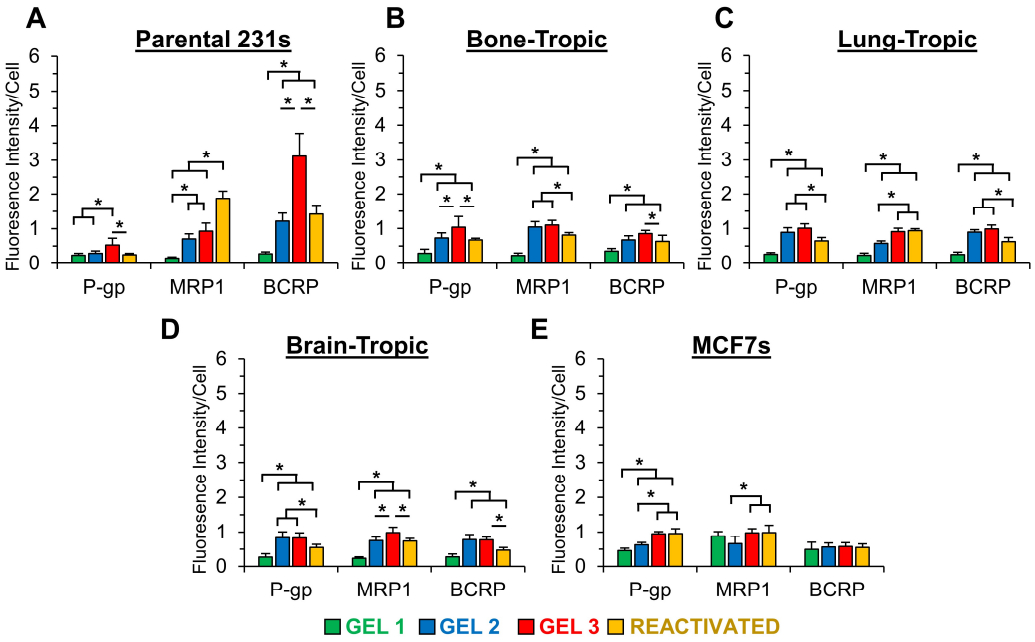

Figure 5.6: Efflux Pump Quantification in Dormant and Reactivated Cells. Quantification of efflux pump (P-gp, MRP1, BCRP) expression by measuring fluorescent per cell in (A) MDA-MB-231s (parental 231s), (B) BoM-1833s (bone-tropic), (C) LM2-4175s (lung-tropic), (D) BrM2a-831s (brain-tropic), and (E) MCF7s. * indicates $p < 0.05$ determined by a one-way ANOVA. n = 6 z-stacks from six individual hydrogels.

In MCF7s, P-gp expression was significantly higher in chemoresistant dormant and reactivated cells ((growing) permissive gel 1: 0.46 ± 0.07, (dormant) non-permissive gel 2: 0.63 ± 0.07, (dormant) non-permissive gel 3: 0.95 ± 0.07, reactivated: 0.96 ± 0.14), and MRP1 expression was significantly higher in dormant cells in non-permissive gel 3 and reactivated cells ((growing) gel 1: 0.89 ± 0.13, (dormant) non-permissive gel 2: 0.67 ± 0.21, (dormant) non-permissive gel 3: 0.98 ± 0.12, reactivated: 0.98 ± 0.21) (Figure 5.6). Interestingly, no significant differences were observed in BCRP expression between growing, dormant, and reactivated

MCF7s ((growing) permissive gel 1: 0.49 ± 0.21, (dormant) non-permissive gel 2: 0.56 ± 0.12, (dormant) non-permissive gel 3: 0.58 ± 0.11, reactivated: 0.55 ± 0.10).

Overall, these results indicate that chemoresistant dormant and reactivated cells express greater levels of efflux pumps P-gp, MRP1, and BCRP compared to chemosensitive cells in permissive gel 1. This suggests that efflux pump expression may play a role in observed chemoresistance to DOX and decreased accumulation and nuclear localization.

5.3.2 Influence of P-gp, MRP1, BCRP Inhibition in Doxorubicin Chemosensitivity

To determine if differential efflux pump, P-gp, MRP1, or BCRP, expression played a role in dormant and reactivated-cell chemoresistance, we investigated drug response after efflux pump inhibition in parental 231s, a representative organotropic line (brain-tropic), and MCF7s. Inhibitors were added to cell-laden hydrogels for 24 h after 15 or 22 days in culture: P-gp inhibitor (10 nM tariquidar), MRP1 inhibitor (50 μM MK571), or BCRP inhibitor (10 μM Ko 143). Cells were then exposed to varying concentrations of DOX with either P-gp inhibitor, MRP1 inhibitor, BCRP inhibitor, or a combination of all three (P-gp+MRP1+BCRP inhibitor) for 48 h. Since MCF7s did not show differential BCRP expression, these cells were only exposed to P-gp inhibitor, MRP1 inhibitor, or a combination (P-gp+MRP1 inhibitor). After 48 h, cells were rinsed, labeled for viability, imaged, and analyzed to obtain dose-response curves (Figure 5.7) and EC_{50} and IC_{50} values. To confirm, efflux pump inhibition did not influence viability, preliminary studies that compared the number of viable cells with media to those with inhibitor (no DOX) were conducted and indicate no significant

difference, indicating that efflux pump inhibition alone did not influence cell viability (Figure 5.7).

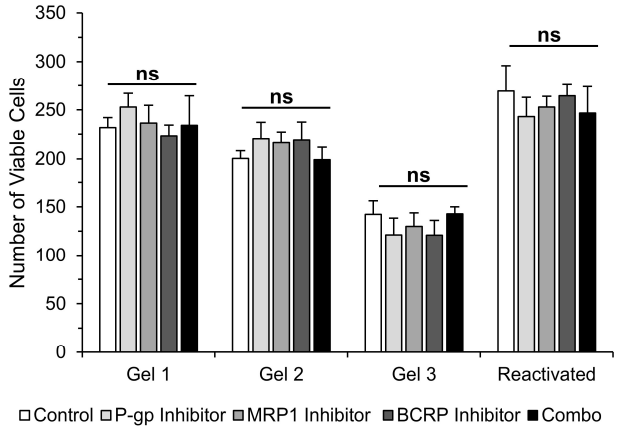

Figure 5.7: Influence of Efflux Inhibition on Cell Viability. Average viable cell number of encapsulated MDA-MB-231s present when exposed to media with + 1%DMSO (control), P-gp inhibitor (10 nM tariquidar), MRP1 inhibitor (50 μM MK571), BCRP inhibitor (10 μM Ko 143), or a combination of all three inhibitors. Results indicate that efflux inhibition has no significant impact in viable cell number. n=6 z-stacks from 6 individual hydrogels. Values represent mean + standard deviation.

In the parental 231 line, P-gp inhibition increased chemosensitivity and significantly decreased EC_{50} values of cells undergoing growth in permissive gel 1 from 44.8 ± 4.2 to 9.5 ± 0.8 μM (~5-fold decrease), cells undergoing dormancy in non-permissive gel 2 from 67.1 ± 16.2 to 38.4 ± 6.3 μM (~2-fold decrease), cells undergoing dormancy in non-permissive gel 3 from 89.1 ± 12.4 to 32.7 ± 6.3 μM (~3-fold decrease), and reactivated cells from 113.0 ± 16.0 to 23.5 ± 2.3 μM (5-fold decrease) (Figure 5.8-5.9). However, dormant (non-permissive gels 2 and 3) and reactivated parental 231s maintained some chemoresistance compared to cells in the

growth state, with significantly higher EC_{50} values compared to growing cells in permissive gel 1. MRP1 inhibition decreased EC_{50} values to 24.3 ± 11.4 μM (permissive gel 1),16.0 ± 5.0 μM (non-permissive gel 2), 12.2 ± 2.9 μM (non-permissive gel 3), and 5.8 ± 1.1 μM (reactivated). Furthermore, MRP1 inhibition increased dormant cell (non-permissive gels 2 and 3) chemosensitivity, with significantly lower EC_{50} values for dormant and reactivated cells compared to cells in the growth state. BCRP inhibition led to similar results and dropped EC_{50} values to 13.3 ± 1.5 μM (permissive gel 1), 7.4 ± 0.7 μM (non-permissive gel 2), 1.1 ± 0.4 μM (non-permissive gel 3), and 5.6 ± 0.7 μM (reactivated). Inhibiting P-gp, MRP1, and BCRP had the greatest effect, dropping EC_{50} values to 4.2 ± 1.1 μM (permissive gel 1, ~11-fold decrease), 0.4 ± 0.1 μM (non-permissive gel 2, ~170-fold decrease), 1.1 ± 0.5 μM (gel 3, ~81-fold decrease), and 1.4 ± 0.3 μM (reactivated, ~81-fold decrease). Furthermore, inhibition of all three efflux pumps increased dormant (non-permissive gels 2 and 3) and reactivated cell chemosensitivity to the extent that growing 231s in permissive gel 1 had a significantly greater EC_{50}, rendering them less chemosensitive than dormant and reactivated parental 231s due to efflux pump inhibition.

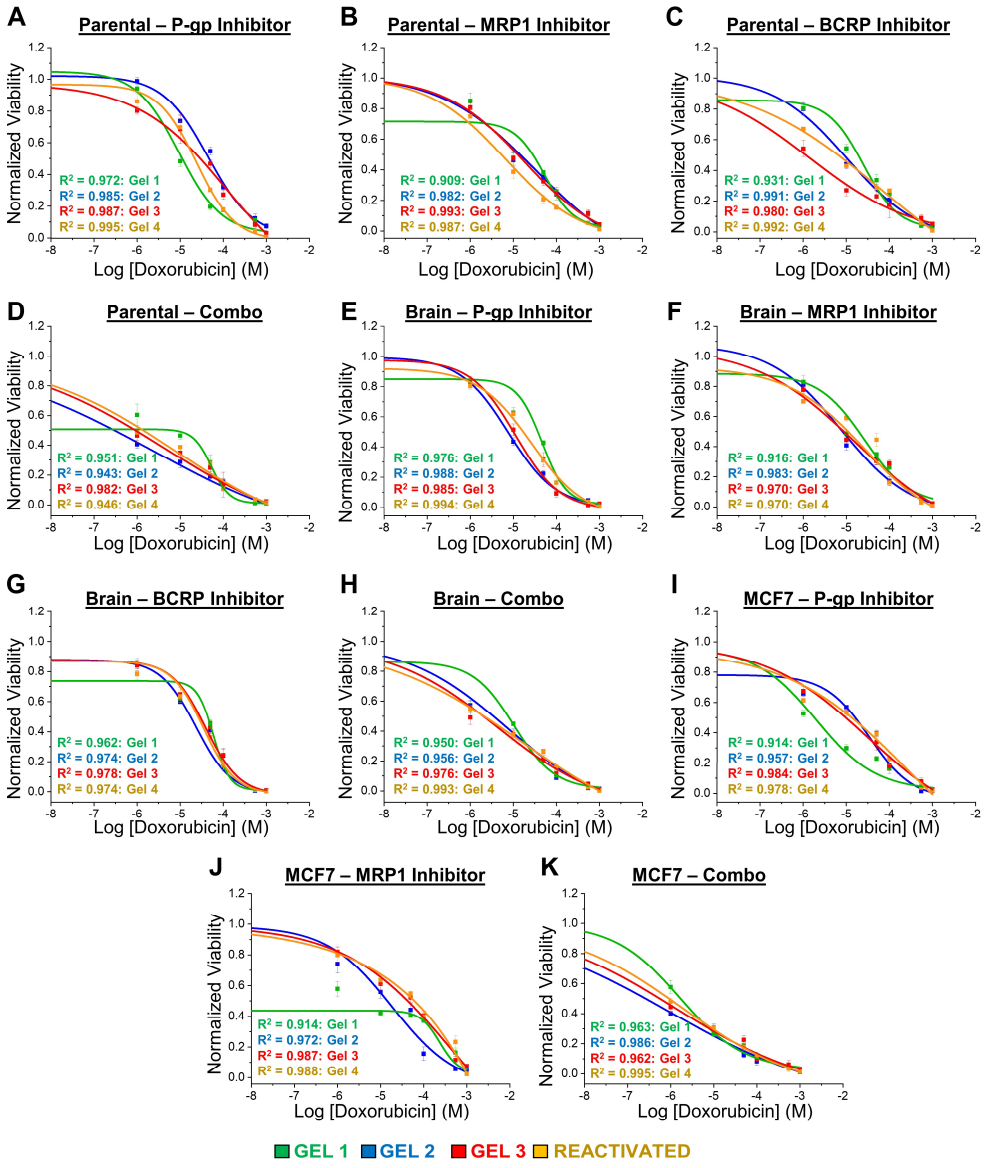

Figure 5.8: Doxorubicin Dose-Response Curves in Dormant and Reactivated Cells. Doxorubicin dose-response curves for (A-D) MDA-MB-231s (parental), (E-H) BrM2a-831s (brain-tropic), or (I-K) MCF7s with no inhibitor, P-gp inhibitor (10 nM tariquidar), MRP1 inhibitor (50 µM MK571), BCRP inhibitor (10 µM Ko 143), or a combination of all inhibitors. n=6 z-stacks from 6 individual hydrogels. Values represent mean ± standard deviation.

In brain-tropic 231s, P-gp inhibition decreased EC_{50} values from 44.9 ± 6.2 to 22.9 ± 3.0 μM in permissive gel 1, 65.5 ± 7.7 to 6.9 ± 0.7 μM in non-permissive gel 2, 85.7 ± 14.4 to 11.2 ± 2.0 μM in non-permissive gel 3, and 113.0 ± 15.7 to 5.6 ± 0.7 μM in reactivated cells, with significantly lower EC_{50} values for dormant (non-permissive gels 2 and 3) and reactivated cells compared to growing cells in permissive gel 1, indicating greater chemosensitivity (Figure 5.8-5.10). Similar trends were observed with MRP1 (EC_{50}: permissive gel 1: 11.8 ± 1.2 μM, non-permissive gel 2: 7.2 ± 1.2 μM, non-permissive gel 3: 8.3 ± 0.5 μM, reactivated: 17.0 ± 1.3 μM), and BCRP inhibition (EC_{50}: permissive gel 1: 25.0 ± 3.0 μM, non-permissive gel 2: 21.7 ± 1.4 μM, non-permissive gel 3: 28.2 ± 1.4 μM, reactivated: 21.6 ± 4.9 μM). Inhibition of all three efflux pumps resulted in a ~17-fold (permissive gel 1 EC_{50}: 2.7 ± 0.6 μM), ~26-fold (non-permissive gel 2 EC_{50}: 2.5 ± 0.5 μM), ~61-fold (non-permissive gel 3 EC_{50}: 1.4 ± 0.4 μM), and ~40-fold decrease (reactivated EC_{50}: 2.3 ± 0.3 μM) in EC_{50} values.

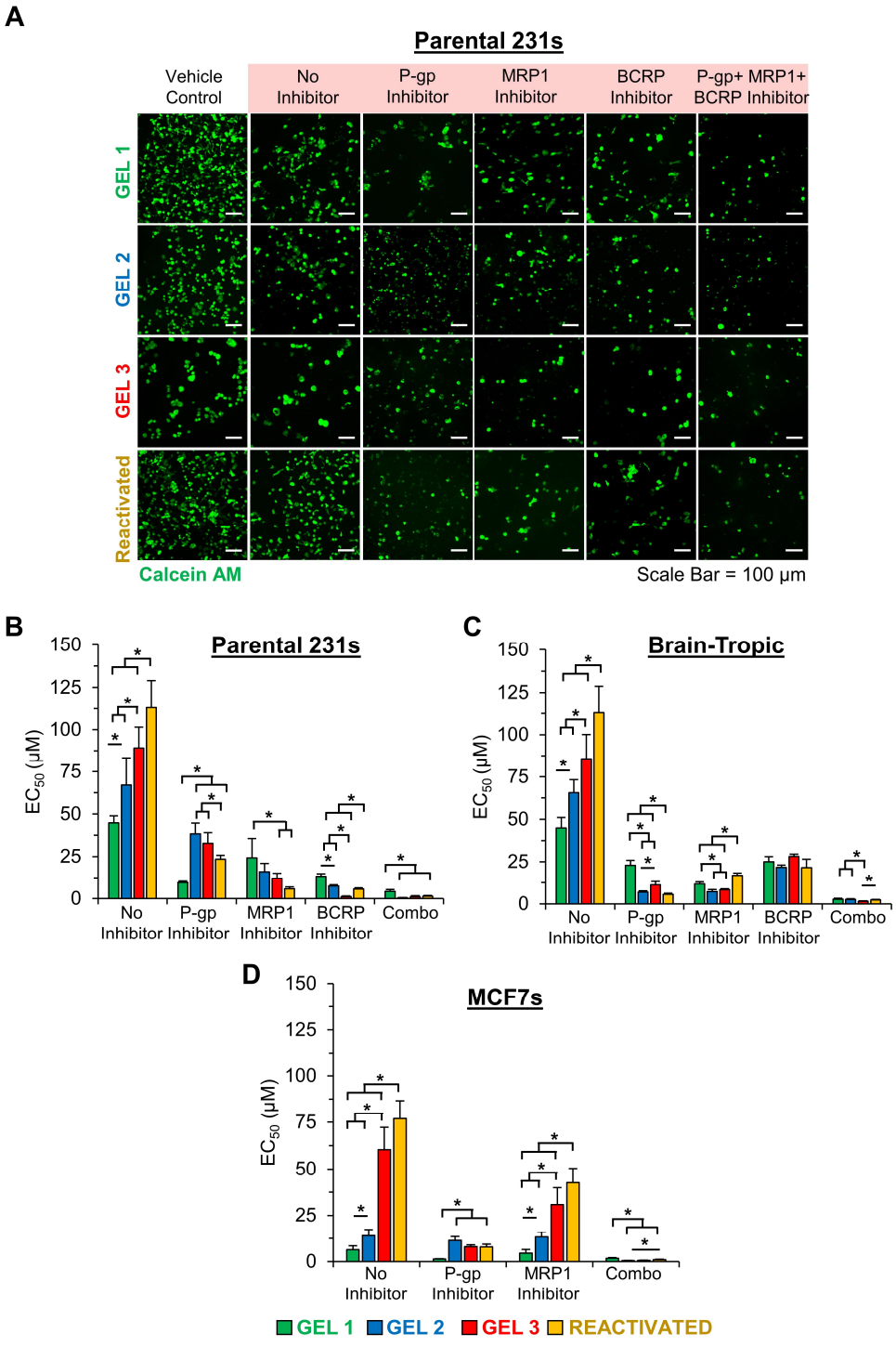
A
Parental 231s
Vehicle Control
No Inhibitor
P-gp Inhibitor
MRP1 Inhibitor
BCRP Inhibitor
P-gp+ MRP1+ BCRP Inhibitor
GEL 1
GEL 2
GEL 3
Reactivated
Calcein AM
Scale Bar = 100 µm
B
Parental 231s
C
Brain-Tropic
D
MCF7s
EC50 (µM)
No Inhibitor
P-gp Inhibitor
MRP1 Inhibitor
BCRP Inhibitor
Combo
GEL 1
GEL 2
GEL 3
REACTIVATED

Figure 5.9: Influence of Efflux Pump Inhibition in Doxorubicin Chemosensitivity of Dormant and Reactivated Cells. (A) Representative maximum intensity z-projections from 3D image stacks of live (Calcein AM:green) MDA-MB-231s (parental 231s) after 15 days in culture followed by 48 h exposure to 0.05 mM doxorubicin with no inhibitor, P-gp inhibitor (10 nM tariquidar), MRP1 inhibitor (50 μM MK571), BCRP inhibitor (10 μM Ko 143), or a combination of all three. Scale bar = 100 μm. Calculated EC_{50} values for (B) MDA-MB-231s (parental), (C) BrM2-831s (brain-tropic), or (D) MCF7s with no inhibitor or the indicated inhibitor. * indicates statistically significant difference ($p<0.05$). n=6 z-stacks from 6 individual hydrogels. Values represent mean + standard deviation.

P-gp inhibition in MCF7s dropped EC_{50} values from 6.3 ± 2.1 to 1.3 ± 0.2 μM in permissive gel 1, 13.9 ± 3.4 to 11.3 ± 2.1 μM in non-permissive gel 2, 60.4 ± 11.8 to 8.0 ± 1.0 μM in non-permissive gel 3, and 76.9 ± 9.7 to 7.8 ± 1.5 μM in reactivated cells (Figure 5.8-5.10). However, dormant (non-permissive gels 2 and 3), and reactivated cells maintained significantly higher chemoresistance compared to growing cells in permissive gel 1 with P-gp inhibition. Dormant and reactivated cell chemoresistance was also sustained during MRP1 inhibition (permissive gel 1: 4.5 ± 2.0 μM, non-permissive gel 2: 13.2 ± 2.8 μM, non-permissive gel 3: 30.8 ± 9.1 μM, reactivated: 42.6 ± 7.8 μM). However, inhibition of both P-gp+MRP1 dropped EC_{50} values to 1.7 ± 0.4 μM (permissive gel 1), 0.5 ± 0.1 μM (non-permissive gel 2), 0.6 ± 0.1 μM (non-permissive gel 3), 1.0 ± 0.2 μM (reactivated). In addition to increasing overall DOX efficacy, P-gp+MRP1 inhibition increased dormant (non-permissive gels 2 and 3) and reactivated cell chemosensitivity to levels exceeding chemosensitivity of growing cells in permissive gel 1.

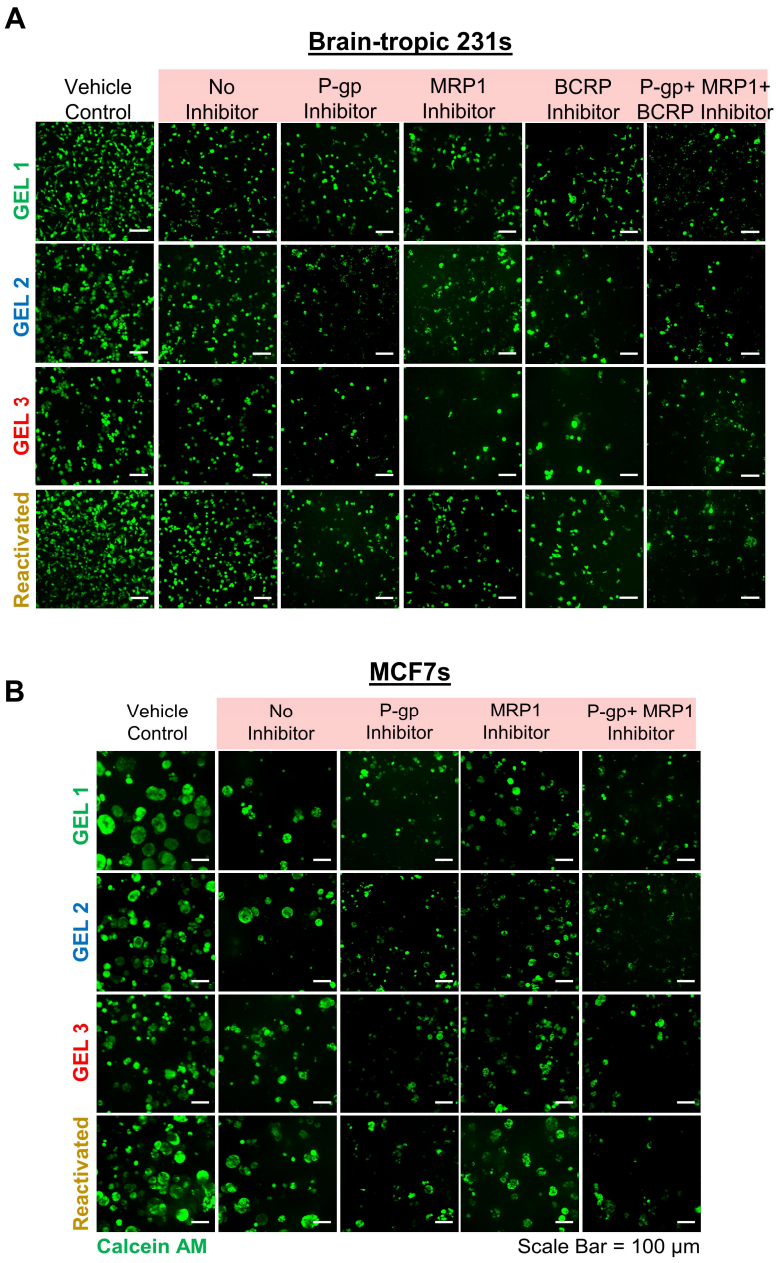

Figure 5.10: Influence of Efflux Pump Inhibition on Doxorubicin Chemosensitivity of Dormant and Reactivated Brain-tropic and MCF7s. Representative maximum intensity z-projections from 3D image stacks of live (Calcein AM:green) (A) BrM2-831s (brain-tropic) and (B) MCF7s after 15 days in culture followed by 48 h exposure to 0.05 mM doxorubicin with no inhibitor, P-gp inhibitor (10 nM tariquidar), MRP1 inhibitor (50 µM MK571), BCRP inhibitor (10 µM Ko 143), or a combination of all three. Scale bar = 100 µm.

Taken together, this data demonstrates that inhibiting efflux pumps P-gp, MRP1, and BCRP increased DOX efficacy by significantly reducing EC_{50} values. Additionally, inhibiting these pumps diminished dormant (non-permissive gels 2 and 3) and reactivated cell chemoresistance compared to permissive gel 1, suggesting that dormant and reactivated cells may use efflux pumps to avoid drug-induced cytotoxicity.

5.3.3 Influence of P-gp, MRP1, BCRP Inhibition in Doxorubicin Accumulation

To determine if efflux pump inhibition increased DOX chemosensitivity by altering intracellular DOX accumulation, after 15 or 22 days in culture, P-gp inhibitor (10 nM tariquidar), MRP1 inhibitor (50 μM MK571), BCRP inhibitor (10 μM Ko 143), or a combination of all three were added to the hydrogels in media. As noted earlier, BCRP inhibition was not performed on MCF7s. After 24 h, 0.05 mM DOX with each inhibitor condition was added and accumulation was measured at varying time points (1, 2, 3, 4, 5, 6, 12, 24, 36, 48 h) over 48 h as described in chapter 4 (Figure 5.11-5.13). The accumulation rate was calculated as the linear slope of the accumulation over time plot.

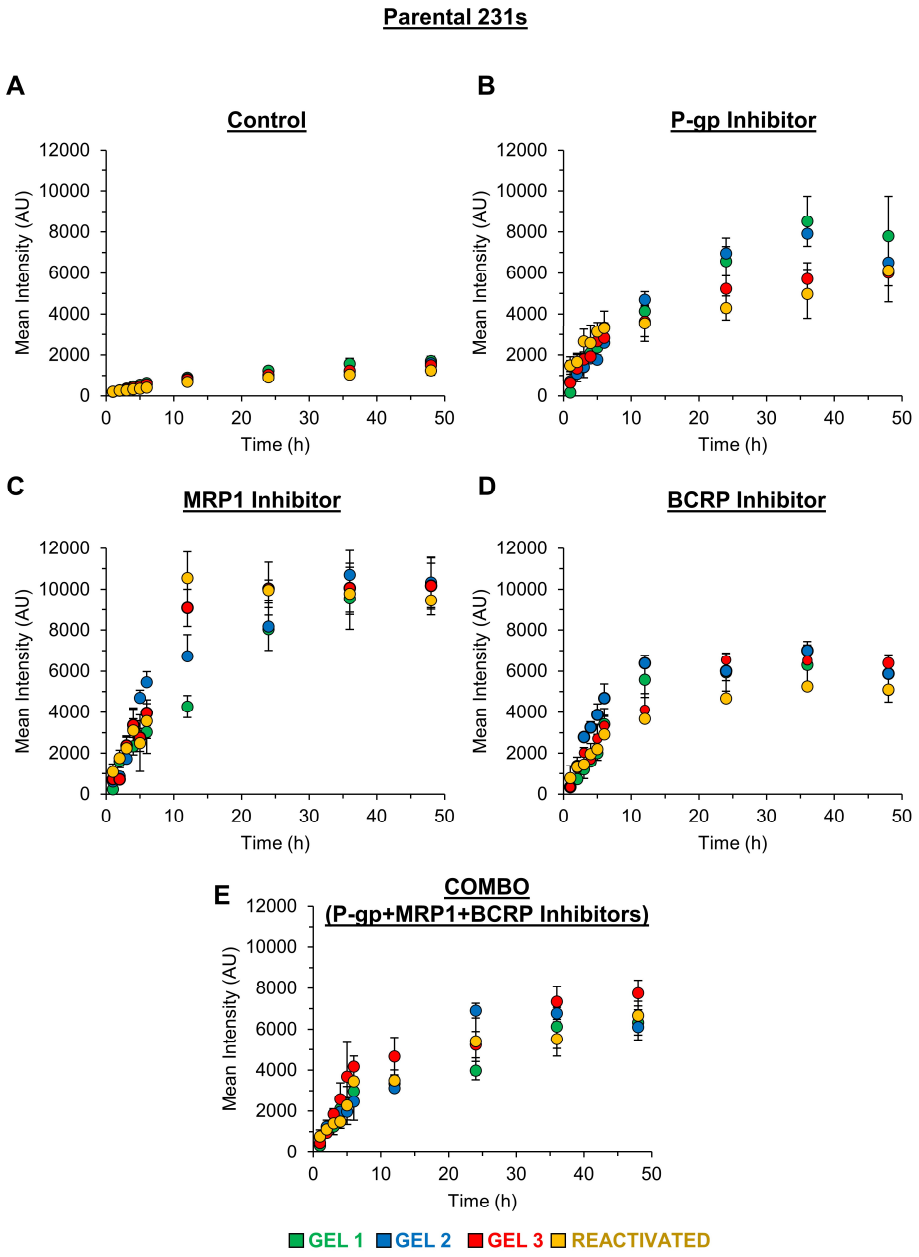

Figure 5.11: Doxorubicin Accumulation on Parental 231s. Quantification of doxorubicin (0.05 mM) accumulation in MDA-MB-231s (parental 231s) with (A) no inhibitor, (B) P-gp inhibitor (10 nM tariquidar), (C) MRP1 inhibitor (50 µM MK571), (D) BCRP inhibitor (10 µM Ko 143), or (E) a combination of all three inhibitors over 48 h via fluorescence intensity. Value represent mean ± standard deviation.

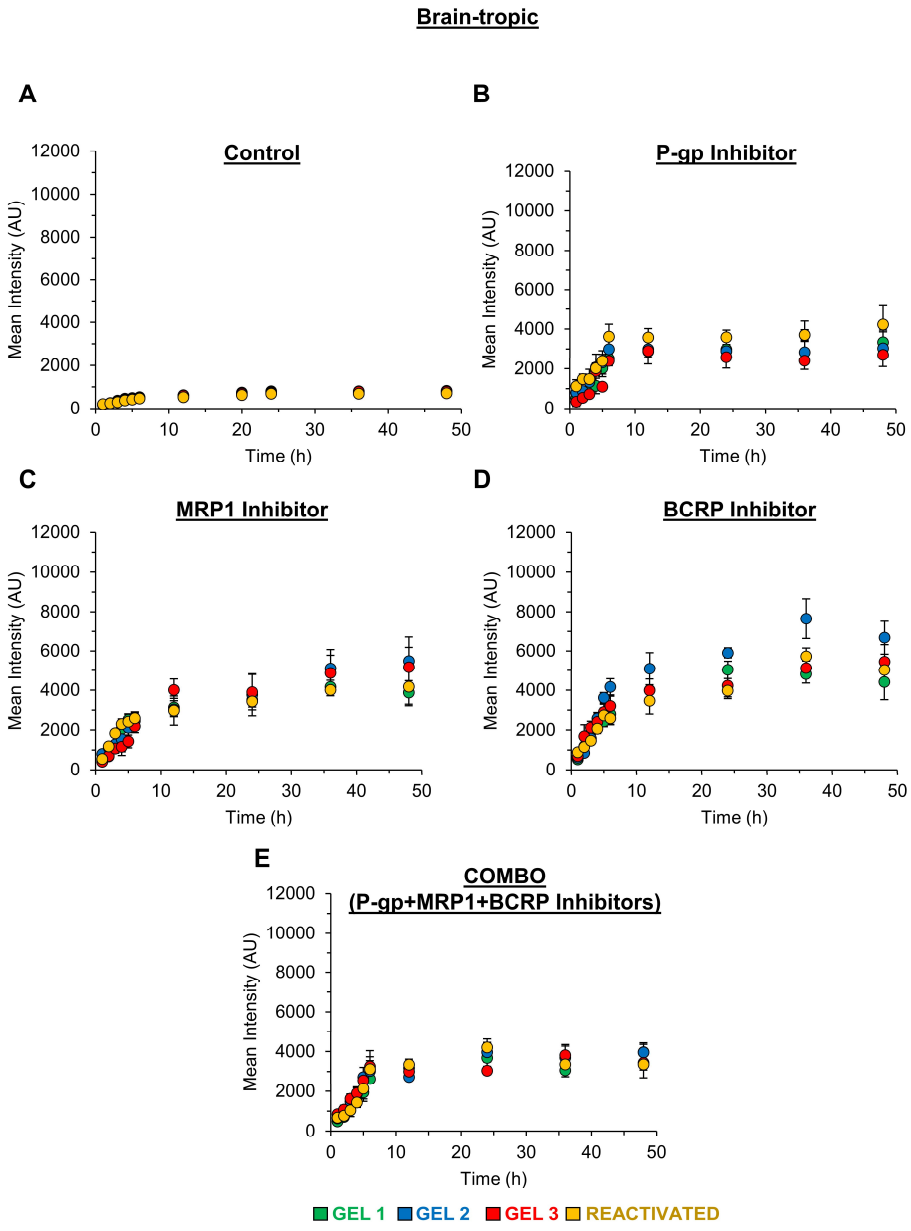

Figure 5.12: Doxorubicin Accumulation on Brain-tropic Cells. Quantification of doxorubicin (0.05 mM) accumulation in BrM2a-831s (brain-tropic) with (A) no inhibitor, (B) P-gp inhibitor (10 nM tariquidar), (C) MRP1 inhibitor (50 µM MK571), (D) BCRP inhibitor (10 µM Ko 143), or (E) a combination of all three inhibitors over 48 h via fluorescence intensity. Value represent mean ± standard deviation.

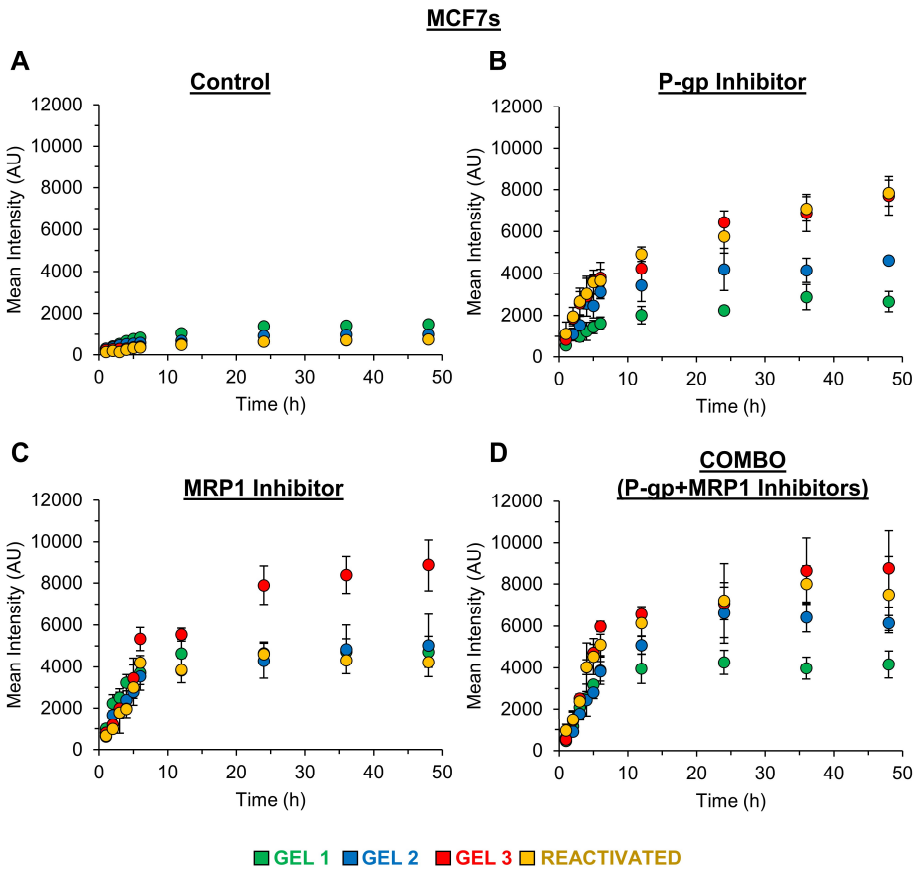

Figure 5.13: Doxorubicin Accumulation on MCF7s. Quantification of doxorubicin (0.05 mM) accumulation in MCF7s with (A) no inhibitor, (B) P-gp inhibitor (10 nM tariquidar), (C) MRP1 inhibitor (50 µM MK571), or (D) a combination of both inhibitors over 48 h via fluorescence intensity. Value represent mean ± standard deviation.

Results showed that P-gp inhibition increased the DOX accumulation rate from 112.8 ± 10.1 to 515.77 ± 51.8 h^{-1} in permissive gel 1 (~5-fold increase),100.5 ± 7.7 to 428.4 ± 33.6 h^{-1} in non-permissive gel 2 (~4-fold increase), 97.2 ± 9.4 to 513.5 ± 38.7 h^{-1} in non-permissive gel 3 (~5-fold increase), and 76.63 ± 1.7 to 645.3 ± 94.9 h^{-1} in reactivated parental 231s (~8-fold increase) (Figure 5.11, 5.14, 55.15). Accumulation

rate in reactivated parental 231s was significantly greater than both dormant (non-permissive gels 2 and 3) and growing cells (permissive gel 1) with P-gp inhibition. MRP1 (permissive gel 1: 570.7 ± 47 h^{-1} (~5-fold increase), non-permissive gel 2: 825.2 ± 39.5 h^{-1} (~8-fold increase), non-permissive gel 3: 662.9 ± 88.2 h^{-1} (~7-fold increase), reactivated: 696.6 ± 113.3 h^{-1} (~9-fold increase)), and BCRP inhibition (permissive gel 1: 463.8 ± 35.5 h^{-1} (~4-fold increase), non-permissive gel 2: 791.6 ± 80.6 h^{-1} (~8-fold increase), non-permissive gel 3: 541.4 ± 84.7 h^{-1} (~6-fold increase), reactivated: 484.9 ± 61.0 h^{-1} (~6-fold increase)) also increased accumulation rates significantly (Figure 5.11, 5.14). Interestingly dormant cells in non-permissive gel 2 had the greatest accumulation rate in both conditions. Combining all three inhibitors further increased the accumulation rate to 484.3 ± 40.0 h^{-1} (permissive gel 1) (~4-fold increase), 453 ± 73.1 h^{-1} (non-permissive gel 2) (~4-fold increase), 678.7 ± 101.6 h^{-1} (non-permissive gel 3) (~7-fold increase), and 497.52 ± 50.5 h^{-1} (reactivated) (~6-fold increase). Furthermore, dormant cells in non-permissive gel 3 had the greatest accumulation rate, while all other conditions showed no significant difference in the accumulation rate under P-gp+MRP1+BCRP inhibition.

Similar trends were observed in brain-tropic 231s with significant increases in accumulation rates via P-gp inhibition (permissive gel 1: 378.4 ± 39.9 h^{-1} (~3-fold increase), non-permissive gel 2: 487.5 ± 77.7 h^{-1} (~5-fold increase), non-permissive gel 3: 340.7 ± 17.9 h^{-1} (~4-fold increase), reactivated: 553.0 ± 64.5 h^{-1} (~7-fold increase)), MRP1 inhibition (permissive gel 1: 460.3 ± 16.5 h^{-1} (~4-fold increase), non-permissive gel 2: 422.2 ± 56.8 h^{-1} (~4-fold increase), non-permissive gel 3: 329.6 ± 33.9 h^{-1} (~4-fold increase), reactivated: 497.0 ± 11.8 h^{-1} (~6-fold increase)), BCRP inhibition (permissive gel 1: 509.9 ± 40.1 h^{-1} (~5-fold increase), non-permissive gel 2:

664.5 ± 32.1 h^{-1} (~7-fold increase), non-permissive gel 3: 591.0 ± 50.5 h^{-1} (~6-fold increase), reactivated: 494.7 ± 60.1 h^{-1} (~6-fold increase)), and P-gp+MRP1+BCRP inhibition (permissive gel 1: 420.5 ± 22.2 h^{-1} (~4-fold increase), non-permissive gel 2: 510.5 ± 46.1 h^{-1} (~5-fold increase), non-permissive gel 3: 525.0 ± 65.0 h^{-1} (~6-fold increase), reactivated: 444.7 ± 45.7 h^{-1} (~6-fold increase)) (Figure 5.12, 5.14, 5.15). Furthermore, inhibition of all three efflux pumps, led to significantly greater accumulation rate in dormant brain-tropic cells (non-permissive gels 2 and 3) compared to growing (permissive gel 1) and reactivated cells.

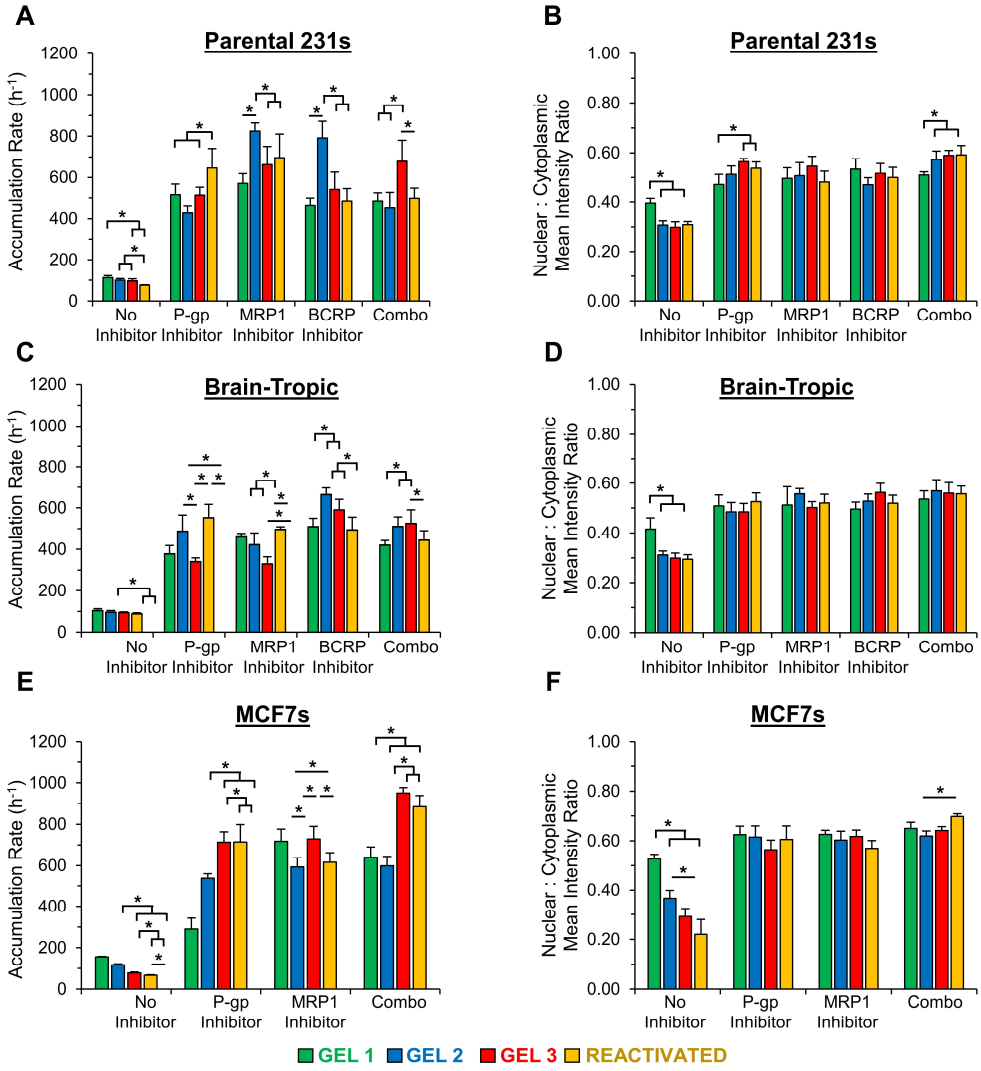
A
Parental 231s
Accumulation Rate (h-1)
1200
1000
800
600
400
200
0
No Inhibitor
P-gp Inhibitor
MRP1 Inhibitor
BCRP Inhibitor
Combo
B
Parental 231s
Nuclear : Cytoplasmic Mean Intensity Ratio
1.00
0.80
0.60
0.40
0.20
0.00
C
Brain-Tropic
D
Brain-Tropic
E
MCF7s
F
MCF7s
GEL 1
GEL 2
GEL 3
REACTIVATED

Figure 5.14: Influence of Efflux Pump Inhibition on Doxorubicin Accumulation and Localization in Dormant and Reactivated Cells. Quantification of doxorubicin (0.05 mM) accumulation rate in (A) MDA-MB-231s (parental 231s), (C) BrM2-831s (brain-tropic) sublines, and (E) MCF7s with no inhibitor, P-gp inhibitor (10 nM tariquidar), MRP1 inhibitor (50 μM MK571), BCRP inhibitor (10 μM Ko 143), or a combination of all inhibitors over 48 h via fluorescence intensity. Quantification of nuclear to cytoplasmic localization of doxorubicin (0.05 mM, 48h) in (B) MDA-MB-231s (parental 231s), (D) BrM2-831s (brain-tropic) sublines, and (F) MCF7s with no inhibitor, P-gp inhibitor (10 nM tariquidar), MRP1 inhibitor (50 μM MK571), BCRP inhibitor (10 μM Ko 143), or a combination of all inhibitors over 48 h via fluorescence intensity. * indicates $p < 0.05$ determined by a one-way ANOVA. n = 6 (accumulation) or 4 (localization) z-stacks from six individual hydrogels in (A, C, E) Values represent mean + standard deviation.

In MCF7s, P-gp inhibition increased accumulation rate by ~3-fold in cells in the growth state cultured in permissive gel 1 (290.1 ± 52.8 h^{-1}), ~5-fold in non-permissive gel 2 (537.9 ± 22.2 h^{-1}), ~7-fold in non-permissive gel 3 (713.4 ± 49.6 h^{-1}), and ~9-fold in reactivated cells (714.5 ± 84.6 h^{-1}) (Figure 5.12-5.14). Additionally, P-gp inhibition led to significantly greater accumulation rates in dormant (non-permissive gels 2 and 3) and reactivated cells compared to growing cells in permissive gel 1. MRP1 inhibition further increased accumulation rate in permissive gel 1 by ~6-fold (718.3 ± 58.1 h^{-1}) and led to similar increases in non-permissive gel 2 (~6-fold increase, 593.6 ± 44.5 h^{-1}), non-permissive gel 3 (~7-fold increase, 728.9 ± 60.6 h^{-1}), and reactivated cells (~8-fold increase, 616.6 ± 45.9 h^{-1}). Finally, inhibition of both P-gp+MRP1 led to significantly higher accumulation rates in dormant cells in non-permissive gel 3 (~10-fold increase, 951.0 ± 26.9 h^{-1}) and reactivated cells (~11-fold increase 884.4 ± 54.8 h^{-1}), compared to growing cells in permissive gel 1 (~6-fold

increase, 640.4 ± 50.3 h^{-1}), and dormant cells in non-permissive gel 2 (~6-fold increase, 599.3 ± 45.4 h^{-1}).

Taken together, this data indicates that efflux pump inhibition significantly increases both chemosensitivity to DOX and DOX accumulation rate in parental 231s, brain-tropic 231s, and MCF7s. This suggests that dormant and reactivated cells attain chemoresistance via efflux pumps that expel DOX out of the cell, and inhibiting this process significantly increases drug efficacy.

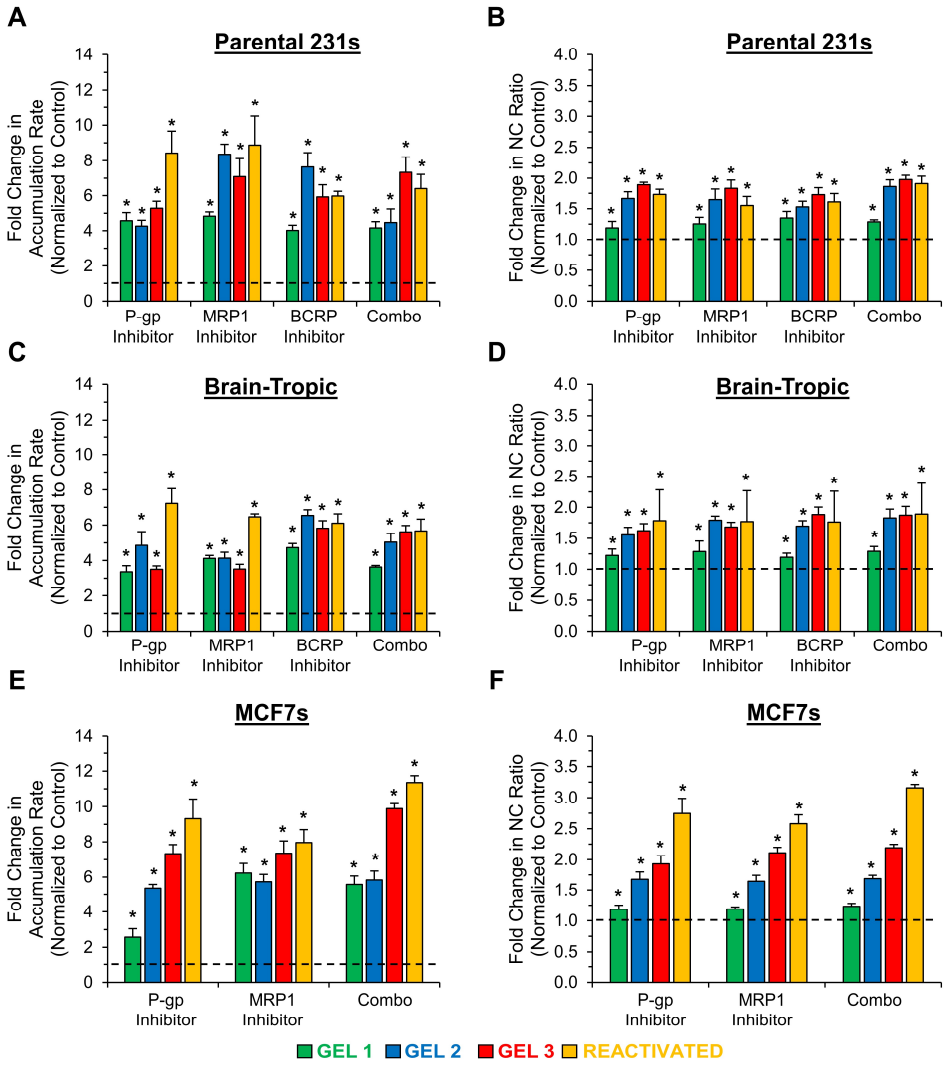

Figure 5.15: Fold-Change in Doxorubicin Accumulation and Localization in Dormant and Reactivated Cells with Efflux Pump Inhibition. (A, C, E) Fold-change in accumulation rate and (B, D, F) nuclear: cytoplasmic intensity ratio of MDA-MB-231s (parent 231), BrM2a-831s (brain-tropic), and MCF7s with P-gp inhibitor (10 nM tariquidar), MRP1 inhibitor (50 µM MK571), BCRP inhibitor (10 µM Ko 143), or a combination of all inhibitors with 0.05 mM doxorubicin over 48 h, normalized to no inhibitor. * indicates $p < 0.05$ determined by a one-way ANOVA. $n = 6$ (accumulation) or 4 (localization) z-stacks from individual hydrogels. Values represent mean + standard deviation.

5.3.4 Influence of P-gp, MRP1, BCRP Inhibition in Doxorubicin Localization

As shown in chapter 4, nuclear localization is significantly higher in growing cells in permissive gel 1 compared to dormant (non-permissive gels 2 and 3) and reactivated cells for all cell lines tested. To determine if efflux pump inhibition altered DOX localization to the nucleus, cells were exposed to each inhibitor (P-gp inhibitor (10 nM tariquidar), MRP1 inhibitor (50 μM MK571), BCRP inhibitor (10 μM Ko 143), or a combination of all three) for 24 h, followed by 0.05 mM of DOX+inhibitor for 48 h. Nuclear and cytoplasmic DOX intensity was then measured and compared to determine NC ratio as described in chapter 4.

In parental 231s, results indicate that P-gp, MRP1, BCRP, and P-gp+MRP1+BCRP inhibition significantly increased NC ratio for all formulations (Figure 5.14, 5.15). For instance, P-gp inhibition increased the NC ratio from 0.40 ± 0.02 to 0.47 ± 0.04 in permissive gel 1, 0.31 ± 0.02 to 0.51 ± 0.03 in non-permissive gel 2, 0.30 ± 0.02 to 0.56 ± 0.01 in non-permissive gel 3, and 0.31 ± 0.01 to 0.54 ± 0.03 in reactivated cells, resulting in significantly higher nuclear localization in dormant cells in non-permissive gel 3 and reactivated cells, compared to growing and dormant cells in non-permissive gel 2. Under MRP1 (permissive gel 1: 0.50 ± 0.04, non-permissive gel 2: 0.51 ± 0.05, non-permissive gel 3: 0.55 ± 0.04, reactivated: 0.48 ± 0.04) and BCRP inhibition (permissive gel 1: 0.53 ± 0.04, non-permissive gel 2: 0.47 ± 0.03, non-permissive gel 3: 0.52 ± 0.04, reactivated: 0.50 ± 0.04) NC ratios also increased to the extent that there were no significant differences between growing (permissive gel 1), dormant (non-permissive gels 2 and 3), and reactivated cells. Inhibiting all three efflux pumps, went beyond increasing nuclear localization levels in dormant and reactivated cells to that of growing cells; instead, dormant (non-permissive gels 2 and 3) and reactivated cells displayed significantly greater NC ratios

than growing cells in permissive gel 1 (permissive gel 1: 0.51 ± 0.01, non-permissive gel 2: 0.57 ± 0.03, non-permissive gel 3: 0.59 ± 0.02, reactivated: 0.59 ± 0.04).

Brain-tropic cells showed similar trends, with P-gp, MRP1, BCRP, and P-gp+MRP1+BCRP inhibition all increasing NC ratios and leading to no significant differences between growing, dormant (non-permissive gels 2 and 3), and reactivated cells: P-gp inhibition: permissive gel 1: 0.51 ± 0.04, non-permissive gel 2: 0.48 ± 0.04, non-permissive gel 3: 0.48 ± 0.03, reactivated: 0.53 ± 0.04, MRP1 inhibition: permissive gel 1: 0.51 ± 0.07, non-permissive gel 2: 0.56 ± 0.02, non-permissive gel 3: 0.50 ± 0.02, reactivated: 0.52 ± 0.03, BCRP inhibition: permissive gel 1: 0.50 ± 0.03, non-permissive gel 2: 0.53 ± 0.03, non-permissive gel 3: 0.56 ± 0.04, reactivated: 0.52 ± 0.03, combo: permissive gel 1: 0.54 ± 0.03, non-permissive gel 2: 0.57 ± 0.05, non-permissive gel 3: 0.56 ± 0.04, reactivated: 0.56 ± 0.03 (Figure 5.14, 5.15).

MCF7s had the greatest difference in NC ratio with significant differences observed both between growing (permissive gel 1: 0.53 ± 0.02), dormant (non-permissive gel 2: 0.37 ± 0.03, non-permissive gel 3: 0.29 ± 0.03), and reactivated MCF7s (0.22 ± 0.06), as well as between dormant cell in non-permissive gel 2 and reactivated cells (Figure 5.13, 5.14). Under P-gp inhibition, NC ratio increased to 0.62 ± 0.03 in permissive gel 1, 0.61 ± 0.05 in non-permissive gel 2, 0.56 ± 0.04 in non-permissive gel 3, and 0.61 ± 0.05 in reactivated cells. Under MRP1 inhibition, NC ratio increased to 0.63 ± 0.02 in permissive gel 1, 0.60 ± 0.04 in non-permissive gel 2, 0.62 ± 0.03 in non-permissive gel 3, 0.57 ± 0.03 in reactivated cells. Both P-gp and MRP1 inhibition increased NC ratios in dormant (non-permissive gels 2 and 3) and reactivated cells to the extent that there were no longer any significant differences compared to growing cells in permissive gel 1. When inhibiting both P-gp and MRP1

together, NC ratios similarly increased in growing (0.65 ± 0.02 in permissive gel 1) and dormant cells (non-permissive gel 2: 0.62 ± 0.02, non-permissive gel 3: 0.64 ± 0.02) with no significant differences between the three formulations, however there was significantly greater localization in reactivated cells compared to all other formulations (0.70 ± 0.01).

This data indicates that inhibiting P-gp, MRP1, and BCRP can increase the amount of DOX that both makes it into the cell and localizes to the nucleus. Furthermore, while this inhibition increased localization in all phenotypic states, growing cells no longer displayed significantly greater NC ratios, instead in some cases dormant or reactivated cells now had significantly greater nuclear localization. Along with dose-response and accumulation data, these findings suggest that dormant and reactivated cells use efflux pumps to reduce DOX intracellular accumulation and nuclear localization. Inhibition of these efflux pumps increases drug accumulation and localization, and overall efficacy, providing a potential therapeutic strategy to target and eliminate dormant and reactivated cells to help prevent metastatic relapse.

5.4 Discussion and Conclusion

Cancer latency, during which cells lie dormant, can last up to decades before residual cells become reactivated and resume growth.[3,4] This period provides a crucial window of time that may be used to treat and eliminate dormant cells before they begin to form overt lesions that lead to poor patient outcome. In order to develop new drugs and therapeutic strategies to target dormant cells and prevent metastatic relapse, we developed an *in vitro* hydrogel platform that mimics a permissive niche (permissive gel 1 (++ adhesivity, ++ degradability)), and two non-permissive niches (non-permissive gel 2 (+ adhesivity, + degradability), and non-permissive gel 3 (-

adhesivity, ++ degradability) (chapters 2 and 3). Parental 231s, 3 organotropic sublines, and MCF7s were each encapsulated in each gel type for 15 days, and multimetric analysis based on dormancy-associated phenotypic changes characterized hydrogel-induced phenotype to be either in growth (in permissive gel 1), balanced cellular dormancy, balanced tumor mass dormancy, or restricted survival dormancy (in non-permissive gels 2 or 3). Cells in non-permissive gel 3 were reactivated via matrix modulation by adding RGDS into the matrix at day 15 and culturing cells for an additional 7 days (22 days total) (chapter 3). With an established dormancy and reactivation platform, we quantified dormant and reactivated cell chemoresponse in all five cell lines and found that dormant (non-permissive gels 2 and 3) and reactivated cells showed significantly greater chemoresistance to DOX, determined by EC_{50} and IC_{50} values (chapter 4). These results were further confirmed by findings that indicated DOX accumulation rate and nuclear localization were significantly lower in dormant (non-permissive gels 2 and 3) and reactivated cells compared to growing cells in permissive gel 1, suggesting that DOX transport may play a significant role in observed chemoresistance. This chapter focused on determining which factors influence DOX transport and ultimate chemoresistance to develop a potential strategy to increase efficacy in dormant and reactivated cells.

To investigate DOX transport, we focused on ABC efflux transporters, which belong to a superfamily of proteins known to actively transport biomolecules out of a cell.[131] Furthermore, ABC efflux transporters have been established as key components in multi-drug resistance. For instance, ABC transporters have been shown to reduce drug accumulation[135,136] and their overexpression has been linked to aggressive tumor progression and poor patient outcome. This study investigated the

role of three ABC efflux exporters that are widely associated with cancer chemoresistance: P-gp, MRP1, and BCRP. P-gp is a membrane-associated glycoprotein which excretes substrates including cytotoxic drugs.[47,137,138] Furthermore, it is overexpressed in chemotherapy-resistant tumors and is associated with disease progression in many cancers including breast cancer.[47] Studies have also shown P-gp overexpression in multi-drug resistance cell lines decreases both drug accumulation in the cytoplasm and the nucleus.[139] MRP1 (ABCC1) is primarily found in the basolateral membrane of epithelial cells of multiple organs including lung, kidney placenta, and others.[49] MRP1 has been correlated with inflammatory, immunological diseases, muscular degeneration, cardiovascular disease, and neurological disorders, has shown elevated expression in solid tumors.[48,140,141] Furthermore, MRP1 expression has been associated with drug resistance and poor clinical outcome.[49,142] BCRP (ABCG2) is a homodimer on cellular plasma membranes present in both cancer cells and normal tissues including cells in the mammary gland epithelium and hepatocytes.[51] As other efflux pumps, its role lies in the extrusion of substrates including drugs. BCRP also plays a role in urate transportation and is found in the mammary gland epithelium, hepatocytes, and in the blood brain barrier.[51] It plays a prominent role in chemoresistance,[143-145] with its overexpression correlated to cancer cell resistance to mitoxantrone, doxorubicin, SN-38, and others.[51] Studies have shown that inhibition of these efflux pumps decreases chemoresistance and increases overall drug efficacy.[132-134]

To determine if ABC efflux pumps associated with multidrug resistance were differentially expressed in chemosensitive growing cells (permissive gel 1) and chemoresistant dormant (non-permissive gels 2 and 3) and reactivated cells, parental

231s, organotropic sublines, and MCF7s were individually encapsulated in permissive gel 1, non-permissive gel 2, or non-permissive gel 3 and cultured for 15 days to achieve a growth or dormant state. To also investigate reactivated cells, dormant cells in non-permissive gel 3 were reactivated via RGDS incorporation and further cultured for 7 days (total 22 days). Cells were then fixed and labeled for P-gp, MRP1, or BCRP, and counterstained to label cell nuclei and cytoskeleton (Figure 5.1-5.5). Efflux pump expression was measured by quantifying mean intensity per cell. In the parental line, results showed significantly higher P-gp expression in dormant 231s in non-permissive gel 3, compared to other formulations. Parental 231s also showed significantly higher MRP1 and BCRP expression in chemoresistant dormant (non-permissive gels 2 and 3) and reactivated cells compared to growing cells in permissive gel 1. Organotropic lines also displayed significantly greater efflux pump expression for P-gp, MRP1, and BCRP in chemoresistant dormant and reactivated cells. Lastly, MCF7s indicated significant differences for P-gp and MRP1, but not BCRP. Overall, these results indicated that chemoresistant dormant and reactivated cells had higher efflux pump expression, suggesting efflux pumps may play a role in acquired chemoresistance.

The role of efflux pumps in multidrug resistance has been further investigated using efflux pump inhibitors and quantifying subsequent drug response. P-gp inhibitors have been widely studied, with 3 classes or generation of inhibitors currently established.[146,147] First generation inhibitors were approved therapeutics that also function to inhibit P-gp, including compounds such as verapamil, quinine, quinidine, and cyclosporine A. However, these inhibitors failed in clinical trials as high concentrations required for inhibition had adverse side effects. Generation 2

inhibitors were designed for P-gp inhibition and were more effective but required concentrations remained high and often interfered with pharmacokinetics of other drugs.[147] Third generation inhibitors like tariquidar have been most effective, with high P-gp affinity at lower concentrations.[148] Other efflux pumps including BCRP have also been inhibited. BCRP inhibitor, Ko 143 has been shown to display >200-fold selectivity for BCRP, compared to P-gp and MRP1, and has been shown to increase intracellular drug accumulation to reverse BCRP-mediated multidrug resistance both *in vitro* and *in vivo*.[134,149] Similarly, MRP1 inhibitor, MK571 has shown promising results *in vitro* and *in vivo*, showing the ability to significantly increase drug efficacy.[150,151]

To determine whether differential efflux expression played a role in chemoresistance in dormant and reactivate breast cancer, drug studies were conducted using P-gp inhibitor (10 nM tariquidar), MRP1 inhibitor (50 μM MK571), BCRP inhibitor (10 μM Ko 143), or a combination of all three. Concentrations were chosen based on inhibitor *in vitro* IC_{50} values (tariquidar: 5.1 nM, MK571: 3.5 μM, Ko 143: 26 nM)[152,153] and experiments performed by other groups.[154,155] Furthermore, tariquidar concentration was also kept below 100 nM, as higher concentrations >100 nM have shown to inhibit both P-gp and BCRP.[156] While these concentrations were used in this study, a larger study testing out an array of concentrations would be required to find the optimal doses in future studies.

Parental 231s, brain-tropic, or MCF7s were encapsulated in each formulation and cultured to day 15 or 22 were exposed to each inhibitor condition for 24 h, followed by DOX+inhibitor for 48 h. Results showed that efflux pump inhibition significantly increased chemosensitivity, indicated by significant decreases in EC_{50}

values (Figure 5.8, 5.9). To assure the inhibitor alone had no cytotoxic affect, viable cell number was compared between control groups (media) and inhibitor controls (media + inhibitor (no DOX)) (Figure 5.7). Results indicated no significant differences in the number of viable cells with or without inhibitor, assuring that efflux pump inhibition had no cytotoxic affects.

In parental 231s, P-gp inhibition alone decreased EC_{50} values, however dormant and reactivated cells still displayed significantly greater chemoresistance (EC_{50} ~ 23-38 μM) compared to growing cells in permissive gel 1 (EC_{50}: 9.5 ± 0.8 μM) (Figure 5.9). However, MRP1, BCRP, and P-gp+MRP1+BCRP inhibition decreased dormant and reactivated EC_{50} values significantly below those for permissive gel 1. Brain-tropic cells showed similar trend overall, with the greatest change observed in P-gp+MRP1+BCRP inhibition in which EC_{50} values decreased from 44.9 ± 6.2 to 2.7 ± 0.6 μM (17-fold decrease) in permissive gel 1, 65.5 ± 7.7 to 2.5 ± 0.5 μM (~26-fold) in non-permissive gel 2, 85.7 ± 14.4 to 1.4 ± 0.4 μM (~61-fold) in non-permissive gel 3, and 113.0 ± 15.7 to 2.3 ± 0.3 μM (~40-fold decrease) in reactivated cells (Figure 5.9). In MCF7s, inhibition of both P-gp and MRP1 dropped EC_{50} values to 1.7 ± 0.4 μM (permissive gel 1), 0.5 ± 0.1 μM (non-permissive gel 2), 0.6 ± 0.1 μM (non-permissive gel 3), and 1.0 ± 0.2 μM (reactivated). Additionally, P-gp and MRP1 inhibition increased dormant (non-permissive gels 2 and 3) and reactivated cell chemosensitivity to levels exceeding growing cells in permissive gel 1 (Figure 5.9). To determine if increased efficacy correlated with DOX transport during efflux inhibition, DOX accumulation and nuclear localization during efflux pump inhibition were quantified. Results showed significant increases in both accumulation rates and NC ratio (Figure 5.14, 5.15). Furthermore, the accumulation rates were

significantly higher in dormant and reactivated cells in certain cases including P-gp+MRP1 inhibition in MCF7s. Additionally, efflux pump inhibition increased nuclear localization in dormant and reactivated cells to levels observed in growing cells in permissive gel 1 for parental 231s, brain-tropic 231s, and MCF7s.

These findings indicate that inhibiting efflux pumps, P-gp, MRP1, and BCRP increases DOX intracellular accumulation rate and nuclear localization, leading to increased drug efficacy. This suggests that dormant and reactivated cells use efflux pumps as a mechanism to limit drug intake and evade cytotoxicity. We cannot rule out the possibility that dormant cells use other breast cancer resistance-associated mechanisms including tumor suppressor genes, oncogenes, autophagy, mitochondrial alteration, EMT, cancer stemness, and others.[130] As many of these mechanisms work together to decrease drug toxicity, it is possible that dormant and reactivated cells employ multiple methods to decrease drug efficacy, and this should be explored in future studies. However, results indicate that efflux pump inhibition is sufficient to significantly increase EC_{50} values for five different breast cancer lines and diminish any dormant or reactivated-associated chemoresistance, compared to growing cells in permissive gel 1. Future implementation of this work can be used as a novel treatment strategy to target and inhibit these efflux pumps in dormant and reactivated cells *in vivo*. Taken together, this data provides insight into the mechanisms used by dormant and reactivated cells to resist DOX cytotoxicity and lays the groundwork for a novel treatment strategy to target dormant and reactivated cells and help prevent metastatic relapse.

Chapter 6

CONCLUSIONS AND FUTURE DIRECTIONS

Sections in this chapter have been adapted from the following articles:

(1) Farino CJ, Pradhan S, Slater JH. The Influence of Matrix-Induced Dormancy on Metastatic Breast Cancer Chemoresistance. ACS Applied Biomaterials 2020, 3(9), 5832-5844.

(2) Farino Reyes CJ, Pradhan S, Slater JH. The Influence of Ligand Density and Degradability on Hydrogel Induced Breast Cancer Dormancy and Reactivation. Advanced Healthcare Materials 2021, 10(11), 2002227.

6.1 Summary of Key Findings

Novel treatment strategies that target dormant cells can make significant strides in preventing metastasis and cancer progression. Toward this goal, mechanistic investigation of microenvironmental factors influencing cancer cell fate can help in understanding how cancer dormancy is initiated and maintained and highlight the underlying factors mediating the latency period that is commonly observed prior to metastatic relapse. *In vitro* models can provide a platform to perform these studies and screen new therapeutic strategies that target dormant cells and help prevent cancer recurrence.

In chapters 2 and 3, we characterize a hydrogel-based *in vitro* system that mimics favorable and unfavorable ECMs that DTCs may experience during early stages of infiltration into secondary organs. Implementing a permissive gel (++

adhesivity, ++ degradability), a non-permissive gel 2 (+ adhesivity, + degradability), and a non-permissive gel 3 (- adhesivity, ++ degradability), chapter 3 demonstrated the ability to achieve growth, distinct forms of dormancy, and reactivation in parental 231s, organotropic sublines, and ER^+ MCF7s. Studies in chapter 4 implemented this platform to quantify drug-response and found that dormant and reactivated cells exhibit increased chemoresistance compared to growing cells, in part due to DOX transport properties, including significantly lower accumulation rates and nuclear localization.

Lastly, chapter 5 investigated the mechanisms that regulate DOX transport and overall chemoresistance. Results found that chemoresistant dormant and reactivated cells had significantly greater efflux pump expression. Inhibition of these efflux pumps significantly increased chemosensitivity to DOX and increased intracellular DOX accumulation rate and nuclear localization. Overall, this work developed a hydrogel platform to induce dormancy and reactivation in five relevant breast cancer lines and has the potential to induce dormancy in other cancers known to have similar latency periods. This work also provides insight into the mechanisms used by dormant and reactivated cells to resist DOX cytotoxicity and lays the groundwork for a novel treatment strategy to target dormant and reactivated cells and help prevent metastatic relapse. Suggestions for future studies and implementation of this work are listed below.

6.2 Future Directions

6.2.1 Gene Expression Analysis

As mentioned in chapter 3, dormancy-associated phenotypic changes were determined via multi-metric analysis to classify hydrogel-induced phenotype. Phenotypic metrics can indicate observable hydrogel-induced traits; however, they do not provide information regarding ECM-induced genetic changes. Groups that have performed gene analysis in dormant cells have shown differential expression involved in a multitude of cellular processes including cell cycle regulation, developmental processes, motility, and differentiation.[69] Understanding the genetic differences between growing, dormant, and reactivated cells could provide insight into the mechanisms that regulate dormancy. Furthermore, genetic differences between growing and reactivated cells can be used to explain reactivated cell chemoresistance. Unique genetic signatures can be further implemented to develop new methods that target and eliminate dormant cells.

6.2.2 Inducing Dormancy and Reactivation in Patient-Derived Cells

In this work, we show the ability to induce growth, dormancy, and reactivation in five breast cancer cell lines: triple negative parental 231s, organotropic sublines that preferentially metastasize to the bone, lung, or brain, and ER^+ MCF7s. The logic for these cell lines is explained in chapter 3. Briefly, investigation of the parental 231 line and its organotropic sublines provides insight into how genetically unique organotropic lines respond to unfavorable conditions, while investigation of ER^+ MCF7s is clinically relevant as ER^+ breast cancer is more likely to enter dormancy and remain in dormancy for longer periods of time. Transition into a clinical setting requires that future studies quantify the ability to induce dormancy and reactivation in

patient-derived cells with clinically relevant receptor status and genotype. For instance, in selecting ER^+ patient derived cells, the Oncotype DX genomic test can be used to select cells with high probability of metastasis with a high-risk recurrence score (score ≥ 31 is high risk[157]), based on the expression of 21 genes (Ki67, STK15, Survivin, CCNB1, MYBL2, MMP11, Stromolysin 3, CTSL2, GRB2, HER2, ER, PGR, BCL2, SCUBE2, GSTM1, CD68, BAG1, ACTB, GAPDH, RPLPO, GUS, TFRC) associated with recurrence.

6.2.3 Incorporation of Other Dormancy-Inducing Methods

In this work, we focused on ECM-induced dormancy to understand how tuning matrix adhesivity and degradability can influence cancer cell phenotype. As described in chapter 3, other methods including signaling-induced dormancy, biochemical-induced dormancy, and drug-induced dormancy have been used to model dormancy *in vitro*. Future studies that optimize conditions can be conducted to include these additional factors in a controlled manner. For instance, experiments that include hypoxic conditions can be conducted in the current system, or secondary cell types such as fibroblasts or immune cells can be included through careful experimental design. These studies could highlight how multiple factors influence phenotype compared to the ECM alone.

6.2.4 Improvements to Current Platform

A limitation of our current polymerization scheme is that hydrogel degradability and elasticity are coupled. Future studies that implement a multi-arm PEG chemistry can provide independent control over these parameters. [87-90] Another modification that can made to the system includes using organ-mimetic peptides to

capture unique organ-specific ECM-induced changes. Finally, while current fabrication methods are fairly simple and easy to use, finding new methods to increase throughput in both encapsulation and imaging will aid in the clinical translation to a drug development platform.

6.2.5 Efflux Pump Inhibition in Dormant and Reactivated Cells

Chapters 4 and 5 provide valuable insight into dormant and reactivated cell chemoresistance, showing that dormant and reactivated cells exhibit increased DOX chemoresistance compared to growing cells in permissive gel 1, with significantly lower DOX accumulation rates and nuclear localization. Furthermore, chapter 5 showed that inhibition of efflux pumps, P-gp, MRP1, and BCRP significantly reduces chemoresistance, accompanied by significant increases in accumulation rate and localization. This provides a treatment strategy to increase DOX efficacy in hydrogel-induced dormancy and reactivation *in vitro*. To build on this work, future studies that investigate efflux inhibition influence on chemoresistance on other commonly used chemotherapeutics such as PAC or 5-FU should be conducted. Additionally, a wider range of concentrations can be tested to optimize treatment conditions. If similar resistance is attained, *in vivo* studies that demonstrate the ability to target dormant cells will be crucial.

6.3 Significance

Metastasis is responsible for most cancer-associated deaths and significantly decreases patient-survival rates. Commonly observed prior to relapse is a latency period that can last up to decades,[4] that is regulated by tumor dormancy in which cancer cells remain clinically undetectable. The danger arises when dormant cells

become reactivated and resume growth, leading to overt lesions and cancer recurrence. We can take advantage of this latency period as a therapeutic "window of opportunity" to eliminate dormant cells prior to reactivation. However, current chemotherapeutics fail to target dormant cells. Thus, to aid in the development of drugs that eliminate dormant cells, we developed a hydrogel platform that can induce both dormancy and reactivation in five relevant breast cancer cell lines. This platform can aid in making significant strides towards metastasis prevention as it provides the resolution to perform single cell mechanistic studies, dynamic control over hydrogel properties, and models metastatic relapse, a key transition that can be further studied to prevent exit out of dormancy *in vivo*.

To aid in understanding dormancy-associated chemoresistance, this platform was implemented to quantify increased chemoresistance in dormant and reactivated cells and demonstrated decreased DOX intracellular concentration and nuclear localization and chemoresistant dormant and reactivated cells. These novel findings provided insight that was further explored to determine the role of efflux pumps, P-gp, MRP1, and BCRP, in DOX efficacy and transport. Studies confirmed that chemoresistant dormant and reactivated cells overexpressed these efflux pumps and that their inhibition increased chemosensitivity via increased accumulation rate and nuclear localization. This work provides significant strides towards the goal to eliminate dormant cells and prevent metastatic relapse as it provides a potential mechanism involved in chemoresistance and provides a method to target dormant and reactivated cells *in vitro* that can be further tested *in vivo*.

REFERENCES

1 Cancer Facts & Figures 2019. American Cancer Society. (2019).

2 Chaffer, C. L. & Weinberg, R. A. A perspective on cancer cell metastasis. *Science (New York, N.Y.)* **331**, 1559-1564, doi:10.1126/science.1203543 (2011).

3 Aguirre-Ghiso, J. A. Models, mechanisms and clinical evidence for cancer dormancy. *Nature reviews. Cancer* **7**, 834-846, doi:10.1038/nrc2256 (2007).

4 Gomis, R. R., Gawrzak S. Tumor cell dormancy. *Molecular Oncology*, 62-78 (2017).

5 Weidenfeld, K. & Barkan, D. EMT and Stemness in Tumor Dormancy and Outgrowth: Are They Intertwined Processes? *Frontiers in oncology* **8**, 381, doi:10.3389/fonc.2018.00381 (2018).

6 Luzzi, K. J., MacDonald, I. C., Schmidt, E. E., Kerkvliet, N., Morris, V. L., Chambers, A. F., Groom, A. C. Multistep nature of metastatic inefficiency: dormancy of solitary cells after successful extravasation and limited survival of early micrometastases. *Am J Pathol* **153**, 865-873, doi:10.1016/s0002-9440(10)65628-3 (1998).

7 Pradhan, S., Sperduto, J. L., Farino, C. J. & Slater, J. H. J. J. o. B. E. Engineered In Vitro Models of Tumor Dormancy and Reactivation. **12**, 37, doi:10.1186/s13036-018-0120-9 (2018).

8 Meng, S. T., D., Frenkel, E. P., Shete, S., Naftalis, E. Z., Huth, J. F., Beitsch, P. D., Leitch, M., Hoover, S., Euhus, D., Haley, B., Morrison, L., Fleming, T. P., Herlyn, D., Terstappen, L. W., Fehm, T., Tucker, T. F., Lane, N., Wang, J., Uhr, J. W. Circulating tumor cells in patients with breast cancer dormancy. *Clinical cancer research : an official journal of the American Association for Cancer Research* **10**, 8152-8162, doi:10.1158/1078-0432.Ccr-04-1110 (2004).

9 Naumov, G. N., MacDonald, I. C., Weinmeister, P. M., Kerkvliet, N., Nadkarni, K. V., Wilson, S. M., Morris, V. L., Groom, A. C., Chambers, A. F. Persistence of solitary mammary carcinoma cells in a secondary site: a possible contributor to dormancy. *Cancer research* **62**, 2162-2168 (2002).

10 Naumov, G. N., Folkman, J., Straume, O., Akslen, L. A. Tumor-vascular interactions and tumor dormancy. *APMIS : acta pathologica, microbiologica, et immunologica Scandinavica* **116**, 569-585, doi:10.1111/j.1600-0463.2008.01213.x (2008).

11 Manjili, M. H. Tumor Dormancy and Relapse: From a Natural Byproduct of Evolution to a Disease State. *Cancer research* **77**, 2564-2569, doi:10.1158/0008-5472.Can-17-0068 (2017).

12 Brackstone, M., Townson, J. L. & Chambers, A. F. Tumour dormancy in breast cancer: an update. *Breast cancer research : BCR* **9**, 208, doi:10.1186/bcr1677 (2007).
13 Bissell, M. J. & Hines, W. C. Why don't we get more cancer? A proposed role of the microenvironment in restraining cancer progression. *Nat Med* **17**, 320-329, doi:10.1038/nm.2328 (2011).
14 Ghajar, C. M., Peinado, H., Mori, H., Matei, I. R., Evason, K. J., Brazier, H., Almeida, D., Koller, A., Hajjar, K. A., Stainier, D. Y., Chen, E. I., Lyden, D., Bissell, M. J. The perivascular niche regulates breast tumour dormancy. *Nat Cell Biol* **15**, 807-817, doi:10.1038/ncb2767 (2013).
15 Braun, S., Kentenich, C., Janni, W., Hepp, F., de Waal, J., Willgeroth, F., Sommer, H., Pantel, K. Lack of effect of adjuvant chemotherapy on the elimination of single dormant tumor cells in bone marrow of high-risk breast cancer patients. *Journal of clinical oncology : official journal of the American Society of Clinical Oncology* **18**, 80-86, doi:10.1200/jco.2000.18.1.80 (2000).
16 Krawczyk, N., Banys, M., Neubauer, H., Solomayer, E. F., Gall, C., Hahn, M., Becker, S., Bachmann, R., Wallwiener, D., Fehm, T. HER2 status on persistent disseminated tumor cells after adjuvant therapy may differ from initial HER2 status on primary tumor. *Anticancer research* **29**, 4019-4024 (2009).
17 Janni, W., Vogl, F. D., Wiedswang, G., Synnestvedt, M., Fehm, T., Juckstock, J., Borgen, E., Rack, B., Braun, S., Sommer, H., Solomayer, E., Pantel, K., Nesland, J., Friese, K., Naume, B. Persistence of disseminated tumor cells in the bone marrow of breast cancer patients predicts increased risk for relapse--a European pooled analysis. *Clinical cancer research : an official journal of the American Association for Cancer Research* **17**, 2967-2976, doi:10.1158/1078-0432.Ccr-10-2515 (2011).
18 Manjili, M. H. The inherent premise of immunotherapy for cancer dormancy. *Cancer research* **74**, 6745-6749, doi:10.1158/0008-5472.Can-14-2440 (2014).
19 Hou, J. M., Krebs, M. G., Lancashire, L., Sloane, R., Backen, A., Swain, R. K., Priest, L. J., Greystoke, A., Zhou, C., Morris, K., Ward, T., Blackhall, F. H., Dive, C. Clinical significance and molecular characteristics of circulating tumor cells and circulating tumor microemboli in patients with small-cell lung cancer. *Journal of clinical oncology : official journal of the American Society of Clinical Oncology* **30**, 525-532, doi:10.1200/jco.2010.33.3716 (2012).
20 Muller, V., Stahmann, N., Riethdorf, S., Rau, T., Zabel, T., Goetz, A., Janicke, F., Pantel, K. Circulating tumor cells in breast cancer: correlation to bone marrow micrometastases, heterogeneous response to systemic therapy and low proliferative activity. *Clinical cancer research : an official journal of the American Association for Cancer Research* **11**, 3678-3685, doi:10.1158/1078-0432.Ccr-04-2469 (2005).
21 Phan, T. G. & Croucher, P. I. The dormant cancer cell life cycle. *Nature reviews. Cancer* **20**, 398-411, doi:10.1038/s41568-020-0263-0 (2020).

22 Aguirre-Ghiso, J. A., Soledad Sosa M. Emerging Topics on Disseminated Cancer Cell Dormancy and the Paradigm of Metastasis. *Annual Review of Cancer Biology* (2018).
23 Risson E., N. A. R., Maguer-Satta V., Aguirre-Ghiso, J.A. The current paradigm and challenges ahead for the dormancy of disseminated tumor cells. *Nature Cancer* (2020).
24 Bartosh, T. J., Ullah, M., Zeitouni, S., Beaver, J. & Prockop, D. J. Cancer cells enter dormancy after cannibalizing mesenchymal stem/stromal cells (MSCs). *Proc Natl Acad Sci U S A* **113**, E6447-e6456, doi:10.1073/pnas.1612290113 (2016).
25 Lee, H. R., Leslie, F. & Azarin, S. M. A facile in vitro platform to study cancer cell dormancy under hypoxic microenvironments using CoCl(2). *J Biol Eng* **12**, 12, doi:10.1186/s13036-018-0106-7 (2018).
26 Korah, R. M., Sysounthone, V., Golowa, Y. & Wieder, R. Basic fibroblast growth factor confers a less malignant phenotype in MDA-MB-231 human breast cancer cells. *Cancer research* **60**, 733-740 (2000).
27 Tomoda, R. *et al.* Low-dose methotrexate inhibits lung metastasis and lengthens survival in rat osteosarcoma. *Clin Exp Metastasis* **22**, 559-564, doi:10.1007/s10585-005-5377-y (2005).
28 Zhou, N. *et al.* Stem cell characteristics of dormant cells and cisplatin-induced effects on the stemness of epithelial ovarian cancer cells. *Mol Med Rep* **10**, 2495-2504, doi:10.3892/mmr.2014.2483 (2014).
29 Muthusamy, P., Chary, K. V. & Nalini, G. K. Metronomic Chemotherapy: Seems Prowess to Battle against Cancer in Current Scenario. *J Clin Diagn Res* **10**, Fc09-fc13, doi:10.7860/jcdr/2016/23782.8802 (2016).
30 Reynolds, D. S., Bougher, K. M., Letendre, J. H., Fitzgerald, S. F., Gisladottir, U. O., Grinstaff, M. W., Zaman, M. H. Mechanical confinement via a PEG/Collagen interpenetrating network inhibits behavior characteristic of malignant cells in the triple negative breast cancer cell line MDA.MB.231. *Acta Biomater* **77**, 85-95, doi:10.1016/j.actbio.2018.07.032 (2018).
31 Fang, J. Y., Tan, S. J., Wu, Y. C., Yang, Z., Hoang, B. X., Han, B. From competency to dormancy: a 3D model to study cancer cells and drug responsiveness. *Journal of translational medicine* **14**, 38, doi:10.1186/s12967-016-0798-8 (2016).
32 Cheng, G., Tse, J., Jain, R. K. & Munn, L. L. Micro-environmental mechanical stress controls tumor spheroid size and morphology by suppressing proliferation and inducing apoptosis in cancer cells. *PLoS One* **4**, e4632, doi:10.1371/journal.pone.0004632 (2009).
33 Keeratichamroen, S., Lirdprapamongkol, K. & Svasti, J. Mechanism of ECM-induced dormancy and chemoresistance in A549 human lung carcinoma cells. *Oncology reports* **39**, 1765-1774, doi:10.3892/or.2018.6258 (2018).

34 Pradhan, S. & Slater, J. H. Datasets describing hydrogel properties and cellular metrics for modeling of tumor dormancy. *Data in brief* **25**, 104128, doi:10.1016/j.dib.2019.104128 (2019).
35 Pradhan, S. & Slater, J. H. Tunable hydrogels for controlling phenotypic cancer cell states to model breast cancer dormancy and reactivation. *Biomaterials* **215**, 119177, doi:10.1016/j.biomaterials.2019.04.022 (2019).
36 Pradhan, S. & Slater, J. H. Fabrication, characterization, and implementation of engineered hydrogels for controlling breast cancer cell phenotype and dormancy. *MethodsX* **6**, 2744-2766, doi:10.1016/j.mex.2019.11.011 (2019).
37 Joyce, J. A. & Pollard, J. W. Microenvironmental regulation of metastasis. *Nature reviews. Cancer* **9**, 239-252, doi:10.1038/nrc2618 (2009).
38 Kang, Y. *et al.* A multigenic program mediating breast cancer metastasis to bone. *Cancer cell* **3**, 537-549, doi:10.1016/s1535-6108(03)00132-6 (2003).
39 Minn, A. J. *et al.* Genes that mediate breast cancer metastasis to lung. *Nature* **436**, 518-524, doi:10.1038/nature03799 (2005).
40 Bos, P. D. *et al.* Genes that mediate breast cancer metastasis to the brain. *Nature* **459**, 1005-1009, doi:10.1038/nature08021 (2009).
41 Farino Reyes, C. J., Pradhan, S., Slater, J.H. The Influence of Ligand Density and Degradability on Hydrogel Induced Breast Cancer Dormancy and Reactivation. *Advanced Healthcare Materials* (2021).
42 Walimbe, T. & Panitch, A. Proteoglycans in Biomedicine: Resurgence of an Underexploited Class of ECM Molecules. *Front Pharmacol* **10**, 1661, doi:10.3389/fphar.2019.01661 (2019).
43 Montagner, M. & Sahai, E. In vitro Models of Breast Cancer Metastatic Dormancy. *Front Cell Dev Biol* **8**, 37, doi:10.3389/fcell.2020.00037 (2020).
44 Kloxin, A. M., Kasko, A. M., Salinas, C. N. & Anseth, K. S. Photodegradable hydrogels for dynamic tuning of physical and chemical properties. *Science (New York, N.Y.)* **324**, 59-63, doi:10.1126/science.1169494 (2009).
45 Farino, C. J., Pradhan, S., Slater, J.H. The Influence of Matrix Induced Dormancy on Metastatic Breast Cancer Chemoresistance. *ACS Applied Bio Materials* (2020).
46 Robinson, L. J. *et al.* Human MDR 1 protein overexpression delays the apoptotic cascade in Chinese hamster ovary fibroblasts. *Biochemistry* **36**, 11169-11178, doi:10.1021/bi9627830 (1997).
47 Leonard, G. D., Fojo, T. & Bates, S. E. The role of ABC transporters in clinical practice. *Oncologist* **8**, 411-424, doi:10.1634/theoncologist.8-5-411 (2003).
48 Cole, S. P. Multidrug resistance protein 1 (MRP1, ABCC1), a "multitasking" ATP-binding cassette (ABC) transporter. *J Biol Chem* **289**, 30880-30888, doi:10.1074/jbc.R114.609248 (2014).
49 Peterson, B. G., Tan, K. W., Osa-Andrews, B. & Iram, S. H. High-content screening of clinically tested anticancer drugs identifies novel inhibitors of

human MRP1 (ABCC1). *Pharmacol Res* **119**, 313-326, doi:10.1016/j.phrs.2017.02.024 (2017).
50 Toyoda, Y., Takada, T. & Suzuki, H. Inhibitors of Human ABCG2: From Technical Background to Recent Updates With Clinical Implications. *Front Pharmacol* **10**, 208, doi:10.3389/fphar.2019.00208 (2019).
51 Vlaming, M. L., Lagas, J. S. & Schinkel, A. H. Physiological and pharmacological roles of ABCG2 (BCRP): recent findings in Abcg2 knockout mice. *Adv Drug Deliv Rev* **61**, 14-25, doi:10.1016/j.addr.2008.08.007 (2009).
52 American Society of Clinical Oncology. Breast Cancer - Metastatic: Statistics. (2021).
53 Giancotti, F. G. Mechanisms governing metastatic dormancy and reactivation. *Cell* **155**, 750-764, doi:10.1016/j.cell.2013.10.029 (2013).
54 Ghajar, C. M. Metastasis prevention by targeting the dormant niche. *Nature reviews. Cancer* **15**, 238-247, doi:10.1038/nrc3910 (2015).
55 Turturro, M. V., Sokic, S., Larson, J. C. & Papavasiliou, G. Effective tuning of ligand incorporation and mechanical properties in visible light photopolymerized poly(ethylene glycol) diacrylate hydrogels dictates cell adhesion and proliferation. *Biomed Mater* **8**, 025001, doi:10.1088/1748-6041/8/2/025001 (2013).
56 Lee, C., Teymour, F., Camastral, H., Tirelli, N., Hubbell, J., Elbert, D., Papavasiliou, G. . Characterization of the Network Structure of PEG Diacrylate Hydrogels Formed in the Presence of N-Vinyl Pyrrolidone. *Macromolecular Reaction Engineering* **8**, 314-328 (2013).
57 Gill, B. J. *et al.* A synthetic matrix with independently tunable biochemistry and mechanical properties to study epithelial morphogenesis and EMT in a lung adenocarcinoma model. *Cancer research* **72**, 6013-6023, doi:10.1158/0008-5472.Can-12-0895 (2012).
58 Schweller, R. M. & West, J. L. Encoding Hydrogel Mechanics via Network Cross-Linking Structure. *ACS Biomater Sci Eng* **1**, 335-344, doi:10.1021/acsbiomaterials.5b00064 (2015).
59 Schweller, R. M., Wu, Z. J., Klitzman, B. & West, J. L. Stiffness of Protease Sensitive and Cell Adhesive PEG Hydrogels Promotes Neovascularization In Vivo. *Ann Biomed Eng* **45**, 1387-1398, doi:10.1007/s10439-017-1822-8 (2017).
60 Akhtar, M., Haider, A., Rashid, S. & Al-Nabet, A. Paget's "Seed and Soil" Theory of Cancer Metastasis: An Idea Whose Time has Come. *Advances in anatomic pathology* **26**, 69-74, doi:10.1097/pap.0000000000000219 (2019).
61 Langley, R. R. & Fidler, I. J. The seed and soil hypothesis revisited--the role of tumor-stroma interactions in metastasis to different organs. *International journal of cancer* **128**, 2527-2535, doi:10.1002/ijc.26031 (2011).
62 Fokas, E., Engenhart-Cabillic, R., Daniilidis, K., Rose, F. & An, H. X. Metastasis: the seed and soil theory gains identity. *Cancer metastasis reviews* **26**, 705-715, doi:10.1007/s10555-007-9088-5 (2007).

63 Nguyen, D. X., Bos, P. D. & Massague, J. Metastasis: from dissemination to organ-specific colonization. *Nature reviews. Cancer* **9**, 274-284, doi:10.1038/nrc2622 (2009).
64 Kim, R. S. *et al.* Dormancy signatures and metastasis in estrogen receptor positive and negative breast cancer. *PLoS One* **7**, e35569, doi:10.1371/journal.pone.0035569 (2012).
65 Zhang, X. H., Giuliano, M., Trivedi, M. V., Schiff, R. & Osborne, C. K. Metastasis dormancy in estrogen receptor-positive breast cancer. *Clinical cancer research : an official journal of the American Association for Cancer Research* **19**, 6389-6397, doi:10.1158/1078-0432.Ccr-13-0838 (2013).
66 Zhang, F. L. *et al.* Cancer-Associated MORC2-Mutant M276I Regulates an hnRNPM-Mediated CD44 Splicing Switch to Promote Invasion and Metastasis in Triple-Negative Breast Cancer. *Cancer research* **78**, 5780-5792, doi:10.1158/0008-5472.Can-17-1394 (2018).
67 Schwartz, A. D., Hall, C. L., Barney, L. E., Babbitt, C. C. & Peyton, S. R. Integrin α(6) and EGFR signaling converge at mechanosensitive calpain 2. *Biomaterials* **178**, 73-82, doi:10.1016/j.biomaterials.2018.05.056 (2018).
68 Liang, M. *et al.* IL-11 is essential in promoting osteolysis in breast cancer bone metastasis via RANKL-independent activation of osteoclastogenesis. *Cell Death Dis* **10**, 353, doi:10.1038/s41419-019-1594-1 (2019).
69 Ovadia, E. M. *et al.* Understanding ER+ Breast Cancer Dormancy Using Bioinspired Synthetic Matrices for Long-Term 3D Culture and Insights into Late Recurrence. *Adv Biosyst* **4**, e2000119, doi:10.1002/adbi.202000119 (2020).
70 Comşa, Ş., Cîmpean, A. M. & Raica, M. The Story of MCF-7 Breast Cancer Cell Line: 40 years of Experience in Research. *Anticancer research* **35**, 3147-3154 (2015).
71 Aguirre-Ghiso, J. A., Estrada, Y., Liu, D. & Ossowski, L. ERK(MAPK) activity as a determinant of tumor growth and dormancy; regulation by p38(SAPK). *Cancer research* **63**, 1684-1695 (2003).
72 Aguirre-Ghiso, J. A., Liu, D., Mignatti, A., Kovalski, K. & Ossowski, L. Urokinase receptor and fibronectin regulate the ERK(MAPK) to p38(MAPK) activity ratios that determine carcinoma cell proliferation or dormancy in vivo. *Mol Biol Cell* **12**, 863-879, doi:10.1091/mbc.12.4.863 (2001).
73 Park, S. Y. & Nam, J. S. The force awakens: metastatic dormant cancer cells. *Exp Mol Med* **52**, 569-581, doi:10.1038/s12276-020-0423-z (2020).
74 Adam, A. P. *et al.* Computational identification of a p38SAPK-regulated transcription factor network required for tumor cell quiescence. *Cancer research* **69**, 5664-5672, doi:10.1158/0008-5472.Can-08-3820 (2009).
75 McGrath, J., Panzica, L., Ransom, R., Withers, H. G. & Gelman, I. H. Identification of Genes Regulating Breast Cancer Dormancy in 3D Bone Endosteal Niche Cultures. *Molecular cancer research : MCR* **17**, 860-869, doi:10.1158/1541-7786.Mcr-18-0956 (2019).

76 Guereño, M. *et al.* Glypican-3 (GPC3) inhibits metastasis development promoting dormancy in breast cancer cells by p38 MAPK pathway activation. *Eur J Cell Biol* **99**, 151096, doi:10.1016/j.ejcb.2020.151096 (2020).
77 Cameron, M. D. *et al.* Temporal progression of metastasis in lung: cell survival, dormancy, and location dependence of metastatic inefficiency. *Cancer research* **60**, 2541-2546 (2000).
78 Chambers, A. F., Groom, A. C. & MacDonald, I. C. Dissemination and growth of cancer cells in metastatic sites. *Nature reviews. Cancer* **2**, 563-572, doi:10.1038/nrc865 (2002).
79 Chen, C. *et al.* TSC-mTOR maintains quiescence and function of hematopoietic stem cells by repressing mitochondrial biogenesis and reactive oxygen species. *J Exp Med* **205**, 2397-2408, doi:10.1084/jem.20081297 (2008).
80 Wang, Y. H. *et al.* Cell-state-specific metabolic dependency in hematopoiesis and leukemogenesis. *Cell* **158**, 1309-1323, doi:10.1016/j.cell.2014.07.048 (2014).
81 Faubert, B., Solmonson, A. & DeBerardinis, R. J. Metabolic reprogramming and cancer progression. *Science (New York, N.Y.)* **368**, doi:10.1126/science.aaw5473 (2020).
82 Aguirre-Ghiso, J. A. How dormant cancer persists and reawakens. *Science (New York, N.Y.)* **361**, 1314-1315, doi:10.1126/science.aav0191 (2018).
83 Rao, S. S., Kondapaneni, R. V. & Narkhede, A. A. Bioengineered models to study tumor dormancy. *J Biol Eng* **13**, 3, doi:10.1186/s13036-018-0137-0 (2019).
84 Barkan, D., Green, J.E., Chamabers, A. Extracellular Matrix: A Gatekeeper in the Transition from Dormancy to Metastatic Growth. *European Journal of Cancer* (2010).
85 Narkhede, A. A., Crenshaw, J. H., Crossman, D. K., Shevde, L. A. & Rao, S. S. An in vitro hyaluronic acid hydrogel based platform to model dormancy in brain metastatic breast cancer cells. *Acta Biomater* **107**, 65-77, doi:10.1016/j.actbio.2020.02.039 (2020).
86 Kondapaneni, R. V. & Rao, S. S. Matrix stiffness and cluster size collectively regulate dormancy versus proliferation in brain metastatic breast cancer cell clusters. *Biomater Sci*, doi:10.1039/d0bm00969e (2020).
87 He, H. *et al.* Engineering Helical Modular Polypeptide-Based Hydrogels as Synthetic Extracellular Matrices for Cell Culture. *Biomacromolecules* **21**, 566-580, doi:10.1021/acs.biomac.9b01297 (2020).
88 Galarza, S., Crosby, A. J., Pak, C. & Peyton, S. R. Control of Astrocyte Quiescence and Activation in a Synthetic Brain Hydrogel. *Adv Healthc Mater* **9**, e1901419, doi:10.1002/adhm.201901419 (2020).
89 Jansen, L., Thomas P. McCarthy, Michael J. Lee, and Shelly R. Peyton. A synthetic, three-dimensional bone marrow hydrogel. *bioRxiv* (2018).

90 Tan, H., DeFail, A. J., Rubin, J. P., Chu, C. R. & Marra, K. G. Novel multiarm PEG-based hydrogels for tissue engineering. *J Biomed Mater Res A* **92**, 979-987, doi:10.1002/jbm.a.32438 (2010).
91 Lam, T., Aguirre-Ghiso, J. A., Geller, M. A., Aksan, A. & Azarin, S. M. Immobilization rapidly selects for chemoresistant ovarian cancer cells with enhanced ability to enter dormancy. *Biotechnol Bioeng*, doi:10.1002/bit.27479 (2020).
92 *Central Nervous System Metastasis, the Biological Basis and Clinical Considerations*. (Springer, 2012).
93 Tsuchida, A. *et al.* Synthesis of disialyl Lewis a (Le(a)) structure in colon cancer cell lines by a sialyltransferase, ST6GalNAc VI, responsible for the synthesis of alpha-series gangliosides. *J Biol Chem* **278**, 22787-22794, doi:10.1074/jbc.M211034200 (2003).
94 Yanagishita, M. Function of proteoglycans in the extracellular matrix. *Acta Pathol Jpn* **43**, 283-293, doi:10.1111/j.1440-1827.1993.tb02569.x (1993).
95 Weinbaum, S., Tarbell, J. M. & Damiano, E. R. The structure and function of the endothelial glycocalyx layer. *Annu Rev Biomed Eng* **9**, 121-167, doi:10.1146/annurev.bioeng.9.060906.151959 (2007).
96 Gubbiotti, M. A., Vallet, S. D., Ricard-Blum, S. & Iozzo, R. V. Decorin interacting network: A comprehensive analysis of decorin-binding partners and their versatile functions. *Matrix Biol* **55**, 7-21, doi:10.1016/j.matbio.2016.09.009 (2016).
97 Christensen, G., Herum, K. M. & Lunde, I. G. Sweet, yet underappreciated: Proteoglycans and extracellular matrix remodeling in heart disease. *Matrix Biol* **75-76**, 286-299, doi:10.1016/j.matbio.2018.01.001 (2019).
98 Barney, L. E. *et al.* Tumor cell-organized fibronectin maintenance of a dormant breast cancer population. *Sci Adv* **6**, eaaz4157, doi:10.1126/sciadv.aaz4157 (2020).
99 Handorf, A. M., Zhou, Y., Halanski, M. A. & Li, W. J. Tissue stiffness dictates development, homeostasis, and disease progression. *Organogenesis* **11**, 1-15, doi:10.1080/15476278.2015.1019687 (2015).
100 Hinz, B. Mechanical aspects of lung fibrosis: a spotlight on the myofibroblast. *Proc Am Thorac Soc* **9**, 137-147, doi:10.1513/pats.201202-017AW (2012).
101 Lovitt, C. J., Shelper, T. B. & Avery, V. M. Doxorubicin resistance in breast cancer cells is mediated by extracellular matrix proteins. *BMC cancer* **18**, 41, doi:10.1186/s12885-017-3953-6 (2018).
102 Wu, F. H., Mu, L., Li, X. L., Hu, Y. B., Liu, H., Han, L. T., Gong, J. P. Characterization and functional analysis of a slow-cycling subpopulation in colorectal cancer enriched by cell cycle inducer combined chemotherapy. *Oncotarget* **8**, 78466-78479, doi:10.18632/oncotarget.19638 (2017).
103 Yamada, T., Takaoka, A. S., Naishiro, Y., Hayashi, R., Maruyama, K., Maesawa, C., Ochiai, A., Hirohashi, S. Transactivation of the multidrug

resistance 1 gene by T-cell factor 4/beta-catenin complex in early colorectal carcinogenesis. *Cancer research* **60**, 4761-4766 (2000).
104 Avvisato, C. L., Yang, X., Shah, S., Hoxter, B., Li, W., Gaynor, R., Pestell, R., Tozeren, A., Byers, S. W. Mechanical force modulates global gene expression and beta-catenin signaling in colon cancer cells. *J Cell Sci* **120**, 2672-2682, doi:10.1242/jcs.03476 (2007).
105 Motlagh, N. S., Parvin, P., Ghasemi, F. & Atyabi, F. Fluorescence properties of several chemotherapy drugs: doxorubicin, paclitaxel and bleomycin. *Biomed Opt Express* **7**, 2400-2406, doi:10.1364/boe.7.002400 (2016).
106 Shah, S., Chandra, A., Kaur, A., Sabnis, N., Lacko, A., Gryczynski, Z., Fudala, R., Gryczynski, I. Fluorescence properties of doxorubicin in PBS buffer and PVA films. *J Photochem Photobiol B* **170**, 65-69, doi:10.1016/j.jphotobiol.2017.03.024 (2017).
107 Lankelma, J., Dekker, H., Luque, F. R., Luykx, S., Hoekman, K., van der Valk, P., van Diest, P. J., Pinedo, H. M. Doxorubicin gradients in human breast cancer. *Clinical cancer research : an official journal of the American Association for Cancer Research* **5**, 1703-1707 (1999).
108 Brooks, E. A., Galarza, S., Gencoglu, M. F., Cornelison, R. C., Munson, J. M., Peyton, S. R. Applicability of drug response metrics for cancer studies using biomaterials. *Philosophical transactions of the Royal Society of London. Series B, Biological sciences* **374**, 20180226, doi:10.1098/rstb.2018.0226 (2019).
109 Richter, V., Weber, P., Wagner, M, Schneckenburger, H. 3D visualization of cellular location and cytotoxic reactions of doxorubicin, a chemotherapeutic agent. *Medical Research Archives* **6** (2018).
110 Kauffman, M. K., Kauffman, M. E., Zhu, H., Jia, Z. & Li, Y. R. Fluorescence-Based Assays for Measuring Doxorubicin in Biological Systems. *React Oxyg Species (Apex)* **2**, 432-439, doi:10.20455/ros.2016.873 (2016).
111 Rusetskaya, N. V., Khariton, N., Yurchenko, O. V. & Chekhun, V. F. Distribution and accumulation of liposomal form of doxorubicin in breast cancer cells of MCF-7 line. *Exp Oncol* **33**, 78-82 (2011).
112 Genomics of Drug Sensitivity in Cancer - Compound: Doxorubicin. *Wellcome Sanger Institue and Massachusetts General Hospital Cancer Center* (2020).
113 Genomics of Drug Sensitivity in Cancer - Compound: Paclitaxel. *Wellcome Sanger Institue and Massachusetts General Hospital Cancer Center* (2020).
114 Genomics of Drug Sensitivity in Cancer - Compound: 5-Fluorouracil. *Wellcome Sanger Institue and Massachusetts General Hospital Cancer Center* (2020).
115 Imamura, Y., Mukohara, T., Shimono, Y., Funakoshi, Y., Chayahara, N., Toyoda, M., Kiyota, N., Takao, S., Kono, S., Nakatsura, T., Minami, H. Comparison of 2D- and 3D-culture models as drug-testing platforms in breast cancer. *Oncology reports* **33**, 1837-1843, doi:10.3892/or.2015.3767 (2015).
116 Edmondson, R., Broglie, J. J., Adcock, A. F. & Yang, L. Three-dimensional cell culture systems and their applications in drug discovery and cell-based

biosensors. *Assay Drug Dev Technol* **12**, 207-218, doi:10.1089/adt.2014.573 (2014).
117 Bilalis, P., Tziveleka, L., Varlas, S., Hermis, I. pH-Sensitive nanogates based on poly(l-histidine) for controlled drug release from mesoporous silica nanoparticles† *Polymer Chemistry* (2016).
118 Krieg, E., Albeck, S., Weissman, H., Shimoni, E. & Rybtchinski, B. Separation, immobilization, and biocatalytic utilization of proteins by a supramolecular membrane. *PLoS One* **8**, e63188, doi:10.1371/journal.pone.0063188 (2013).
119 Yang, F., Teves, S. S., Kemp, C. J. & Henikoff, S. Doxorubicin, DNA torsion, and chromatin dynamics. *Biochim Biophys Acta* **1845**, 84-89, doi:10.1016/j.bbcan.2013.12.002 (2014).
120 Huang, C. Y., Ju, D. T., Chang, C. F., Muralidhar Reddy, P. & Velmurugan, B. K. A review on the effects of current chemotherapy drugs and natural agents in treating non-small cell lung cancer. *BioMedicine* **7**, 23, doi:10.1051/bmdcn/2017070423 (2017).
121 Mitchison, T. J. The proliferation rate paradox in antimitotic chemotherapy. *Mol Biol Cell* **23**, 1-6, doi:10.1091/mbc.E10-04-0335 (2012).
122 Broustas, C. G. & Lieberman, H. B. DNA damage response genes and the development of cancer metastasis. *Radiat Res* **181**, 111-130, doi:10.1667/rr13515.1 (2014).
123 Berenbaum, M. C. In vivo determination of the fractional kill of human tumor cells by chemotherapeutic agents. *Cancer Chemother Rep* **56**, 563-571 (1972).
124 Amadori, D., Volpi, A., Maltoni, R., Nanni, O., Amaducci, L., Amadori, A., Giunchi, D. C., Vio, A., Saragoni, A., Silvestrini, R. Cell proliferation as a predictor of response to chemotherapy in metastatic breast cancer: a prospective study. *Breast Cancer Res Treat* **43**, 7-14, doi:10.1023/a:1005780107879 (1997).
125 Shen, F., Chu, S., Bence, A. K., Bailey, B., Xue, X., Erickson, P. A., Montrose, M. H., Beck, W. T., Erickson, L. C. Quantitation of doxorubicin uptake, efflux, and modulation of multidrug resistance (MDR) in MDR human cancer cells. *J Pharmacol Exp Ther* **324**, 95-102, doi:10.1124/jpet.107.127704 (2008).
126 Schuurhuis, G. J., van Heijningen, T. H., Cervantes, A., Pinedo, H. M., de Lange, J. H., Keizer, H. G., Broxterman, H. J., Baak, J. P., Lankelma, J. Changes in subcellular doxorubicin distribution and cellular accumulation alone can largely account for doxorubicin resistance in SW-1573 lung cancer and MCF-7 breast cancer multidrug resistant tumour cells. *Br J Cancer* **68**, 898-908, doi:10.1038/bjc.1993.452 (1993).
127 Bao, L., Hazari, S., Mehra, S., Kaushal, D., Moroz, K., Dash, S. Increased expression of P-glycoprotein and doxorubicin chemoresistance of metastatic breast cancer is regulated by miR-298. *Am J Pathol* **180**, 2490-2503, doi:10.1016/j.ajpath.2012.02.024 (2012).

128 Lawson, M. A., McDonald, M. M., Kovacic, N., Hua Khoo, W., Terry, R. L., Down, J., Kaplan, W., Paton-Hough, J., Fellows, C., Pettitt, J. A., Neil Dear, T., Van Valckenborgh, E., Baldock, P. A., Rogers, M. J., Eaton, C. L., Vanderkerken, K., Pettit, A. R., Quinn, J. M., Zannettino, A. C., Phan, T. G., Croucher, P. I. Osteoclasts control reactivation of dormant myeloma cells by remodelling the endosteal niche. *Nat Commun* **6**, 8983, doi:10.1038/ncomms9983 (2015).

129 Lee, S. H., Park, S. A., Zou, Y., Seo, S. U., Jun, C. D., Lee, W. J., Hyun, Y. M., Cho, N. H. Real-Time Monitoring of Cancer Cells in Live Mouse Bone Marrow. *Front Immunol* **9**, 1681, doi:10.3389/fimmu.2018.01681 (2018).

130 Zheng, H. C. The molecular mechanisms of chemoresistance in cancers. *Oncotarget* **8**, 59950-59964, doi:10.18632/oncotarget.19048 (2017).

131 Muriithi, W. *et al.* ABC transporters and the hallmarks of cancer: roles in cancer aggressiveness beyond multidrug resistance. *Cancer Biol Med* **17**, 253-269, doi:10.20892/j.issn.2095-3941.2019.0284 (2020).

132 Zakeri-Milani, P. & Valizadeh, H. Intestinal transporters: enhanced absorption through P-glycoprotein-related drug interactions. *Expert Opin Drug Metab Toxicol* **10**, 859-871, doi:10.1517/17425255.2014.905543 (2014).

133 Cole, S. P. Targeting multidrug resistance protein 1 (MRP1, ABCC1): past, present, and future. *Annu Rev Pharmacol Toxicol* **54**, 95-117, doi:10.1146/annurev-pharmtox-011613-135959 (2014).

134 Allen, J. D. *et al.* Potent and specific inhibition of the breast cancer resistance protein multidrug transporter in vitro and in mouse intestine by a novel analogue of fumitremorgin C. *Mol Cancer Ther* **1**, 417-425 (2002).

135 Gillet, J. P. & Gottesman, M. M. Mechanisms of multidrug resistance in cancer. *Methods Mol Biol* **596**, 47-76, doi:10.1007/978-1-60761-416-6_4 (2010).

136 Housman, G. *et al.* Drug resistance in cancer: an overview. *Cancers (Basel)* **6**, 1769-1792, doi:10.3390/cancers6031769 (2014).

137 Wong, H. L. *et al.* A mechanistic study of enhanced doxorubicin uptake and retention in multidrug resistant breast cancer cells using a polymer-lipid hybrid nanoparticle system. *J Pharmacol Exp Ther* **317**, 1372-1381, doi:10.1124/jpet.106.101154 (2006).

138 Tamaki, A., Ierano, C., Szakacs, G., Robey, R. W. & Bates, S. E. The controversial role of ABC transporters in clinical oncology. *Essays Biochem* **50**, 209-232, doi:10.1042/bse0500209 (2011).

139 Baldini, N. *et al.* Nuclear immunolocalization of P-glycoprotein in multidrug-resistant cell lines showing similar mechanisms of doxorubicin distribution. *Eur J Cell Biol* **68**, 226-239 (1995).

140 Blokzijl, H. *et al.* Up-regulation and cytoprotective role of epithelial multidrug resistance-associated protein 1 in inflammatory bowel disease. *J Biol Chem* **283**, 35630-35637, doi:10.1074/jbc.M804374200 (2008).

141 Fletcher, J. I., Haber, M., Henderson, M. J. & Norris, M. D. ABC transporters in cancer: more than just drug efflux pumps. *Nature reviews. Cancer* **10**, 147-156, doi:10.1038/nrc2789 (2010).
142 Haber, M. *et al.* Association of high-level MRP1 expression with poor clinical outcome in a large prospective study of primary neuroblastoma. *Journal of clinical oncology : official journal of the American Society of Clinical Oncology* **24**, 1546-1553, doi:10.1200/jco.2005.01.6196 (2006).
143 Allikmets, R., Schriml, L. M., Hutchinson, A., Romano-Spica, V. & Dean, M. A human placenta-specific ATP-binding cassette gene (ABCP) on chromosome 4q22 that is involved in multidrug resistance. *Cancer research* **58**, 5337-5339 (1998).
144 Doyle, L. A. *et al.* A multidrug resistance transporter from human MCF-7 breast cancer cells. *Proc Natl Acad Sci U S A* **95**, 15665-15670, doi:10.1073/pnas.95.26.15665 (1998).
145 Miyake, K. *et al.* Molecular cloning of cDNAs which are highly overexpressed in mitoxantrone-resistant cells: demonstration of homology to ABC transport genes. *Cancer research* **59**, 8-13 (1999).
146 Brewer, F. K., Follit, C. A., Vogel, P. D. & Wise, J. G. In silico screening for inhibitors of p-glycoprotein that target the nucleotide binding domains. *Mol Pharmacol* **86**, 716-726, doi:10.1124/mol.114.095414 (2014).
147 Binkhathlan, Z. & Lavasanifar, A. P-glycoprotein inhibition as a therapeutic approach for overcoming multidrug resistance in cancer: current status and future perspectives. *Curr Cancer Drug Targets* **13**, 326-346, doi:10.2174/15680096113139990076 (2013).
148 Palmeira, A., Sousa, E., Vasconcelos, M. H. & Pinto, M. M. Three decades of P-gp inhibitors: skimming through several generations and scaffolds. *Curr Med Chem* **19**, 1946-2025, doi:10.2174/092986712800167392 (2012).
149 Ricci, J. W., Lovato, D., Larson, R.S. ABCG2 Inhibitors: Will They Find Clinical Relevance? *Journal of Developing Drugs* (2015).
150 Tivnan, A. *et al.* Inhibition of multidrug resistance protein 1 (MRP1) improves chemotherapy drug response in primary and recurrent glioblastoma multiforme. *Front Neurosci* **9**, 218, doi:10.3389/fnins.2015.00218 (2015).
151 Burkhart, C. A. *et al.* Small-molecule multidrug resistance-associated protein 1 inhibitor reversan increases the therapeutic index of chemotherapy in mouse models of neuroblastoma. *Cancer research* **69**, 6573-6580, doi:10.1158/0008-5472.Can-09-1075 (2009).
152 van Loevezijn, A., Allen, J. D., Schinkel, A. H. & Koomen, G. J. Inhibition of BCRP-mediated drug efflux by fumitremorgin-type indolyl diketopiperazines. *Bioorg Med Chem Lett* **11**, 29-32, doi:10.1016/s0960-894x(00)00588-6 (2001).
153 Łania-Pietrzak, B. *et al.* Modulation of MRP1 protein transport by plant, and synthetically modified flavonoids. *Life Sci* **77**, 1879-1891, doi:10.1016/j.lfs.2005.04.005 (2005).

154 Morfouace, M. *et al.* ABCG2 Transporter Expression Impacts Group 3 Medulloblastoma Response to Chemotherapy. *Cancer research* **75**, 3879-3889, doi:10.1158/0008-5472.Can-15-0030 (2015).
155 Schnúr, A., Premchandar, A., Bagdany, M. & Lukacs, G. L. Phosphorylation-dependent modulation of CFTR macromolecular signalling complex activity by cigarette smoke condensate in airway epithelia. *Sci Rep* **9**, 12706, doi:10.1038/s41598-019-48971-y (2019).
156 Kannan, P. *et al.* The "specific" P-glycoprotein inhibitor Tariquidar is also a substrate and an inhibitor for breast cancer resistance protein (BCRP/ABCG2). *ACS Chem Neurosci* **2**, 82-89, doi:10.1021/cn100078a (2011).
157 Kittaneh, M., Montero, A., and Glück, S. Molecular Profiling for Breast Cancer: A Comprehensive Review. *Biomarkers Cancer* (2013).

Appendix A

COPYRIGHT PERMISSIONS

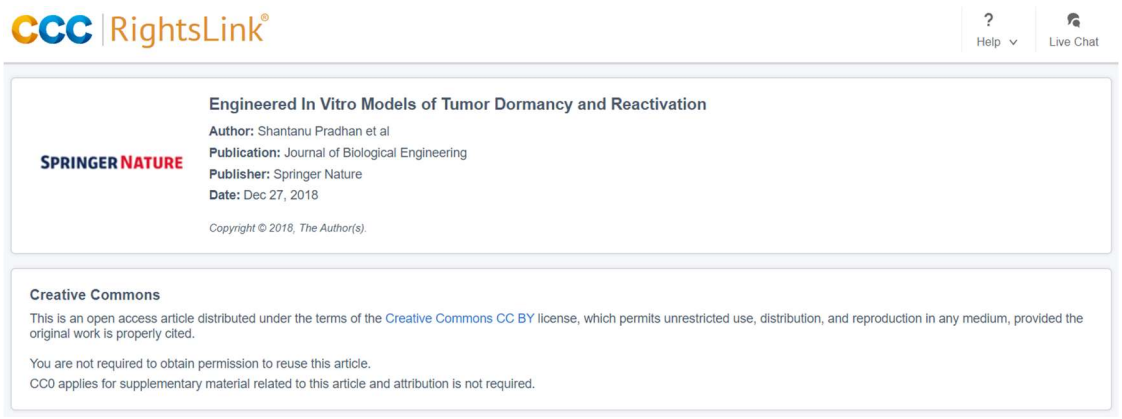

The Influence of Matrix-Induced Dormancy on Metastatic Breast Cancer Chemoresistance

Author: Cindy J. Farino, Shantanu Pradhan, John H. Slater
Publication: ACS Applied Bio Materials
Publisher: American Chemical Society
Date: Sep 1, 2020

PERMISSION/LICENSE IS GRANTED FOR YOUR ORDER AT NO CHARGE

This type of permission/license, instead of the standard Terms and Conditions, is sent to you because no fee is being charged for your order. Please note the following:

- Permission is granted for your request in both print and electronic formats, and translations.
- If figures and/or tables were requested, they may be adapted or used in part.
- Please print this page for your records and send a copy of it to your publisher/graduate school.
- Appropriate credit for the requested material should be given as follows: "Reprinted (adapted) with permission from {COMPLETE REFERENCE CITATION). Copyright {YEAR} American Chemical Society." Insert appropriate information in place of the capitalized words.
- One-time permission is granted only for the use specified in your RightsLink request. No additional uses are granted (such as derivative works or other editions). For any uses, please submit a new request.

If credit is given to another source for the material you requested from RightsLink, permission must be obtained from that source.

BACK CLOSE WINDOW

CCC Marketplace™

Order Date	16-Nov-2021	Type of Use	Republish in a thesis/dissertation
Order License ID	1162044-1		
ISSN	2192-2640	Publisher	Wiley-VCH
		Portion	Chapter/article

LICENSED CONTENT

Publication Title	Advanced Healthcare Materials	Rightsholder	John Wiley & Sons - Books
		Publication Type	Journal
Article Title	The Influence of Ligand Density and Degradability on Hydrogel Induced Breast Cancer Dormancy and Reactivation	Start Page	2002227
		Issue	11
		Volume	10
Date	01/01/2012		
Language	English		
Country	Germany		

REQUEST DETAILS

Portion Type	Chapter/article	Rights Requested	Main product and any product related to main product
Page range(s)	1-20		
Total number of pages	20	Distribution	Worldwide
Format (select all that apply)	Print, Electronic	Translation	Original language of publication
Who will republish the content?	Academic institution	Copies for the disabled?	No
		Minor editing privileges?	Yes
Duration of Use	Life of current and all future editions	Incidental promotional use?	No
Lifetime Unit Quantity	Up to 499	Currency	USD

NEW WORK DETAILS

Title	TECHNIQUES FOR ENHANCED BIOMIMICRY OF IN VITRO VASCULAR MODELS	Institution name	University of Delaware
		Expected presentation date	2022-01-01
Instructor name	Cindy Farino		

ADDITIONAL DETAILS

The requesting person / organization to appear on the license	Cindy Farino Reyes / University of Delaware

REUSE CONTENT DETAILS

Title, description or numeric reference of the portion(s)	Text and Figures	Title of the article/chapter the portion is from	The Influence of Ligand Density and Degradability on Hydrogel Induced Breast Cancer Dormancy and Reactivation
Editor of portion(s)	Farino Reyes, Cindy J.; Pradhan, Shantanu; Slater, John H.	Author of portion(s)	Farino Reyes, Cindy J.; Pradhan, Shantanu; Slater, John H.
Volume of serial or monograph	10		
Page or page range of portion	1-20	Publication date of portion	2021-06-01

RIGHTSHOLDER TERMS AND CONDITIONS

No right, license or interest to any trademark, trade name, service mark or other branding ("Marks") of WILEY or its licensors is granted hereunder, and you agree that you shall not assert any such right, license or interest with respect thereto. You may not alter, remove or suppress in any manner any copyright, trademark or other notices displayed by the Wiley material. This Agreement will be void if the Type of Use, Format, Circulation, or Requestor Type was misrepresented during the licensing process. In no instance may the total amount of Wiley Materials used in any Main Product, Compilation or Collective work comprise more than 5% (if figures/tables) or 15% (if full articles/chapters) of the (entirety of the) Main Product, Compilation or Collective Work. Some titles may be available under an Open Access license. It is the Licensors' responsibility to identify the type of Open Access license on which the requested material was published, and comply fully with the terms of that license for the type of use specified Further details can be found on Wiley Online Library http://olabout.wiley.com/WileyCDA/Section/id-410895.html.

CCC Terms and Conditions

1. Description of Service; Defined Terms. This Republication License enables the User to obtain licenses for republication of one or more copyrighted works as described in detail on the relevant Order Confirmation (the "Work(s)"). Copyright Clearance Center, Inc. ("CCC") grants licenses through the Service on behalf of the rightsholder identified on the Order Confirmation (the "Rightsholder"). "Republication", as used herein, generally means the inclusion of a Work, in whole or in part, in a new work or works, also as described on the Order Confirmation. "User", as used herein, means the person or entity making such republication.

2. The terms set forth in the relevant Order Confirmation, and any terms set by the Rightsholder with respect to a particular Work, govern the terms of use of Works in connection with the Service. By using the Service, the person transacting for a republication license on behalf of the User represents and warrants that he/she/it (a) has been duly authorized by the User to accept, and hereby does accept, all such terms and conditions on behalf of User, and (b) shall inform User of all such terms and conditions. In the event such person is a "freelancer" or other third party independent of User and CCC, such party shall be deemed jointly a "User" for purposes of these terms and conditions. In any event, User shall be deemed to have accepted and agreed to all such terms and conditions if User republishes the Work in any fashion.

3. Scope of License; Limitations and Obligations.

   3.1. All Works and all rights therein, including copyright rights, remain the sole and exclusive property of the Rightsholder. The license created by the exchange of an Order Confirmation (and/or any invoice) and payment by User of the full amount set forth on that document includes only those rights expressly set forth in the Order Confirmation and in these terms and conditions, and conveys no other rights in the Work(s) to User. All rights not expressly granted are hereby reserved.

3.2. General Payment Terms: You may pay by credit card or through an account with us payable at the end of the month. If you and we agree that you may establish a standing account with CCC, then the following terms apply: Remit Payment to: Copyright Clearance Center, 29118 Network Place, Chicago, IL 60673-1291. Payments Due: Invoices are payable upon their delivery to you (or upon our notice to you that they are available to you for downloading). After 30 days, outstanding amounts will be subject to a service charge of 1-1/2% per month or, if less, the maximum rate allowed by applicable law. Unless otherwise specifically set forth in the Order Confirmation or in a separate written agreement signed by CCC, invoices are due and payable on "net 30" terms. While User may exercise the rights licensed immediately upon issuance of the Order Confirmation, the license is automatically revoked and is null and void, as if it had never been issued, if complete payment for the license is not received on a timely basis either from User directly or through a payment agent, such as a credit card company.

3.3. Unless otherwise provided in the Order Confirmation, any grant of rights to User (i) is "one-time" (including the editions and product family specified in the license), (ii) is non-exclusive and non-transferable and (iii) is subject to any and all limitations and restrictions (such as, but not limited to, limitations on duration of use or circulation) included in the Order Confirmation or invoice and/or in these terms and conditions. Upon completion of the licensed use, User shall either secure a new permission for further use of the Work(s) or immediately cease any new use of the Work(s) and shall render inaccessible (such as by deleting or by removing or severing links or other locators) any further copies of the Work (except for copies printed on paper in accordance with this license and still in User's stock at the end of such period).

3.4. In the event that the material for which a republication license is sought includes third party materials (such as photographs, illustrations, graphs, inserts and similar materials) which are identified in such material as having been used by permission, User is responsible for identifying, and seeking separate licenses (under this Service or otherwise) for, any of such third party materials; without a separate license, such third party materials may not be used.

3.5. Use of proper copyright notice for a Work is required as a condition of any license granted under the Service. Unless otherwise provided in the Order Confirmation, a proper copyright notice will read substantially as follows: "Republished with permission of [Rightsholder's name], from [Work's title, author, volume, edition number and year of copyright]; permission conveyed through Copyright Clearance Center, Inc. " Such notice must be provided in a reasonably legible font size and must be placed either immediately adjacent to the Work as used (for example, as part of a by-line or footnote but not as a separate electronic link) or in the place where substantially all other credits or notices for the new work containing the republished Work are located. Failure to include the required notice results in loss to the Rightsholder and CCC, and the User shall be liable to pay liquidated damages for each such failure equal to twice the use fee specified in the Order Confirmation, in addition to the use fee itself and any other fees and charges specified.

3.6. User may only make alterations to the Work if and as expressly set forth in the Order Confirmation. No Work may be used in any way that is defamatory, violates the rights of third parties (including such third parties' rights of copyright, privacy, publicity, or other tangible or intangible property), or is otherwise illegal, sexually explicit or obscene. In addition, User may not conjoin a Work with any other material that may result in damage to the reputation of the Rightsholder. User agrees to inform CCC if it becomes aware of any infringement of any rights in a Work and to cooperate with any reasonable request of CCC or the Rightsholder in connection therewith.

4. Indemnity. User hereby indemnifies and agrees to defend the Rightsholder and CCC, and their respective employees and directors, against all claims, liability, damages, costs and expenses, including legal fees and expenses, arising out of any use of a Work beyond the scope of the rights granted herein, or any use of a Work which has been altered in any unauthorized way by User, including claims of defamation or infringement of rights of copyright, publicity, privacy or other tangible or intangible property.

5. Limitation of Liability. UNDER NO CIRCUMSTANCES WILL CCC OR THE RIGHTSHOLDER BE LIABLE FOR ANY DIRECT, INDIRECT, CONSEQUENTIAL OR INCIDENTAL DAMAGES (INCLUDING WITHOUT LIMITATION DAMAGES FOR LOSS OF BUSINESS PROFITS OR INFORMATION, OR FOR BUSINESS INTERRUPTION) ARISING OUT OF THE USE OR INABILITY

TO USE A WORK, EVEN IF ONE OF THEM HAS BEEN ADVISED OF THE POSSIBILITY OF SUCH DAMAGES. In any event, the total liability of the Rightsholder and CCC (including their respective employees and directors) shall not exceed the total amount actually paid by User for this license. User assumes full liability for the actions and omissions of its principals, employees, agents, affiliates, successors and assigns.

6. Limited Warranties. THE WORK(S) AND RIGHT(S) ARE PROVIDED "AS IS". CCC HAS THE RIGHT TO GRANT TO USER THE RIGHTS GRANTED IN THE ORDER CONFIRMATION DOCUMENT. CCC AND THE RIGHTSHOLDER DISCLAIM ALL OTHER WARRANTIES RELATING TO THE WORK(S) AND RIGHT(S), EITHER EXPRESS OR IMPLIED, INCLUDING WITHOUT LIMITATION IMPLIED WARRANTIES OF MERCHANTABILITY OR FITNESS FOR A PARTICULAR PURPOSE. ADDITIONAL RIGHTS MAY BE REQUIRED TO USE ILLUSTRATIONS, GRAPHS, PHOTOGRAPHS, ABSTRACTS, INSERTS OR OTHER PORTIONS OF THE WORK (AS OPPOSED TO THE ENTIRE WORK) IN A MANNER CONTEMPLATED BY USER; USER UNDERSTANDS AND AGREES THAT NEITHER CCC NOR THE RIGHTSHOLDER MAY HAVE SUCH ADDITIONAL RIGHTS TO GRANT.

7. Effect of Breach. Any failure by User to pay any amount when due, or any use by User of a Work beyond the scope of the license set forth in the Order Confirmation and/or these terms and conditions, shall be a material breach of the license created by the Order Confirmation and these terms and conditions. Any breach not cured within 30 days of written notice thereof shall result in immediate termination of such license without further notice. Any unauthorized (but licensable) use of a Work that is terminated immediately upon notice thereof may be liquidated by payment of the Rightsholder's ordinary license price therefor; any unauthorized (and unlicensable) use that is not terminated immediately for any reason (including, for example, because materials containing the Work cannot reasonably be recalled) will be subject to all remedies available at law or in equity, but in no event to a payment of less than three times the Rightsholder's ordinary license price for the most closely analogous licensable use plus Rightsholder's and/or CCC's costs and expenses incurred in collecting such payment.

8. Miscellaneous.

   8.1. User acknowledges that CCC may, from time to time, make changes or additions to the Service or to these terms and conditions, and CCC reserves the right to send notice to the User by electronic mail or otherwise for the purposes of notifying User of such changes or additions; provided that any such changes or additions shall not apply to permissions already secured and paid for.

   8.2. Use of User-related information collected through the Service is governed by CCC's privacy policy, available online here:https://marketplace.copyright.com/rs-ui-web/mp/privacy-policy

   8.3. The licensing transaction described in the Order Confirmation is personal to User. Therefore, User may not assign or transfer to any other person (whether a natural person or an organization of any kind) the license created by the Order Confirmation and these terms and conditions or any rights granted hereunder; provided, however, that User may assign such license in its entirety on written notice to CCC in the event of a transfer of all or substantially all of User's rights in the new material which includes the Work(s) licensed under this Service.

   8.4. No amendment or waiver of any terms is binding unless set forth in writing and signed by the parties. The Rightsholder and CCC hereby object to any terms contained in any writing prepared by the User or its principals, employees, agents or affiliates and purporting to govern or otherwise relate to the licensing transaction described in the Order Confirmation, which terms are in any way inconsistent with any terms set forth in the Order Confirmation and/or in these terms and conditions or CCC's standard operating procedures, whether such writing is prepared prior to, simultaneously with or subsequent to the Order Confirmation, and whether such writing appears on a copy of the Order Confirmation or in a separate instrument.

   8.5. The licensing transaction described in the Order Confirmation document shall be governed by and construed under the law of the State of New York, USA, without regard to the principles thereof of conflicts of law. Any case, controversy, suit, action, or proceeding arising out of, in connection with, or related to such licensing transaction shall be brought, at CCC's sole discretion, in any federal or state court located in the County of New York, State of New York, USA, or in any federal or state court whose geographical

Appendix B

ACRONYMS

5-FU	5-Fluorouracil
ANOVA	One-Way Analysis of Variance
BCRP	Breast Cancer Resistance Protein
BoM-1833	Bone-tropic MDA-MB-231Subline
BrM2a-831	Brain-tropic MDA-MB-231Subline
BSA	Bovine Serum Albumin
CTFG	Connective Tissue Growth Factor
CXCR4	Chemokine Receptor Type 4
DTC	Disseminated Circulating Tumor Cell
DIPEA	N,N-diisoproylethylamine
DMEM	Dulbecco's Modified Eagle's Medium
DMSO	Dimethyl Sulfoxide
DOX	Doxorubicin
EC_{50}	Half maximal effective concentration
ECM	Extracellular Matrix
EdU^+ Ratio	Number of EdU^+ Cells at Day 15: EdU^+ Cells at Day 0
EdU^+:Annexin V^+ Cell Ratio	Number of EdU^+ Cells at Day 15: Annexin V^+ Cells at Day 0
EMT	Epithelial-Mesenchymal Transition
ERK	Extracellular Signal-Regulated Kinase

FBS	Fetal Bovine Serum
FGF5	Fibroblast Growth Factor 5
FITC	Fluorescein
GPC	Gel Permeation Chromatography
H	Hour
HEPES	4-(2-Hydroxyethyl)-1-Piperazineethanesulfonic Acid
IC_{50}	Half maximal inhibitory concentration
IL-11	Interleukin 11
LAP	2,2-Dimethoxy-2-Phenylacetophenone
LM2-4175	Lung-tropic MDA-MB-231Subline
M	Molar
MAPK	Mitogen Activated Kinase
MCF7	Human Breast Epithelial Cell Line
MDA-MB-231	Human Breast Adenocarcinoma Cell Line
Metabolic Ratio	Metabolic Activity at Day 15: Activity at Day 0
MMP	Matrix Metalloproteinase
MRP1	Multidrug Resistance-Associated Protein 1
NC Ratio	Nuclear to Cytoplasmic Mean Intensity Ratio
New Live: New Dead	Change in Number of Viable Cells Between Days 0-15:
Cell Ratio	Change in Number of Dead Cells Between Days 0-15
NVP	N-vinyl pyrrolidone
PAC	Paclitaxel
PBS	Phosphate Buffered Saline
PDMS	Poly(dimethylsiloxane)

PEGDA	Polyethylene Glycol Diacrylate
PEG-SVA	PEG-Succinimidyl Valerate
P-gp	P-glycoprotein
PQ	MMP-degradable Peptide Sequence: GGGPQGIWGQGK
UV	Ultraviolet